

5-1-2022

## The Effects of Winds on Accretion Disks and Spectra Of X-Ray Binaries and Active Galactic Nuclei

Shalini Ganguly

Follow this and additional works at: <https://digitalscholarship.unlv.edu/thesesdissertations>



Part of the [Astrophysics and Astronomy Commons](#)

---

### Repository Citation

Ganguly, Shalini, "The Effects of Winds on Accretion Disks and Spectra Of X-Ray Binaries and Active Galactic Nuclei" (2022). *UNLV Theses, Dissertations, Professional Papers, and Capstones*. 4400.  
<http://dx.doi.org/10.34917/31813281>

This Dissertation is protected by copyright and/or related rights. It has been brought to you by Digital Scholarship@UNLV with permission from the rights-holder(s). You are free to use this Dissertation in any way that is permitted by the copyright and related rights legislation that applies to your use. For other uses you need to obtain permission from the rights-holder(s) directly, unless additional rights are indicated by a Creative Commons license in the record and/or on the work itself.

This Dissertation has been accepted for inclusion in UNLV Theses, Dissertations, Professional Papers, and Capstones by an authorized administrator of Digital Scholarship@UNLV. For more information, please contact [digitalscholarship@unlv.edu](mailto:digitalscholarship@unlv.edu).

THE EFFECTS OF WINDS ON ACCRETION DISKS AND SPECTRA OF X-RAY  
BINARIES AND ACTIVE GALACTIC NUCLEI

By

Shalini Ganguly

Bachelor of Science in Physics  
University of Calcutta, India  
2015

Master of Science in Physics  
Indian Institute of Technology Hyderabad, India  
2017

A dissertation submitted in partial fulfillment  
of the requirements for the

Doctor of Philosophy - Astronomy

Department of Physics and Astronomy  
College of Sciences  
The Graduate College

University of Nevada, Las Vegas  
May 2022



## **Dissertation Approval**

The Graduate College  
The University of Nevada, Las Vegas

April 8, 2022

This dissertation prepared by

Shalini Ganguly

entitled

The Effects of Winds on Accretion Disks and Spectra Of X-Ray Binaries and Active  
Galactic Nuclei

is approved in partial fulfillment of the requirements for the degree of

Doctor of Philosophy - Astronomy  
Department of Physics and Astronomy

Daniel Proga, Ph.D.  
*Examination Committee Chair*

Bing Zhang, Ph.D.  
*Examination Committee Member*

George Rhee, Ph.D.  
*Examination Committee Member*

Balakrishnan Naduvalath, Ph.D.  
*Graduate College Faculty Representative*

Kathryn Hausbeck Korgan, Ph.D.  
*Vice Provost for Graduate Education &  
Dean of the Graduate College*

## Abstract

Active galactic nuclei (AGNs) and X-ray binaries (XRBs) contain at their cores supermassive black holes (SMBH), and stellar mass black holes or neutron stars, respectively. These objects bind matter gravitationally, leading to the formation of accretion disks. The accretion of matter leads to efficient conversion of gravitational potential energy into radiation. When the force and/or energy imparted by this radiation on matter exceeds the attractive force due to the local gravitational field, it leads to the launching of matter in the form of outflows or winds. These outflows produce blueshifted (and occasionally redshifted) emission or absorption components in the spectra of these sources. For instance, Seyfert galaxies generally display absorption lines with relatively small blueshifts ( $\sim 100\text{--}1000\text{ km s}^{-1}$ ) in their UV and X-ray spectra, indicating the presence of mass outflows. In some such galaxies, the X-ray absorbers (the so-called warm absorbers, WAs) and UV absorbers have very similar velocities which suggests that these absorbers are nearly cospatial. This, in turn, suggests that regions of very different temperatures coexist and that the absorption occurs in a multi-phase outflow.

In this dissertation, we study two distinct effects of disk winds/outflows: (a) self-regulating effects on accretion disks, and (b) effects on the background continuum radiation due to absorption. The self-regulating disk-wind feedback process is an example of how disk winds can regulate the time evolution of the entire accretion disk. We develop a one-dimensional radial hydrodynamic code to study the evolution of such a disk. By relaxing the condition of a fixed wind launching radius, we find that an accretion disk is destabilized for much stronger winds than previously predicted for a fixed launching radius model. We then compute thermally-driven outflow models irradiated by an AGN continuum, using the magnetohydrodynamics code *ATHENA++*. An isobaric perturbation can trigger thermal instability leading to the formation of multi-phase outflows that can have distinguishing effects on the absorption line profiles. To study such effects, we develop and test a pipeline written in Python, which combines results from *ATHENA++* and the photoionization calculation code *XSTAR*. We use this pipeline to generate the absorption line profiles based on our outflow solutions. We discuss how absorption line profiles produced by different species could help distinguish smooth outflows from multi-phase ones.

## Acknowledgements

At the end of this five year long journey, I am grateful for this opportunity to be able to thank everyone who helped me achieve my goal. I would like to thank, first and foremost, my advisor, Dr. Daniel Proga. My dream of pursuing research in astrophysics came to fruition under his guidance. I gained immensely from his wealth of knowledge and experience. I am thankful to Daniel for his patience and for always being available to address any concerns via email or Slack (on that note, we are also very grateful for the messaging platform Slack, for making it so much easier to share files/ideas/concerns with colleagues). I am also extremely thankful to all my research associates working in Daniel's group, particularly Tim Waters, Randall Dannen and Sergei Dyda. They set a high standard for what it means to be a researcher. I thank them for bearing with me through the many questions involving code debugging and paper editing. Tim and Sergei were also great mentors and I learned a lot from our interactions. I am also indebted to them for their help with my postdoctoral job applications.

I am grateful for the useful suggestions and thoughtful inquiries received from my research committee members, Dr. Bing Zhang, Dr. George Rhee and Dr. Balakrishnan Naduvalath. I had the opportunity to take an independent course with Dr. George Rhee, whereby I had the opportunity to revisit Bayesian statistics and be introduced to the concept of Reverberation Mapping in Active Galactic Nuclei. I enjoyed taking the High Energy Astrophysics course with Dr. Bing Zhang and learned a lot in the process. Lastly, I thank Dr. Balakrishnan Naduvalath for the tough questions related to photoionization code setups that helped put my research into perspective. I would also like to thank Dr. Shantanu Desai, for all his help and guidance during my masters. I wouldn't be here if not for him.

I am also thankful for all the amazing people I met at the Department of Physics and Astronomy at UNLV. I enjoyed Dr. Rebecca Martin's classes and talking to her about my first project involving accretion disk simulations. I thoroughly enjoyed Dr. Zhaohuan Zhu's course on Computational Physics. I am thankful for the weekly Journal Clubs and Astro Coffees with my peers, where we often had very interesting discussions. I would like to thank the newer members of Daniel's group, Margaret and Colin, for our small chats during the pandemic era and I wish them the very best in their paths. I would also like to thank the staffs of our department who were always hard at work. I especially thank Natasa for all her help and for being so friendly and kind.

This city of Las Vegas, located almost diametrically opposite on the globe to my home town, Howrah, in India, was a vibrant experience of my youth. It gave me two amazing friends, Ankita and Anjan, who made this rather exciting yet arduous experience, so much richer. I would also like to

thank the internet and free international calls for keeping my past friendships alive during this discourse, despite the prevalent turmoil in the world. Lastly, and most importantly, I would like to thank my parents and my little brother for believing in me and encouraging my relentless selfish pursuits. I cannot thank my aunt (mum) enough for always being there for me. I would like to dedicate my work to both my grandfathers and thank them for their wisdom, and my grandmothers for their undying love. Finally, I cannot thank Anish enough for being there in my life, and for loving and supporting me through thick and thin.

# Table of Contents

<b>Abstract</b>	<b>iii</b>
<b>Acknowledgements</b>	<b>iv</b>
<b>List of Tables</b>	<b>ix</b>
<b>List of Figures</b>	<b>xv</b>
<b>List of Symbols</b>	<b>xvi</b>
<b>1 Introduction</b>	<b>1</b>
1.1 Accretion Disks . . . . .	5
1.1.1 Shakura-Sunyaev Disks . . . . .	7
1.1.2 Radiation Spectrum of Accretion Disks . . . . .	9
1.1.3 Disk Winds . . . . .	11
1.2 X-ray Binaries . . . . .	12
1.2.1 State Transitions . . . . .	13
1.3 Active Galactic Nuclei . . . . .	14
1.3.1 AGN Outflows . . . . .	16
1.3.2 Spectral Energy Distribution of AGN . . . . .	18
1.4 Thesis Outline . . . . .	20
<b>2 Wind-driven Relaxation Cycles in Accretion Disks</b>	<b>21</b>
2.1 The Problem . . . . .	21
2.1.1 Equations for Disk Evolution . . . . .	22
2.1.2 $\delta$ -function Wind at $R_d$ . . . . .	25
2.2 Models . . . . .	27
2.2.1 Fixed Launching Radius at $R = R_d$ . . . . .	27
2.2.2 Variable Launching Radius $R_L$ . . . . .	28
2.3 Numerical Methods . . . . .	28
2.4 Results and Discussions . . . . .	29
2.4.1 Fixed Launching Radius . . . . .	29

2.4.2	Variable Launching Radius . . . . .	31
2.5	Conclusion . . . . .	33
<b>3</b>	<b>Synthetic Absorption Line Profiles of Thermally-</b>	
	<b>Driven Winds in AGNs</b>	<b>38</b>
3.1	Thermally-Driven Winds . . . . .	38
3.2	Field's Criterion for Thermal Instability . . . . .	39
3.3	Photoionization Code - XSTAR . . . . .	40
3.3.1	Photoionized Plasma Modelling . . . . .	41
3.3.2	Photoionization Calculation Setup . . . . .	42
3.4	Models . . . . .	43
3.4.1	Clumpy Models . . . . .	46
3.5	Ionization Structure and Absorption Diagnostics . . . . .	48
3.5.1	Photoionization Calculations . . . . .	51
3.6	Results . . . . .	52
3.6.1	Steady State Wind Solutions . . . . .	54
3.6.2	Clumpy Wind Solutions . . . . .	59
3.7	Conclusion . . . . .	65
<b>4</b>	<b>Conclusion</b>	<b>69</b>
	<b>References</b>	<b>76</b>
	<b>Curriculum Vitae</b>	<b>77</b>



## List of Tables

2.1	Summary of all parameters ( $C'$ and $p$ ) used in simulations for the model described by eqn (2.31). The subscripts d, crit and g denote values of $C'$ for which the oscillations decay, persist and grow, respectively. The value of $C'_{crit}$ increases with increasing $p$ . In Fig. 2.3, we use the corresponding $C'_{crit}$ to plot the wind efficiency $\eta_{w,crit}$ , which decreases with increasing $p$ . . . . .	31
2.2	Summary of parameter survey. $C'_d, C'_{crit}, C'_g$ hold the same meaning as described in the Table 2.1. The two new types of outcome, $C'_{sd}$ and $C'_{sg}$ , denote oscillations that decay/grow for a few time scales before stabilizing and oscillating with a constant amplitude. In Fig. 2.5, we use the corresponding $C'_{crit}$ to plot the wind efficiency $\eta_{w,crit}$ . . . . .	37
3.1	Model parameters and some gross properties of steady wind models A21, B and C. These models share the following basic parameters: $\Gamma = 0.3$ , $\Xi_0 = 3.12$ ( $\xi_0 = 5.0$ erg cm s $^{-1}$ ) and $M_{BH} = 10^6 M_\odot$ . D20 found that models B and C are unsteady. However, Waters et al. (2021) refined the numerical methods and found that these two models can eventually settle down to an unstable yet steady state. Once these solutions are perturbed they become clumpy in agreement with D20's findings. The second, third, and fourth columns list the hydrodynamic escape parameter $HEP_0$ , the inner radius $r_0$ , and the density $\rho_0$ at $r_0$ , respectively. The next three columns list the following properties of the solutions: the flow velocity $v$ and mass loss rate $\dot{M}$ at the outer most grid point, $r_{out}$ , at a late time when the flow has become steady. The last column shows the hydrogen column density $N_H$ for the outflow. . . . .	44
3.2	Ionic column densities (cm $^{-2}$ ) in steady models. The ionic column density for each ion in our survey, $N_{ion} = \int n_1 dr$ , where $n_1$ is the level population for the ground state, for the three steady models A21, B and C. . . . .	52

3.3 Ions used for computing line profiles (in decreasing order of IE). We denote different transitions for the same ion with a number, which corresponds to the wavelength of the transition, as in Si XIV 5 and Si XIV 6. The 2<sup>nd</sup>, 3<sup>rd</sup>, and 4<sup>th</sup> column denote the rest frame wavelength  $\lambda_0$ , the velocity shift (in  $\text{km s}^{-1}$ ) of the doublet components  $\Delta v = c(\lambda_b - \lambda_r)/\lambda_r$  (where subscripts  $r$  and  $b$  denote red and blue components) and the ionization energy of the ion, IE. . . . . 66

## List of Figures

- 1.1 An image of P Cygni, a variable star in the constellation Cygnus located around 1500 - 1800 parsecs from Earth, and first discovered by Dutch astronomer, Willem Janszoon Blaeu, on August 18, 1600. The image is taken from Second Digital Sky Survey by combining blue, red and near infrared plates in false colour. Image courtesy: SkyView and CalTech/STScI, colour image processing done by W. Renz. . . . . 2
- 1.2 *Left:* Geometry of stellar wind with outward velocity gradient; the star at the center (shown in white) occults the gas column at the ‘back’ (B), while the gas column in the ‘front’ (F) contributes to absorption, and the gas columns on the ‘sides’ (S) scatter radiation from photosphere in all directions. *Right:* The net absorption and emission components result into the so-called P Cygni profile. Image courtesy: Lamers & Cassinelli (1999) . . . . . 3
- 1.3 Hubble Heritage (STScI) image of a portion of the Carina Nebula; Eta Carinae and the Homunculus Nebula is the bright spot near the left edge of the field. The most massive stars, like P Cygni, O and B type stars (as shown in this image), last only a few million years from their formation to their catastrophic destruction as Type II supernovae, which contribute to a three-phase model of the ISM as studied by McKee & Ostriker (1977). . . 5
- 1.4 Viscous angular momentum transport and differential viscous torque in a shearing medium. The chaotic exchange of matter between adjacent layers cannot result in net mass transfer but the particles in adjacent layers carry different angular momenta (shown by blue curved arrows) which results in viscous torque being exerted on outer layer by inner layer. The inner layer thus, loses angular momentum to the outer layer and slowly spirals inward. The ring of gas between  $R$  and  $R + dR$  is subject to competing torques (shown by black curved arrows). The net torque leads to dissipation of energy within the gas. . . . . 9

1.5	<i>Left:</i> A schematic of an accretion disk, where the coloured rings indicate the different zones contributing to the corresponding coloured spectra shown on the right. <i>Right:</i> Integrated emitted spectra of accretion disk radiating a local blackbody spectrum at each radius, with arbitrary units. The temperature at the outermost radius $R_{\text{out}}$ is denoted by $T_{\text{out}}$ and $R_*$ corresponds to the innermost disk radius. The ‘flat’ part $S_\nu \propto \nu^{1/3}$ makes this a characteristic accretion disk spectrum (black curve), giving the impression of a stretched-out blackbody, as is evident from looking at the contribution of the red (innermost), green (intermediate) and blue (outermost) zones of the accretion disk. . . . .	10
1.6	<i>Left:</i> X-ray spectral states of Cyg X-1 from Gierliński et al. (1999). <i>Right:</i> Hardness-intensity diagram of the 2002/2003 outburst GX 339-4 showing the ‘q-shaped pattern/hysteresis’ (Belloni, 2005) . . . . .	14
1.7	The unified model of Active Galactic Nuclei (AGNs). <i>Image credit:</i> Beckmann & Shrader (2012) . . . . .	15
1.8	The average physical parameters of ionized outflows in AGNs. This image shows the relative spatial extent of the outflows and, in a way, depicts a ‘unified model of AGN outflows’ detected so far. <i>Image credit:</i> Laha et al. (2021). . . . .	18
1.9	Obscured (AGN1) and unobscured (AGN2) AGN SEDS of NGC 5548 studied in Danneken et al. (2019) (top panel). The UV (blue) and X-ray (red) energy bands are shaded and the bottom panel shows the fraction of the total energy of SED in each energy component band for AGN1 and AGN2. . . . .	19
2.1	A schematic of mass accretion rates at different parts of the accretion disk around a compact object (the accretor, shown as a black circle on the left). Near the outermost disk radius, the disk flares and the net wind mass loss rate and (constant) mass supply rate result in the mass accretion rate $\dot{M}(R_d)$ at steady state. Defining the wind mass loss rate at some radius $R$ as a sink term integrated from the inner radius upto that radius, the mass accretion rate $\dot{M}(R)$ is the resultant of the mass accretion rate at the inner radius of the disk $\dot{M}_a$ and the net loss in the form of wind $\dot{M}_w(< R)$ . . . . .	23

2.2	Central mass accretion rate (normalized to the steady state mass accretion rate) evolution of the disk for different wind strength parameter $C$ . The top panel shows decayed oscillations in the disk, the middle panel shows the critical $C$ case where the oscillation persists with constant amplitude. The bottom panel shows a growing oscillation phase, which saturates after some time due to local disk depletion. . . . .	30
2.3	The critical wind efficiency $\eta_{w,crit}$ as a function of the power-law index, $p$ , in accordance with eq. (2.31). . . . .	31
2.4	Examples of the time evolution of the accretion rate for (a) $\Gamma = 0.2, p = 0.5$ ( <i>left</i> ), and (b) $\Gamma = 0.7, p = 1$ ( <i>right</i> ), for various $C'$ . <i>Left</i> : The top panel shows an example of an initial decay that is followed by a constant amplitude oscillation. The second, third and fourth panels depict the range of $C'_{crit}$ that lead to stable oscillations. <i>Right</i> : The top three panels indicate a damped high amplitude oscillation superposed on the fundamental mode oscillating around the steady state value of 1. The lowest panel shows growing oscillations that saturate but has a very high frequency of oscillation, which increases with time. . . . .	32
2.5	<i>Left</i> : The steady state critical wind efficiency $\eta_w$ vs $p$ for different $\Gamma$ values. For some $\Gamma$ , stable oscillations occur not just for a single value of $\eta_w$ , but for a range of $\eta_w$ (see Fig. 2.4 for some examples, e.g. second, third and fourth panels there). We shaded the regions for $\Gamma$ s where this happens. <i>Right</i> : The steady state critical wind efficiency $\eta_{w,crit}$ vs $\Gamma$ for different $p$ values (top panel). In the bottom panel, we plot $p\eta_{w,crit}$ vs $\Gamma$ for different $p$ values. Once again, the shaded region highlights the possible $\eta_{w,crit}$ values for a particular combination of $p$ and $\Gamma$ . . . . .	34
3.1	Thermal equilibrium curve (solid curve) relevant to the two-phase model of the ISM. The dashed line shows a fiducial isobar $P \propto \rho T = \text{constant}$ , which shows three possible phases in pressure equilibrium with one another. The phases F and H are thermally stable, while phase G is thermally unstable. <i>Image credits</i> : Shu (1992). . . . .	40

- 3.2 Phase diagram ( $T - \Xi$ ): the solid black line represents the thermal equilibrium curve (S-curve) while the black dashed line represents the Balbus contour. All points to the left of the latter are thermally unstable whereas those to the right are thermally stable according to Balbus' criterion for TI (Balbus, 1986). There are two unstable regions encountered while tracing the S-curve starting from low temperatures; we refer to them as the lower and upper TI zones. The figure also shows our three steady wind solutions (solid red, dot-dashed green, and dashed blue line for model A21, B, and C, respectively). We marked the sonic points for each solution with an '×'. Notice that upon reaching  $\Xi_{c,max}$  (marked by red dot on the S-curve), Model A21 exhibits runaway heating and quickly exits the lower TI zone. Models B and C instead follow the S-curve within this zone. The decrease in temperature beyond the sonic points in all three cases is due to efficient adiabatic cooling being balanced by radiative heating. . . . . 45
- 3.3 *Left*: Radial profiles of logarithm of number density  $n$  ( $\text{cm}^{-3}$ ), temperature  $T$  (K), flow velocity  $v$  ( $\text{km s}^{-1}$ ), ionization parameter  $\xi$  ( $\text{erg cm s}^{-1}$ ) and the dimensionless pressure ionization parameter  $\Xi$ , for the three steady wind models shown in Fig. 3.2. Sonic points are again marked by '×'s. The horizontal line in the fourth panel marks  $\log(\xi_{c,max}) = 2.15$ , the entry into the lower TI zone. *Right*: Fractional ionic abundance  $\eta$  (shown on left y-axis, with thinner lines) and the ion ground state level population  $n_1 = n\eta A$  (shown on right y-axis, with thicker lines) vs  $\log(r - r_0)$ , for the same five ions whose line profiles are compared in Fig. 3.6. The topmost panel shows radial velocity profiles (in  $\text{km s}^{-1}$ ) to aid in assessing blueshifts. The legend in this panel applies to both the left and right y-axes. *Bottom*: The same quantities as in the top right subfigure, but plotted against the flow velocity  $v$  (in  $\text{km s}^{-1}$ ) rather than distance. The topmost panel shows the radial distribution of  $v$ . . . . . 47
- 3.4 Comparison of the AMD for our three steady state wind solutions. The top panel shows the AMD (eq. 3.17) in units of its maximum value for model A21 ( $= 8.8 \times 10^{22} \text{cm}^{-2}$ ) versus  $\xi$ . The vertical black dotted line marks the base of the lower TI zone,  $\xi = \xi_{c,max}$ , while the three triangles mark the points where each model leaves this TI zone. In the bottom panel, these AMDs are mapped onto the flow velocity,  $v$  (in  $\text{km s}^{-1}$ ; the range with  $v < 1 \text{ km s}^{-1}$  is not shown). Sonic points are marked with '×' symbols and the color shadings denote the parameter space of gas occupying the lower TI zone. . . . . 49

- 3.5 Column densities as functions of ionization energy. *Top panel:* the column density of a given ion (the ionic column density,  $N_{\text{ion}}$ ) as a function of IE of that ion (see also Table 3.2). *Bottom panel:* as above but with  $N_{\text{ion}}$  corrected for the element abundance ( $N_{\text{ion}}/A$ ), so it is the hydrogen column density in the region where a given ion is present. 53
- 3.6 Absorption profiles due to lines from five ions (as labeled) together with a plot of  $\xi$  vs.  $v$  (bottom panel). Red solid, green dot-dashed, and blue dashed lines denote model A21, B and C, respectively. Absorption troughs are shaded to highlight their depth and shape. Except for Fe XXV, all lines shown here are doublets (see Table 3.3 for details). The C IV doublet components (second from the bottom panel) are separated in all three models whereas the Si XIV 5, Mg XII, and O VIII 19 doublet components are blended. The vertical grey dashed line marks  $v = 0$  in all panels. In the lowermost panel, the horizontal dashed line marks  $\log(\xi_{c,\text{max}}) = 2.15$  in order to judge the blueshift at which the flow enters the lower TI zone. . . . . 55
- 3.7 Absorption profiles for models A21, B and C (left, middle, and right columns of panels, respectively). See the ion labels at left and Table 3.3 for the line identification. The profiles are shown using solid black lines. For doublet lines, we plot a composite spectrum by adding the red and blue components while accounting for their wavelength separation in velocity space. The individual components have been additionally plotted with red and blue dashed lines. In the bottom panel, we plot the ionization parameter against the radial flow velocity, for reference. The dashed horizontal line indicates the value of  $\xi_{c,\text{max}}$ , whereas the black vertical line marks zero velocity. For FITS files of all our line profile calculations, see: <http://www.physics.unlv.edu/astro/clumpywindsims-lps.html>. . . . . 57
- 3.8 The position of the the blue-edge of the absorption trough,  $v_B$  as a function of IE. We formally define  $v_B$  as the velocity where  $I_v = 0.99$ . When the line is a blended doublet we correct  $v_B$  for the doublet split. Here we show results for the steady models. The blue and red dashed lines indicate the maximum flow velocity and the velocity where ionization parameter  $\log \xi = \log \xi_{c,\text{max}} = 2.15$ , respectively. . . . . 58

- 3.9 *Left:* Line profile comparison for the steady model B (dot-dashed green shaded profile) and the unsteady/clumpy model B-c (dotted magenta shaded profile, refer to eq. 3.15). The lower panel shows  $\log \xi$  vs  $v$  for these two cases, for comparison, where horizontal gray dashed line marks  $\log(\xi_{c,\max}) = 2.15$ , while vertical dashed lines mark  $v = 0$  in all panels. *Right:* Contributions of different parts of a clumpy outflow (model B-c) to the overall line profile for Mg XII. The colors green, blue and cyan highlight the higher-than-average density regions corresponding to clumps, while the red, magenta and yellow highlight intercloud regions. . . . . 60
- 3.10 Variability of the Mg XII line profile for model B-c. Line profiles at three different states  $t_i$  of the simulation runs are plotted along with the time-averaged line profile. The legend shows the time  $\Delta t = (t_i - t_0)$  (in kyr), the red line denoting the state  $t_0$ . The middle panel shows the difference between the snapshots from the average profile. The bottom panel shows the cooling time,  $t_{\text{cool}}$ ; a vertical line marks the velocity for which  $\log \xi_{c,\max} = 2.15$ , showing that cooling times exceed 1 year in the clumps. Any time-dependence must therefore occur on longer timescales. An animation of the time evolution of line profiles for B-c and C-c, can be found here: <http://www.physics.unlv.edu/astro/clumpywindsims-lps.html>. . . . . 61
- 3.11 Ionization energy vs velocity of the blue-edge of line profiles (defined as where  $I = 0.99$ ) for steady models (black solid line with red dots) compared to their clumpy versions (black dashed line with green dots). The dotted (dashed) blue and red vertical lines indicate the maximum flow velocity and the velocity where  $\xi = \xi_{c,\max}$ , respectively, for the clumpy (steady) models. . . . . 62
- 3.12 Same as 3.7, but for steady model B compared to clumpy model B-c. . . . . 63
- 3.13 Same as 3.12, but for steady model C compared to clumpy model C-c. . . . . 64



## List of Symbols

$k$	Boltzmann's constant	$1.3807 \times 10^{-16} \text{ cm}^2 \text{ g s}^{-2} \text{ K}^{-1}$
$e$	Charge of electron	$4.8032 \times 10^{-10} \text{ cm}^{3/2} \text{ g}^{1/2} \text{ s}^{-1} \text{ (esu)}$
$L_{\odot}$	Luminosity of sun	$3.839 \times 10^{33} \text{ erg s}^{-1}$
$m_e$	Mass of electron	$9.1094 \times 10^{-28} \text{ g}$
$m_p$	Mass of proton	$1.6726 \times 10^{-24} \text{ g}$
$M_{\odot}$	Mass of sun	$1.989 \times 10^{33} \text{ g}$
$pc$	Parsec	$3.086 \times 10^{18} \text{ cm}$
$c$	Speed of light in vacuum	$2.99792458 \times 10^{10} \text{ cm s}^{-1}$
$\sigma$	Stefan-Boltzmann constant	$5.6704 \times 10^{-5} \text{ g s}^{-3} \text{ K}^{-4}$
$h$	Planck's constant	$6.6261 \times 10^{-27} \text{ cm}^2 \text{ g s}^{-1}$

# Chapter 1

## Introduction

The observable Universe is interspersed with baryonic matter, mostly in the form of hot gases and ionized plasmas. The physics of ionized plasma tells us about the formation and evolution of astrophysical objects such as Active Galactic Nuclei (AGNs), X-ray binaries (XRBs), and Young Stellar Objects (YSOs). By studying the emission and absorption spectral signatures of ionized plasma around such objects, we can determine how they interact with their surroundings. For example, gaseous nebulae emit spectra dominated by forbidden lines of ions of common elements such as Oxygen, Nitrogen and Sulphur, in addition to permitted lines of Hydrogen and Helium, comprising the full range of the electromagnetic spectrum. Planetary nebulae provides us with a view of the outer envelopes of dying stars and differ from the spectral signatures of other nebulae in that the spectral shape is more compact and round rather than chaotic and patchy. Extremely luminous objects ( $L \sim 10^{42} - 10^{48} \text{ erg s}^{-1}$ ) such as Quasars, Active Galactic Nuclei, and Quasi Stellar Objects (QSOs) are theorized to be powered by accretion due to the supermassive black hole at their centers (see Antonucci (1993) for a review). The study of ionized hot gases in many such systems comprises of the branch of astrophysics called Astrophysical Fluid Dynamics (AFD). It has applications in various fields such as the study of stellar and planetary interiors, winds and jets in accretion disks, the interstellar as well as intergalactic medium and certain areas of cosmology (Ogilvie, 2016).

The continuous outflow of materials from stars was dubbed “solar winds” or “stellar winds” by Eugene N. Parker in 1958 and 1960, who then went onto present one of the first theoretical solutions for the simple case of an isothermal, steady-state spherical wind, in which the gas is subject to only the inward force of gravity and the outward gradient of gas pressure. For a stationary spherically symmetric wind, the mass loss rate is given by the equation of mass continuity,  $\dot{M} = 4\pi r^2 \rho(r) v(r)$ , where  $r$  is the distance from the center of the star,  $\rho$  is the density and  $v$  is the velocity. The distribution of velocity of the wind with radial distance from the star, called the velocity law,  $v(r)$ , can often be approximated by a  $\beta$ -law, given by

$$v(r) \simeq v_0 + (v_\infty - v_0) \left(1 - \frac{R_*}{r}\right)^\beta \quad (1.1)$$

where  $v_0$  is the velocity at the photosphere ( $r = R_*$ ) and  $v_\infty$  is the velocity at large distances, such that  $v_0 \ll v_\infty$ . Observations and models of stellar winds indicate that the above approximation mostly holds.



Figure 1.1: An image of P Cygni, a variable star in the constellation Cygnus located around 1500 - 1800 parsecs from Earth, and first discovered by Dutch astronomer, Willem Janszoon Blaeu, on August 18, 1600. The image is taken from Second Digital Sky Survey by combining blue, red and near infrared plates in false colour. Image courtesy: SkyView and CalTech/STScI, colour image processing done by W. Renz.

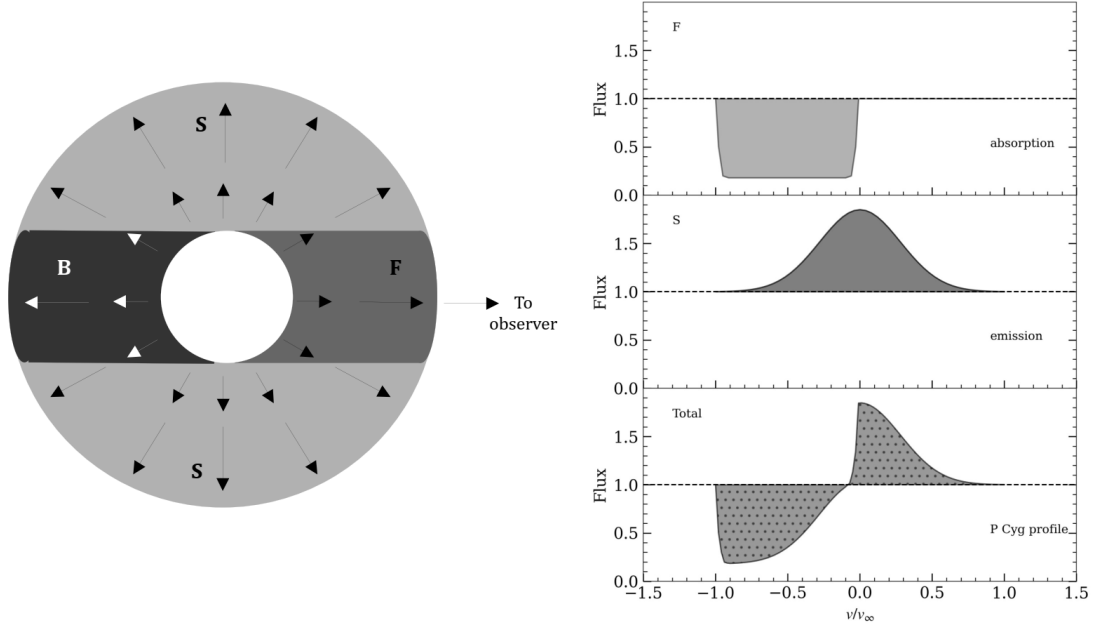


Figure 1.2: *Left:* Geometry of stellar wind with outward velocity gradient; the star at the center (shown in white) occults the gas column at the ‘back’ (B), while the gas column in the ‘front’ (F) contributes to absorption, and the gas columns on the ‘sides’ (S) scatter radiation from photosphere in all directions. *Right:* The net absorption and emission components result into the so-called P Cygni profile. Image courtesy: Lamers & Cassinelli (1999)

The so-called ‘P Cygni’ type stars, first observed by the Dutch astronomer, Willem Janszoon Blaeu, in 1600, show emission components redshifted with respect to line center, along with blueshifted absorption components (see figs. 1.1 and 1.2). It was later identified to be caused by persistent, strong stellar winds. The spectral lines due to atomic transitions from the ground state of abundant ions, called resonance lines, are the most common and sensitive indicators of mass loss rate from hot stars. Some well known resonance lines include C IV, N V and Si IV (in UV spectra) in O- and early B-type stars, C II (in UV spectra) in late B- to A-type stars and Mg II (in UV spectra) of late B- to M-type stars. These abundant ions, due to the high oscillator strength of their resonance transition, can produce observable absorption lines that show Doppler shift due to the outflow, despite a small  $\dot{M}$  value. For small column density values of absorbing ions, about  $10^{13}$ - $10^{14}$  ions  $\text{cm}^{-2}$ , resonance lines produce weak but observable absorption. For column densities larger than  $10^{15}$  ions  $\text{cm}^{-2}$ , the lines produce the ‘P Cygni’ profiles.

The observation from interplanetary space probes have showed evidence for strong time dependence of solar wind properties. This brought forth the development of further theories of stellar winds such as the Alfvén wave driven wind theory (Parker, 1965; Belcher, 1971), magnetic rotator theory (Weber & Davis, 1967) and the radiation-driven wind theory (Lucy & Solomon, 1970; Castor et al., 1975). The

line-driven wind model that includes radiation force from spectral lines, such as the CAK winds (Castor et al., 1975), has particularly proven to be quite successful in explaining the observed mass loss rates and terminal velocities. Calculation of line force showed that it exceeds gravity for a wide range of conditions for early type stars (Lucy & Solomon, 1970; Lamers & Morton, 1976) and suggests that radiation pressure dominates these winds (Abbott, 1980).

The region between stars is filled with extremely dilute gas, called the interstellar medium, with densities of only a few atoms per cubic centimeters, and a very attenuated interstellar radiation field with radiation density of a few photons per cubic centimeters. It primarily comprises of hydrogen gas, significant amounts of helium atoms, along with trace percentages of calcium, sodium, water, ammonia, and formaldehyde. In isolated cases, we can assume thermodynamic equilibrium for the interstellar medium (ISM). In 1939, Strömgren first concluded that the interstellar space is sharply defined by regions of ionized (H II) and nonionized (H I) hydrogen. Interstellar hydrogen is ionized by far-ultraviolet radiation (Lyman continuum ( $L_c$ ),  $\lambda > 912 \text{ \AA}$ ) emerging from hot stars with high luminosities (Kaplan, 1970).

The dynamics of ISM comprises of the study of gas motion in the interstellar space including the formation, properties and attenuation of ionizing and shock waves, interstellar turbulence, condensation of interstellar gas clouds and more. For a predominantly neutral gas heated by low-energy cosmic rays, it has been well established that a thermally bistable phase model, which consists of gases of two densities and temperatures coexisting in pressure equilibrium, best describes the ISM - the so-called *two phase model* (Goldsmith et al., 1969). A harder-to-model *three phase model* has also been put forth since (Cox & Smith, 1974; McKee & Ostriker, 1977) involving a hotter third phase heated by supernovae explosions, leading to the current multiphase theory of the ISM. Figure 1.3 shows a Hubble image of a part of the Carinae Nebula comprising of massive P Cygni, O and B stars that will catastrophically reach their end in Type II supernovae, thus, setting the stage for studying the complex dynamics of the multiphase ISM.

The study of observational signatures in stellar winds forms the basis of understanding absorption and emission components in outflows/winds of various astrophysical systems. Understanding the interaction of matter and radiation helps determine the physical state of ionized gases around these systems. The two-phase model of the ISM has been a primary source of understanding more complex multiphase gases in, for instance, Seyfert galaxies, where observations indicate very different temperature regions coexisting and absorption taking place in multiphase outflows. The aim of this dissertation is to study winds/outflows in accretion disks of X-ray binaries or Active Galactic Nuclei. In the following sections, we introduce accretion disks, which are active sites of wind launching and are in turn regulated by





Figure 1.3: Hubble Heritage (STScI) image of a portion of the Carina Nebula; Eta Carinae and the Homunculus Nebula is the bright spot near the left edge of the field. The most massive stars, like P Cygni, O and B type stars (as shown in this image), last only a few million years from their formation to their catastrophic destruction as Type II supernovae, which contribute to a three-phase model of the ISM as studied by McKee & Ostriker (1977).

them. We also discuss briefly the systems involved in our study, specifically XRBs and AGNs, and their primary observational aspects, in an effort to understand the effect of winds/outflows on the observed spectrum.

## 1.1 Accretion Disks

The accumulation of matter around a central object by virtue of its gravitational attraction can lead to the formation of an accretion disk. The central objects associated with such disks comprise of super-massive black holes at the center of AGNs, neutron stars or black holes in X-ray binaries, young stellar objects (YSOs) embedded in nebular material, etc. In a binary system, the matter flowing out from the secondary companion star has considerable angular momentum which prevents it from freely falling

onto the primary star (accretor). At certain distances from the black hole, the centrifugal forces would balance the gravitational force of the central object, whereby matter would begin to rotate in circular orbits. Only through efficient outward transfer of angular momentum can this matter of rotating gas reach the inner gravitational radius of the accretor. The matter ejected by the companion is generally imbued with magnetic field, which coupled with its turbulent motions, enable outward transportation of angular momentum. The matter in the disk loses gravitational potential energy while gaining kinetic energy and thermal energy, which is eventually radiated away (Zel'dovich, 1964; Salpeter, 1964; Shu, 1992). Thus, accretion of matter on to compact objects is a natural and powerful mechanism for producing high energy radiation.

To produce a simple order-of-magnitude estimate, let us consider a body of mass  $M$  and radius  $R$ . The gravitational potential energy released by the accretion of a mass, say  $m$ , on to its surface is  $\Delta E_{\text{acc}} = GMm/R$ , where  $G$  is the gravitational constant. For a neutron star with radius  $R \sim 10$  km, mass  $M \sim M_{\odot}$ , the solar mass, the value of  $\Delta E_{\text{acc}}$  is about  $10^{20}$  erg  $\text{g}^{-1}$ . In comparison, if we consider energy release by nuclear fusion reactions in a mass  $m$ , comprised initially of hydrogen (as is usually the case in astrophysics), we get  $\Delta E_{\text{nuc}} = 0.007mc^2$ , where  $c$  is the speed of light in vacuum, leading to the value of  $\Delta E_{\text{nuc}}$  to be about  $6 \times 10^{18}$  erg  $\text{g}^{-1} \sim (1/20)\Delta E_{\text{acc}}$ .

We can characterize the emitted radiation by its temperature  $T_{\text{rad}}$  such that the energy of a typical photon,  $h\bar{\nu}$ , is of the order of  $kT_{\text{rad}}$ , which gives  $T_{\text{rad}} = h\bar{\nu}/k$ . For a source of radius  $R_*$  with typical accretion luminosity  $L_{\text{acc}}$ , the corresponding blackbody temperature can be defined as  $T_{\text{bb}} = (L_{\text{acc}}/4\pi R_*^2 \sigma)^{1/4}$ . If the gravitational potential energy of accreted material were converted entirely into thermal energy, then for each proton-electron pair accreted, the potential energy released is  $GM(m_p + m_e)/R_* \approx GMm_p/R_*$ , and the thermal energy is  $2 \times \frac{3}{2}kT_{\text{th}}$ , giving  $T_{\text{th}} = GMm_p/3kR_*$ . For an optically thick flow, the radiation reaches thermal equilibrium with the accreted material before escaping out to the observer and we have  $T_{\text{rad}} \sim T_{\text{bb}}$ . If the flow is optically thin and the accretion energy is converted directly into radiation which escapes without interaction with the accreting material (as in case of shock waves produced in some accretion flows), we have  $T_{\text{rad}} \sim T_{\text{th}}$ . In general, we can thus expect the radiation temperature to lie between

$$T_{\text{bb}} \lesssim T_{\text{rad}} \lesssim T_{\text{th}} \quad (1.2)$$

This analysis gets further complicated while considering scenarios such as non-Maxwellian distribution of electrons in fixed magnetic fields. Using the above analysis, for a solar mass neutron star, we expect the mean photon energy to lie in the range  $1 \text{ keV} \lesssim h\bar{\nu} \lesssim 50 \text{ MeV}$ . Most luminous accreting neutron

star and black hole binary systems are thus, expected to emit in the X-ray to  $\gamma$ -ray part of the spectrum. Similarly, accreting white dwarfs are expected to be observed in the optical, ultraviolet and some parts of the X-ray spectra.

The success of accretion disk theories was apparent with several models being able to explain observed energetic phenomena in X-ray binaries like Sco X-1, where X-ray emissions were first explained to be due to accretion of matter by a neutron star from its companion star (Shklovskii, 1968). The *standard accretion disk* or the  $\alpha$  *disk* model came to be soon developed by Shakura & Sunyaev (1973), which was generalized to its relativistic version by Novikov & Thorne (1973). During the 1980s, several geometric considerations and heating mechanisms led to the optically thick torus in *Polish doughnut* disks (Paczynski & Wiita, 1980) and advection-dominated super-Eddington accretion rates in *slim* disks (Abramowicz et al., 1988), while the Advection-Dominated-Accretion-Flows (ADAFs) were developed in the 1990s (Narayan & Yi, 1994; Abramowicz & Lasota, 1995). The major uncertainties can still be attributed to the dissipation processes like viscosity. This has largely required us relying on observation and subsequent modelling to better understand accretion flows in AGNs and XRBs, among other astrophysical sources (Montesinos, 2012).

Recent calculations based on combining analytical and numerical techniques have succeeded to some extent in incorporating some of the missing elements. Balbus et al. (1996) have shown from general arguments that pure local hydrodynamic turbulence cannot be a self-sustaining mechanism for the generation of viscosity in Keplerian accretion disks. The idea of magnetohydrodynamic (MHD) turbulence studied by Balbus & Hawley (1991) in the context of accretion disks showed that a weak vertical field is unstable if the angular velocity of the fluid decreases outward. This type of models have yielded  $\alpha \sim 0.01 - 0.1$ , although there are several other MHD turbulence mechanisms that work as well. For the purpose of our work, which follows along the line of work done by Shields et al. (1986), we consider the  $\alpha$ -prescription as they did.

### 1.1.1 Shakura-Sunyaev Disks

The disk flow, in most cases, is confined within very close distances to the equatorial plane of the central object. Hence, to a first order approximation, we can regard the disk as a two-dimensional gas flow. The *thin disk approximation* can be used as a basis for developing theories for more complex scenarios and has already proven quite successful while comparing with observations of close binary systems. To a first approximation, we can consider Keplerian rotation giving the azimuthal velocity of gas in circular orbits as  $v_\phi = \sqrt{GM/R}$ , which implies differential rotation of matter in the disk. This holds for any



other rotation laws since any neighbouring gas elements sliding past each other will give rise to chaotic motions leading to viscous forces. Due to these chaotic motions, gas elements with different specific angular momenta are continuously exchanged between adjacent layers. This results in a viscous torque acting on the outer layer due to the inner layer. Using the surface density  $\Sigma = \rho H$  (where  $H$  is the scale height of the disk), we can write the expression for the torque exerted by the outer ring on the inner as

$$G(R) = 2\pi R \nu \Sigma R^2 \Omega' \quad (1.3)$$

where  $\nu$  is the kinematic viscosity, which is of the order of  $\sim \lambda \tilde{v}$ , where  $\lambda$  is the typical length scale and  $\tilde{v}$  is the velocity for the chaotic motions. For a critical velocity of accreting matter, turbulence sets in and the fluid velocity suddenly begins to exhibit large chaotic variations on arbitrarily short time and length scales. We can impose limits on the typical length and velocity,  $\lambda_{\text{turb}}$  and  $v_{\text{turb}}$  as follows: a) the largest turbulent eddies cannot exceed the disk thickness, hence,  $\lambda_{\text{turb}} \lesssim H$ , and b) the turnover velocity is unlikely to be supersonic since they would probably be thermalized by shocks, hence,  $v_{\text{turb}} \lesssim c_s$ , where  $c_s$  is the speed of sound in the medium. Thus, we can write the general expression for viscosity as

$$\nu = \alpha c_s H \quad (1.4)$$

where we expect  $\alpha \leq 1$ . In the seminal paper by Shakura & Sunyaev (1973), this  $\alpha$  parameter, defined to be the efficiency of the mechanism of transport of angular momentum, was first introduced. This parameter encourages a semi-empirical approach to the problem associated with uncertainties in modelling viscosity. We can also formulate  $\alpha$  to include viscosity due to winding-up of random magnetic fields in the disk.

Recent studies have shown that there exists a discrepancy between the  $\alpha$  values from modelling observations of fully ionized, time-dependent accretion disks ( $\alpha \approx 0.1 - 0.4$ ) and those obtained from numerical magnetohydrodynamic simulations, without the superimposed magnetic field ( $\alpha \leq 0.02$ ) (King et al., 2007). The underestimation from numerical simulations could be attributed to certain inherent numerical limitations. Attempts to reproduce accretion disk viscosity due to magnetic effects, as suggested by Balbus & Hawley (1991) with shearing box simulation has met with an underestimation of the value of  $\alpha$  parameter, even suggesting a resolution dependence of the value of  $\alpha$  (Fromang & Papaloizou, 2007; Nixon, 2015; Ryan et al., 2017). Dynamical evolution of self-gravitating accretion disks also seem to suggest that the  $\alpha$  viscosity cannot account for the entire evolution of the mass spectrum of a supermassive black hole, especially for an AGN disk (Kubsch et al., 2016). More recent analysis

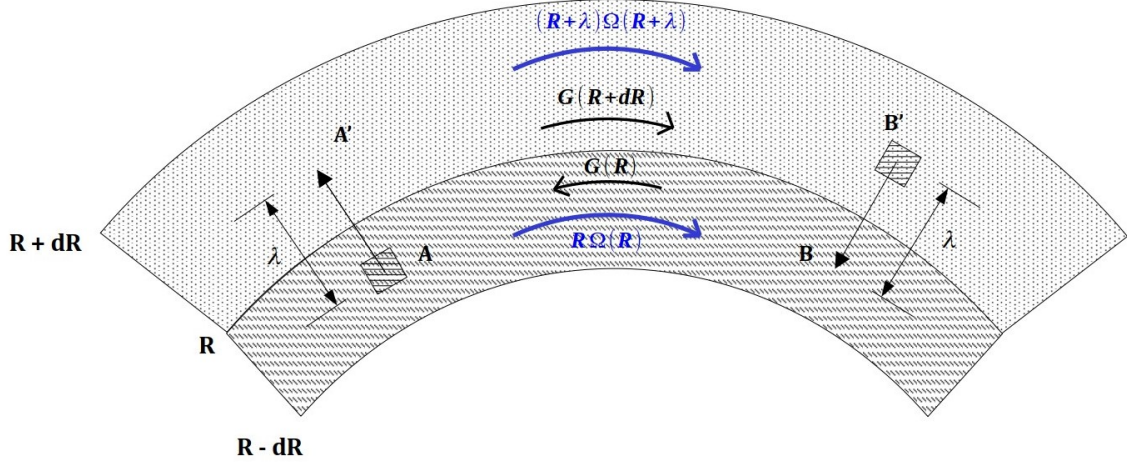


Figure 1.4: Viscous angular momentum transport and differential viscous torque in a shearing medium. The chaotic exchange of matter between adjacent layers cannot result in net mass transfer but the particles in adjacent layers carry different angular momenta (shown by blue curved arrows) which results in viscous torque being exerted on outer layer by inner layer. The inner layer thus, loses angular momentum to the outer layer and slowly spirals inward. The ring of gas between  $R$  and  $R + dR$  is subject to competing torques (shown by black curved arrows). The net torque leads to dissipation of energy within the gas.

of observational evidence suggests that an underestimation of the  $\alpha$  parameter depends on whether the disk is considered to be fully ionized or not (Martin et al., 2019). A fully ionized state of the disk may limit the turbulence upto transonic values, while the decrease of  $\alpha$  with decrease of ionization indicates that conduction and hence, magnetism plays an important role, providing a direct observational support for the magneto-rotational instability (MRI) driven hydrodynamic turbulence.

### 1.1.2 Radiation Spectrum of Accretion Disks

As matter loses its angular momentum and spirals in towards the accretor, it releases gravitational potential energy, a part of which goes into increasing the kinetic energy of rotation and the other part is radiated from the disk surface. The spectrum of this outgoing radiation is determined by the local disk structure and temperature which are determined from the mass accretion rate. The critical luminosity for which the radiation force on ionized material exactly balances the gravitational force is known as the Eddington luminosity,  $L_{\text{cr}} = 10^{38} M/M_{\odot} \text{ erg s}^{-1}$ . This critical luminosity sets the critical mass accretion rate value  $\dot{M}_{\text{cr}}$ , at which the total energy released in the disk equals the Eddington luminosity,  $L = \eta \dot{M} c^2 = L_{\text{cr}}$ . The total emitted spectrum of the disk is calculated by determining the spectrum emitted locally at each part on the disk surface and then integrating it over the entire disk surface.

In the simplest case, if the disk is optically thick, then each element of the disk radiates as a black-body with temperature  $T_s(R)$ . The kinematic viscosity  $\nu$  generates heat dissipation in the disk at a rate

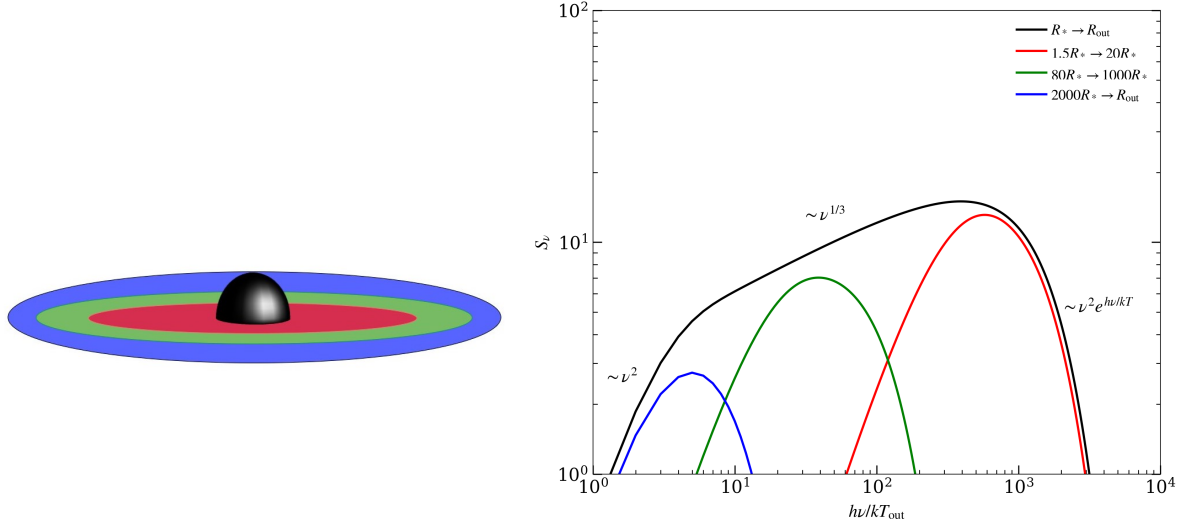


Figure 1.5: *Left:* A schematic of an accretion disk, where the coloured rings indicate the different zones contributing to the corresponding coloured spectra shown on the right. *Right:* Integrated emitted spectra of accretion disk radiating a local blackbody spectrum at each radius, with arbitrary units. The temperature at the outermost radius  $R_{\text{out}}$  is denoted by  $T_{\text{out}}$  and  $R_*$  corresponds to the innermost disk radius. The ‘flat’ part  $S_v \propto \nu^{1/3}$  makes this a characteristic accretion disk spectrum (black curve), giving the impression of a stretched-out blackbody, as is evident from looking at the contribution of the red (innermost), green (intermediate) and blue (outermost) zones of the accretion disk.

$D(R)$  per unit area per unit time, where  $D(R) = (3GM\dot{M}/4\pi R^3)[1 - (R_*/R)^{1/2}]$  and equating half of this (since we are considering emission from one side of the disk) to the total blackbody luminosity, we get

$$T_s = \left\{ \frac{3GM\dot{M}}{8\pi R^3 \sigma} \left[ 1 - \left( \frac{R_*}{R} \right)^{1/2} \right] \right\}^{1/4} \quad (1.5)$$

At large  $R$ , i.e.  $R \gg R_*$ , we find that  $T_s = T_*(R/R_*)^{-3/4}$ , where  $T_* = (3GM\dot{M}/8\pi R_*^3 \sigma)^{1/4}$  is the blackbody temperature on the surface of the accretor with radius  $R_*$ . Each elemental disk area emits the blackbody spectrum  $B_\nu(T_s) \propto \nu^3 [\exp(h\nu/kT_s) - 1]^{-1}$  and so, the spectrum of the disk as a whole is

$$S_\nu \propto \int_{R_*}^{R_{\text{out}}} B_\nu[T_s(R)] \cdot 2\pi R dR \propto \nu^{1/3} \int_0^{x_{\text{out}}} \frac{x^{5/3} dx}{e^x - 1} \quad (1.6)$$

where  $R_{\text{out}}$  is the outer disk radius and we have used the substitution  $x = h\nu/kT_s(R)$ , such that  $x_{\text{out}} = h\nu/kT_{\text{out}}$  and  $T_{\text{out}} = T_s(R_{\text{out}})$ . For frequencies in the range  $kT_{\text{out}}/h \ll \nu \ll kT_*/h$ , we can consider  $x_{\text{out}} \gg 1$  and so,  $S_\nu \propto \nu^{1/3}$ , the characteristic accretion disk spectrum first noted by Lynden-Bell (1969). For  $\nu \ll kT_{\text{out}}/h$ , the Rayleigh-Jeans tail of the coolest disk elements dominates and we have  $S_\nu \propto \nu^2$ .

At the outermost radius, where free-free and free-bound processes dominate (including absorption in the lines of heavy elements broadened by gas pressure), the radiated spectrum is a Planckian at the disk

surface. At intermediate radii, where Thomson scattering dominates, thermal equilibrium exists only at very large optical depths and the outgoing radiation is slightly distorted from the flat  $S_\nu \propto \nu^{1/3}$ . In the innermost regions, Compton processes dominate and the radiation spectrum has a Wien distribution. In addition to these radiative processes, the processes connected to magnetic fields and turbulence can generate non-thermal radiation at low frequencies (Lynden-Bell, 1969). The standard  $\alpha$ -prescription of accretion disks entails disk ‘flaring’ at large radii, making it possible for the disk surface to be exposed to the luminosity of the central source. This would require taking into account reprocessing of hard X-ray radiation in the observed spectra. Absorption of this hard radiation can also lead to subsequent evaporation of matter from the disk, leading to a decrease in the accretion rate, which would further decrease the hard radiation flux that is responsible for the evaporation of the outer disk layers. This type of autoregulating accretion mechanism was first mentioned by Shakura & Sunyaev (1973) and later studied in the context of Compton-heated disk winds by Shields et al. (1986) (hereafter S86). The accretion instability or oscillations studied by S86 forms the basic framework of our wind-driven relaxation cycle models in accretion disks, presented in Chapter 2.

### 1.1.3 Disk Winds

At high mass accretion rates (or  $L/L_{\text{Edd}} > 0.5$ ), disk winds become very important, having considerable impact on the evolution of disk structure. X-ray binaries have been found to exhibit absorption lines of highly ionized elements such as Fe XXV 6.67 keV and Fe XXVI 6.95 keV. These absorption lines indicate the presence of highly ionized material outflowing at moderate velocities  $\sim 500 \text{ km s}^{-1}$ . The theory of wind launching mechanisms are abundant and has been an active field of research for decades. UV radiation can be effective in driving a wind. In X-ray binaries where X-rays tend to ionize material, UV line-driving is important only when there is shielding from the X-ray irradiation. Proga & Kallman (2002) pointed out that strong ionizing X-ray radiation require unphysically high X-ray opacities in order to allow line driving. They alternatively suggested that the same X-ray irradiation can produce hot bipolar wind or corona above the disk. Depending on whether the thermal velocity of heated gas exceeds the local escape velocity, the evaporated photoionized plasma will either form a bound atmosphere/corona or be launched as a thermal wind (Begelman et al., 1983; Woods et al., 1996). The radiation force due to electrons can be very important for very luminous systems, leading to a thermal-radiative pressure mechanism to launch winds at radii well below the Compton radius (the radius at which the gas reaches Compton temperature  $T_{\text{IC}}$ , the temperature at which Compton heating and cooling rates balance out) (Proga & Kallman, 2002). In the presence of a strong toroidal magnetic field, magnetic pressure can

give rise to disk winds. These winds can also be launched at well below the Compton radius (Miller et al., 2006).

Detailed photoionization calculation codes like XSTAR (Mendoza et al., 2021) and CLOUDY (Ferland et al., 2017) are capable of modelling absorption and emission features in simulated plasmas. We also have several spectral fitting codes such as XSPEC (Arnaud, 1996) and SPEX (Kaastra et al., 1996) that can model absorption features along a line of sight, including ions with small cross-sections. From the observation point of view, neutron star and black hole X-ray binaries exhibit multiple narrow absorption features that indicate a wind launching radius consistent with Compton radius and hence, a thermal launching mechanism for these winds (Allen et al., 2018; Gatuzz et al., 2019). Radiation pressure due to electron scattering has been observed to play an important role as gas becomes more photoionized with increased luminosity thus, supporting thermal-radiative disk wind models (Díaz Trigo et al., 2014). The detection of a series of outbursts in black hole X-ray binaries indicate strong disk winds that correspond to magnetic driving instead of thermal (which require very specific radiative conditions) (Tetarenko et al., 2018). Observations also suggest an anti-correlation between jets and winds, whereby jets are able to carry away enough matter from the disk to halt matter flow into the radio jet (Neilsen & Lee, 2009). It is expected that high resolution calorimeters in the future will provide means to constrain accretion flow dynamics, providing more insights into the wind launching mechanisms involved.

## 1.2 X-ray Binaries

X-ray binaries (XRBs) were one of the first objects that helped us determine accretion to be a significant power source in astrophysical objects. A majority of stars are members of binary systems, which at some stage of their evolution, undergo mass transfer. Two of the primary modes of mass transfer in such binaries can be described as follows: a) *Roche lobe overflow*, where one of the stars in the binary may either increase in radius or the binary separation may decrease such that the accretor is able to pull matter from outer layers of the companion star; b) *Stellar wind accretion*, where one of the stars may eject matter in the form of stellar wind, which is gravitationally captured by the accretor (Frank et al., 2002). In most cases, the transferred matter cannot land onto the accreting object until it has lost most of its angular momentum. This leads to the formation of accretion disks, which are an efficient method of converting gravitational potential energy into radiation. XRBs generally comprise of an X-ray luminous double star system, where an optically bright star (donor) is accompanied by a very compact accretor such as a black hole (BH) or a neutron star (NS). Disk winds from accretion disks can be launched

via thermal, radiative and/or magnetic driving. Radiation in the ultraviolet part of the spectrum may contribute to line driving in winds. In XRBs, however, the X-rays tend to photoionize the material thus, reducing the concentration of ions capable of UV line driving. In turn, the X-ray heating can lead to temperatures  $\sim 10^7$  K and potentially drive thermal winds. The upper layers of the accretion disks are expected to puff up into an atmosphere, corona or wind (Díaz Trigo & Boirin, 2013).

The observation of blueshifted absorption lines in NS and BH XRBs provide good evidence for the existence of outflowing material. The presence of broad emission lines has also been attributed to the combination of line blending, Doppler broadening and Compton scattering in an accretion disk corona or hot atmosphere. Additionally, most XRBs present time variable characteristics. Black holes in XRBs exhibit a hysteresis in their spectral/timing properties, which is commonly known as the *q-diagram* (see Figure 1.6). The trend outlines the global evolution of accretion disk properties with the change in mass accretion rate. The study of spectral timing properties thus, enables us to understand the accretion flow properties on a large scale. Recent studies of fast spectral variability can also improve our understanding of Quasi-periodic oscillations (QPOs) in XRBs.

### 1.2.1 State Transitions

The first extensively studied X-ray source, the black hole binary (BHB) Cyg X-1, depicted two very different spectral shapes (see Figure 1.6) indicating very different characteristic photon energy of the source output. The ‘high’/‘soft’/‘thermal-dominant’ state was characterized by a soft component below  $\sim 10$  keV and a complex non-thermal tail of emission extending to  $\gtrsim 500$  keV (Gierliński et al., 1999). The second spectral state, termed ‘low’/‘hard’ state, peaked at  $\sim 100$  keV and is accompanied by a low temperature disk component. With increasing spectral coverage of observations, the nomenclature of spectral states has significantly evolved with time. The bolometric luminosity of the source was later shown to not change much with the change in spectral states and eventually, the discovery of the hysteresis (Nowak, 1995) led to the terms ‘hard’ and ‘soft’ being used to refer to the spectral states instead of the intensity. The diagrams often depict the high/soft state, where ionized absorbers with velocity  $v < 1000 \text{ km s}^{-1}$  are detected, and the low/hard state, in the absence of such absorbers (Fukumura et al., 2020). With an increased number of data from transient BHBs, newer varieties of spectral states have come to light.

The X-ray irradiation from the central source and the consequential radiation pressure may drive strong disk winds that lead to depletion of matter from the inner parts of the disk, thus, leading to quenching of the accretion disk. It is believed that this process is associated with the abrupt end in the

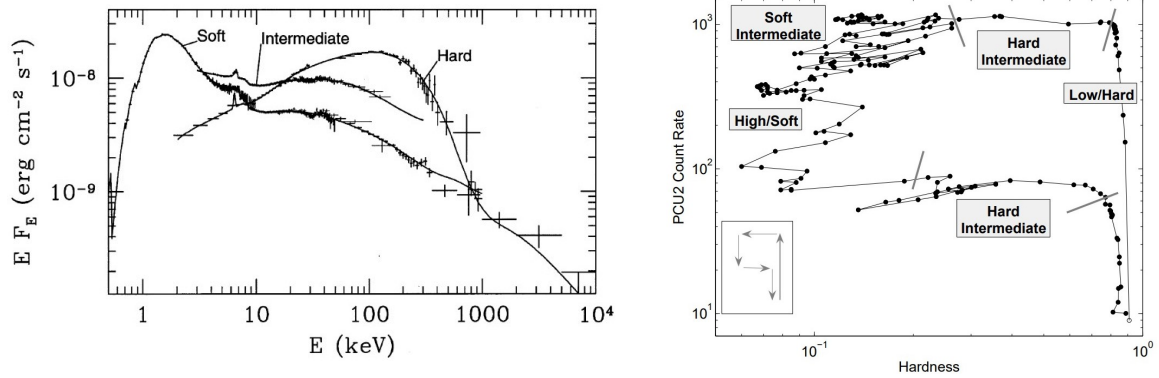


Figure 1.6: *Left*: X-ray spectral states of Cyg X-1 from Gierliński et al. (1999). *Right*: Hardness-intensity diagram of the 2002/2003 outburst GX 339-4 showing the ‘q-shaped pattern/hysteresis’ (Belloni, 2005)

outburst phase of such sources. High-resolution *Chandra* spectra of BH LMXB 4U 1630-47 showed that the absence of absorption lines in the soft-to-hard transitional state can be associated with the disappearance of wind either due to an accelerated flow or quenching of plasma during the soft state (Gatuzz et al., 2019). Geometrical effects such as disk truncation and a hot, optically thin, geometrically thick inner accretion flow are associated with the hard state, whereas the soft state is associated with an optically thick, geometrically thin accretion disk.

### 1.3 Active Galactic Nuclei

Our galaxy comprises of H II regions, planetary nebulae, nova and supernova shells, and these regions have been observed and studied in other galaxies as well. In spiral and irregular galaxies, H II regions occur as largest and most luminous gaseous nebulae, and are formed by ionization of interstellar gas by young O and B stars. For the most part, these regions form far from the galactic nucleus in the outer parts of the system. A very small minority of galaxies comprise of ionized matter in their nuclei that is not associated with O and B stars. These include Seyfert galaxies, radio galaxies, quasars, and quasistellar objects and are collectively called active galactic nuclei (AGNs). They are quite rare, distant and faint but the ionized gas within them emits a prominent emission line spectrum. Their typical luminosity is  $\sim 10^{12} L_{\odot}$  which requires that the central source be of mass  $M > 3 \times 10^7 M_{\odot}$ . Every spectral band from the radio, far infrared, through optical and ultraviolet, to the X-ray and  $\gamma$ -ray regions have led to the original unification scheme (Antonucci, 1993, and references therein, see also Figure 1.7). An AGN has been theorized to be comprised of an axisymmetric dusty structure (dubbed the ‘torus’) with column density large enough to obscure the central source in some directions. The central engine also launches

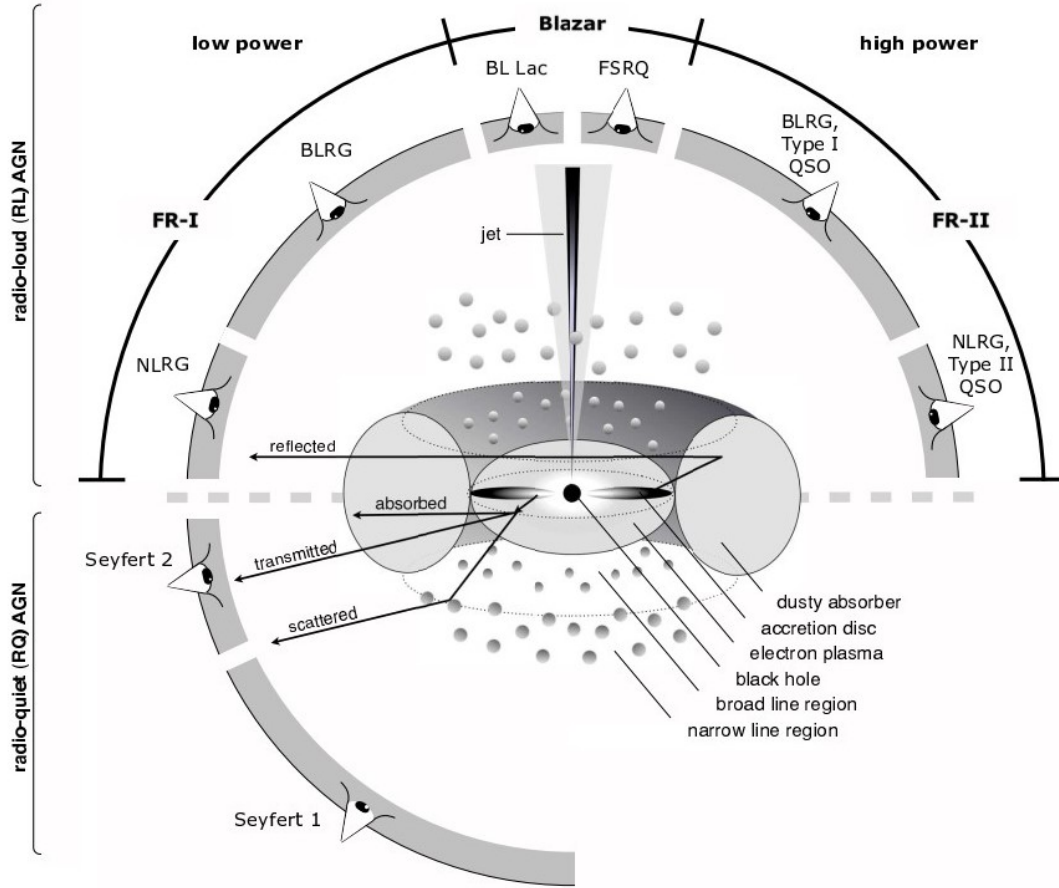


Figure 1.7: The unified model of Active Galactic Nuclei (AGNs). *Image credit:* Beckmann & Shrader (2012)

powerful jets aligned with the symmetry axis of the system, observed in some 10% of high ionization AGNs (Netzer, 2015). Furthermore, the central object is also surrounded by a rotating accretion disk of inflowing matter. Some orientation model (unification in terms of different inclination angles of line of sight) attribute outflowing winds driven off the disk surface to the presence or absence of emission and absorption components.

The unification in terms of observational signatures identifies mainly two regions: a) broad line region (BLR) is a compact (diameter  $d \approx 0.1$  pc) and dense (mean  $n_e \approx 10^{10} \text{ cm}^{-3}$ ) region producing permitted emission lines; b) narrow line region (NLR) spans much larger distances ( $d \approx 10^2$  pc) with much less density (mean  $n_e \approx 10^4 \text{ cm}^{-3}$ ) and produces characteristic emission lines covering a wide range of ionization. It is well known that a supermassive black hole is required as the central engine and a sufficient supply of matter is necessary to fuel it. However, there is considerable mystery surrounding how this fuel gets to the nucleus with practically zero angular momentum on galactic scales. Another area of interest with regards to AGNs is the essential role it plays in the evolution of its host galaxy.



The feedback from an AGN can both suppress or promote star formation rate in the host galaxy. One of the primary modes of such feedbacks are highly ionized fast AGN winds or outflows (more on this in §§1.3.1). Radio jets originating near the poles of the central object with ‘bubbles’ extending up to 10 kpc-10 Mpc, can also influence intergalactic medium via rapid heating and huge amounts of transfer of outward momentum.

### 1.3.1 AGN Outflows

Over 50% of nearby AGNs show evidence for outflows that carry significant amount of kinetic energy constituting a large fraction of the AGN power. Gas from the central accretion disk or other large mass reservoir, that is exposed to strong radiation field from the central source can be transformed to large scale flows. If the flow is continuous, they are classified as ‘winds’. They can also be ejected in the form of ‘clouds’ or ‘condensations’. The equation of motion for a cloud of mass  $M_c$  can be written as

$$a(r) = a_{\text{rad}}(r) - g(r) - \frac{1}{\rho} \frac{dP}{dr} + \frac{f_d}{M_c} \quad (1.7)$$

where  $a(r)$  denotes the acceleration of the cloud, and it equals the sum total of gravitational acceleration  $g(r)$ , acceleration due to radiation pressure force  $a_{\text{rad}}(r)$ , and the drag force  $f_d$ ; and  $P$  is the total pressure (gas pressure + radiation pressure). For pure wind flows, we can neglect the drag force term and the internal radiation pressure, and obtain

$$v \frac{dv}{dr} = a_{\text{rad}}(r) - g(r) - \frac{1}{\rho} \frac{dP_g}{dr} \quad (1.8)$$

Additionally, the mass continuity equation gives

$$\dot{M} = 4\pi\rho r^2 v C_f(r) = \text{const.} \quad (1.9)$$

where  $C_f(r)$  is the location dependent covering factor of the outflowing gas (Netzer, 2008). For low ionization and large column density of gas, gravitational acceleration dominates, while the motion of ionized, low optical depth gas is heavily affected by radiation pressure force. For fully ionized gas, only electron scattering contributes to the pressure. In the regime  $a_{\text{rad}} \ll g(r)$ , pressure gradient is dominant for a high ionization, high temperature gas.

Observationally, absorption line profiles provide a wealth of information regarding the nature of these outflows. The UV absorption lines indicate velocities in the range of a few factors of  $10^2 -$

$10^4 \text{ km s}^{-1}$ , whereby the high velocity indicates gases originating much closer to the central black hole and accretion disk. The X-ray lines with velocity in the range of a few factors of  $10^2 \text{ km s}^{-1}$  indicate slower absorbers located much farther out. Figure 1.8 shows the spatial extent of the different outflows that have been detected in an AGN - a ‘unified AGN outflow model’ per se. The outflows are currently classified as follows:

- **Broad and narrow absorption lines (BALs and NALs)** - an AGN UV absorption line can be classified as broad if the velocity full-width at half maximum  $> 3000 \text{ km s}^{-1}$  and blueshifted velocity  $> 5000 \text{ km s}^{-1}$ . The narrow absorption lines typically have blueshifted velocity  $< 4000 \text{ km s}^{-1}$ , although in exceptional cases they reach  $\sim 10000 \text{ km s}^{-1}$ . The mini-broad absorption lines have intermediate values between those of broad and narrow lines. In the case of BALs, the highest outflow velocities are correlated with quasar luminosity as is expected for a radiation-pressure driven outflow model. They also depict a reddened spectra indicative of high columns of gas and dust (Laor & Brandt, 2002) and they vary on timescales of a year or shorter. The NALs have been found to be associated with radio emission (Knigge et al., 2008). These outflows can be spatially resolved and hence, their location and mass loss rates can be relatively easily estimated for nearby AGNs (Das et al., 2005), but due to their low velocities, any contribution to AGN feedback is insignificant.
- **Warm absorbers (WAs)** - Detected as absorption lines and edges from H- and He- like ions of C, O, N, Ne, Mg, Al, Si, and S in the soft X-ray spectra, these absorbers indicate an outflow velocity of  $v \approx 100 - 2000 \text{ km s}^{-1}$ . The lines have also been detected to be asymmetric with an extended blue wing (Kaspi et al., 2002), with deep absorption troughs. The WAs are estimated to have a low ionization and high mass loss rate (Sako et al., 2001; Laha et al., 2016), although their low velocities are not enough to significantly contribute to feedback processes. High resolution X-ray spectroscopy has successfully been able to estimate the density  $n_e \approx 10^4 - 10^{11} \text{ cm}^{-3}$  and the distance to within  $0.01 \lesssim r \lesssim 10 \text{ pc}$  for these absorbers. Similar to BALs, they are rarely found to be associated with radio-loud galaxies.
- **Ultrafast outflows (UFOs)** - These are a relatively new class of outflows being detected by extremely improved sensitivity and spectral resolution of space-based telescopes like Chandra, XMM-Newton and Suzaku. These UFOs, as their name suggests, may sometimes have velocities as high as 30% of the speed of light and are detected as highly ionized winds via Fe XXV and Fe XXVI K-shell absorption lines. Almost 40% of nearby AGNs show evidence for the presence of UFOs. They carry kinetic energy greater than 0.5% of the continuum luminosity, and hence, suggest that they can deposit considerable kinetic power required for AGN feedback. Since these are highly ionized outflows,

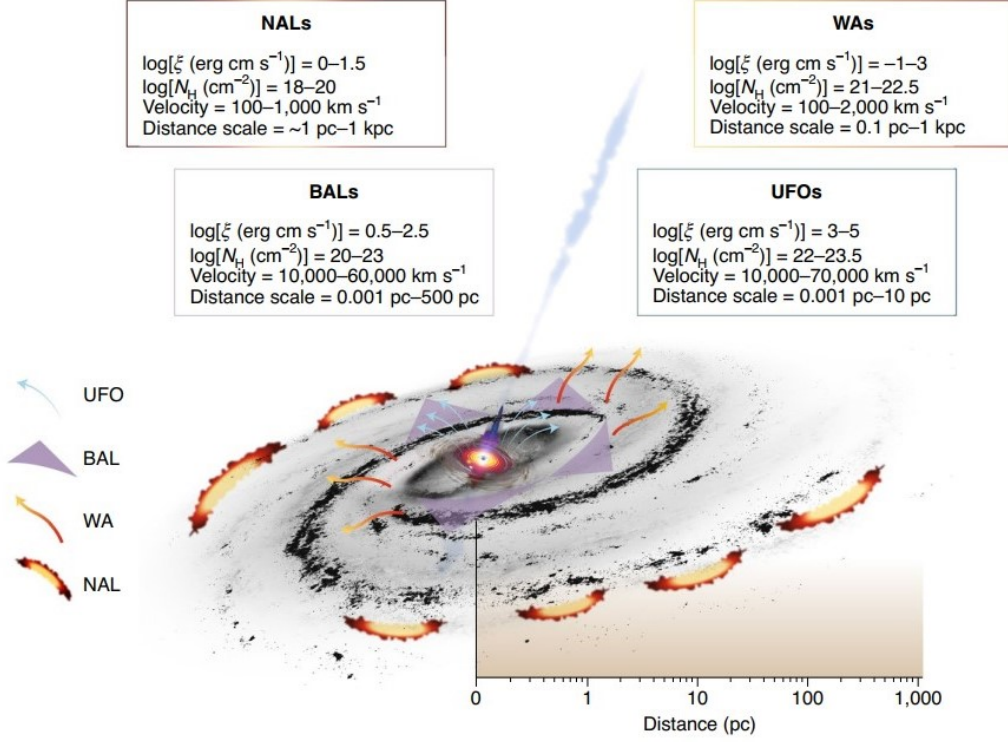


Figure 1.8: The average physical parameters of ionized outflows in AGNs. This image shows the relative spatial extent of the outflows and, in a way, depicts a ‘unified model of AGN outflows’ detected so far. *Image credit:* Laha et al. (2021).

radiative driving would be insufficient as a launching mechanism and hence, magnetohydrodynamic effects in accretion disks need to be considered. They are estimated to be located at  $10^2 - 10^4 r_s$ , where  $r_s$  is the Schwarzschild radius of the central supermassive black hole. Although a strong correlation is yet to be found, it has been suggested that UFOs can originate at the base of radio jets (Ghisellini et al., 2004).

### 1.3.2 Spectral Energy Distribution of AGN

The spectral energy distribution (SED) is used to describe the characteristic spectral signatures of AGNs in several wavelength bands. The monochromatic luminosity per unit frequency ( $L_\nu$  erg s<sup>-1</sup> Hz<sup>-1</sup>) or per unit energy ( $L_E$  erg s<sup>-1</sup> erg<sup>-1</sup>) or per unit wavelength ( $L_\lambda$  erg s<sup>-1</sup> Å<sup>-1</sup>) are some of the common forms of expressing the SED, while the equivalent monochromatic fluxes ( $F_\nu$ ,  $F_E$  or  $F_\lambda$ , containing an additional unit of cm<sup>-2</sup>) are used to describe the observed properties. The SED of many AGNs can be described over a limited range as

$$L_\nu \propto \nu^{-\alpha} \quad \text{or,} \quad L_\lambda \propto \lambda^{-\beta} \quad (1.10)$$

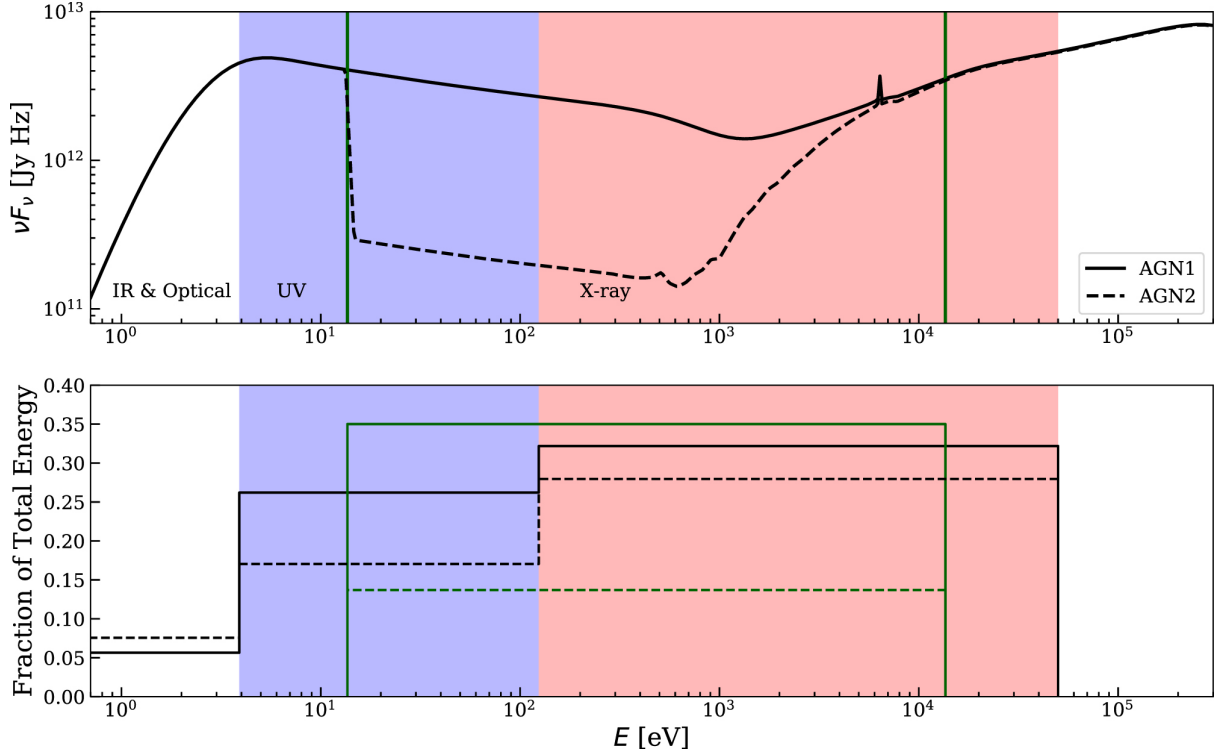


Figure 1.9: Obscured (AGN1) and unobscured (AGN2) AGN SEDs of NGC 5548 studied in Dannen et al. (2019) (top panel). The UV (blue) and X-ray (red) energy bands are shaded and the bottom panel shows the fraction of the total energy of SED in each energy component band for AGN1 and AGN2.

where  $\alpha$  is the frequency spectral index and  $\beta$  is the wavelength spectral index, and  $\beta = 2 - \alpha$ . AGNs emit roughly equal amounts of energy throughout the major part of the electromagnetic spectrum, extending from  $> 100 \mu\text{m}$  in the far-infrared (FIR) to  $> 10 \text{ keV}$  in the hard X-ray. Roughly 10% also emit strongly at radio wavelengths and a significant fraction of these are strong  $\gamma$ -ray sources (Wilkes, 2004). The number of compiled AGN SEDs in the literature includes many individual sources, at both low and high redshifts (Kolman et al., 1991; Kuhn et al., 1995; Kriss, 1988; Elvis et al., 1994; Lawrence et al., 1997; Tripp et al., 1994). However, the single power law approximation as shown above fails over a wide range of wavelengths and only a fraction of the physically relevant SED energy range can actually be observed.

The interaction of the AGN SED with the gas in its vicinity affects its dynamics. For example, the triggering of thermal instability of gas under the influence of an AGN SED has been extensively studied (Kallman & McCray, 1982; Krolik, 1999; Mehdipour et al., 2016; Dyda et al., 2017). For the purpose of our work, we particularly consider the unobscured AGN SED NGC 5548, which has been extensively studied in a multi-satellite campaign (from near-infrared to hard X-rays) and depicts a persistent state of heavy absorption (Mehdipour et al., 2015). This unexpected phenomenon has been determined to be caused by an outflowing stream of weakly ionized gas (called the obscurer), extending from the

vicinity of the accretion disk to the broad-line region (BLR). Both the obscured and unobscured SEDs were studied in the context of photoionization calculations of radiation force due to spectral lines in AGNs by Dannen et al. (2019). Figure 1.9 shows the two SEDs indicating time evolution of the SED and hence, gas dynamics due to material moving between the AGN and our line-of-sight (LOS). The AGN1 is the unobscured, intrinsic SED of the AGN, while AGN2 is the AGN SED through a column density of material  $N_H = 1.45 \times 10^{20} \text{ cm}^2$ . We will discuss the radiation heating/cooling rates and the corresponding thermal stability of the gas in more detail in § 3.4, in the context of our line profile calculations.

## 1.4 Thesis Outline

The primary subject of this dissertation is the study of outflows and disk winds in the vicinity of astrophysical sources like active galactic nuclei and X-ray binaries. Outflows and disk winds either directly affect the system in which they originate, or carry away energetics from the system and deposit them onto the surroundings. Our approach towards studying outflows is two-fold – (i) to directly quantify the extent in which disk winds regulate accretion flows, thus, causing variations in the continuum luminosity, and (ii) to develop methods to incorporate photoionization calculations in hydrodynamic simulations as a means to generate synthetic absorption line profiles due to parsec-scale thermally driven outflows.

This dissertation is arranged in the following order: Chapter 1 provides an introduction to XRBs and AGNs, winds/outflows in them and the essential observational aspects relevant to the study of dynamics of these winds/outflows. In Chapter 2, the results of our analysis of the wind-driven relaxation cycle models are presented. Following this, Chapter 3 discusses AGNs and their outflows, focussing primarily on thermally-driven outflows and thermal instability. We then present the synthetic absorption line profiles. Finally, Chapter 4 presents a general discussion of the relevance of our work in the current context and ways to take it forward.

## Chapter 2

### Wind-driven Relaxation Cycles in Accretion Disks

In this chapter, the results from Ganguly & Proga (2020) are discussed. The outline for this chapter is as follows: A brief introduction of the problem is presented in § 2.1, followed by the analytical results in § 2.2 as presented in S86. We then present our modified thermo-radiative wind model, and the numerical methods employed in § 2.3. Finally, § 2.4 discusses the main results of our analysis and its relevance in a broader context, such as the explanation of state transitions, and § 2.5 presents some concluding remarks pertaining to this work.

#### 2.1 The Problem

For the standard  $\alpha$  disk model, it is well-known that the disk flares in thickness near the outer edges, exposing the surface of the disk to irradiation from the central source luminosity. The irradiating X-ray photons induce photoionization heating, which is balanced by line cooling such that the disk gas temperature has an ambient value of  $\sim 10^4$  K. If however, the gas is relatively tenuous, the continuum intensity  $J$  will induce a large ionization parameter value  $\Xi' \equiv 4\pi J / pc = p_r / p_g$ , where  $p_r$  and  $p_g$  are the radiation and gas pressures in the disk. This  $\Xi'$  increases with height above the disk, until it reaches a critical value  $\Xi'_{c,\max}$ , where Compton heating and photoionization heating exceed radiative cooling and the gas undergoes runaway heating towards a Compton temperature  $T_{IC} = \langle \epsilon \rangle / 4k \approx 10^8$  K, where  $\langle \epsilon \rangle = L^{-1} \int_0^\infty h\nu L_\nu d\nu$  is the mean photon energy. If thermal conduction is significant, this happens for  $\Xi' < \Xi'_{c,\max}$ .

At  $R \gtrsim 0.1R_{IC}$ , the scale height of the hot corona  $H_c \geq 0.1R$ , so that the hot gas is able to flow away in the form of a wind (here  $R_{IC} \equiv GM\mu/kT_{IC}$  is the Compton radius). For a given luminosity, this wind can be so vigorous that the mass loss rate in the form of wind  $\dot{M}_w$  exceeds greatly the mass accretion rate  $\dot{M}_a$ , so that  $C \equiv \dot{M}_w / \dot{M}_a \gg 1$ . This can substantially modify the accretion supply rate and have significant effect on the spectrum and overall evolution of the system. For a sufficiently large  $C$ , the steady accretion flow may be unstable and there could be subsequent oscillations in the mass accretion rates.

For a constant rate of mass supply to an accretion disk, time variability could be attributed to spatial and temporal variations in the disk structure or the strength and configuration of the disk magnetic field,

in addition to a variety of local instabilities such as convective, thermal or magneto-rotational instability (Balbus & Hawley, 1998; Fromang & Lesur, 2019), and several non-local processes. The large radial extent of accretion disks imply a huge variation in the local escape velocity throughout the disk. A strong wind can hence, be launched from outer disk radii which causes a disruption in the accretion flow. When information about this disruption reaches the inner disk, it changes the local emission which, in turn, affects the disk irradiation. Thus, the radiation from the inner disk acts as a coupling between the inner and outer disks. The self-irradiated disk is an example of a “self-regulated accretion” process with feedback S86. Figure. 2.1 shows a schematic of this model.

To assess the role of the Compton-heated corona and disk winds, we may define a variable  $\eta_w \equiv \dot{M}_w / \dot{M}_a$ , where  $\dot{M}_w$  and  $\dot{M}_a$  are the wind mass loss rate (at the outer disk region) and mass accretion rate onto an accretor, respectively. The ratio measures the efficiency of wind driving due to the accretion power and indicates how strongly the wind is coupled to the latter. The model of instantaneous response of wind-to-accretion and vice versa showed that a wind with  $\eta_w$  as low as one, destabilizes the disk (Begelman et al., 1983). However, taking the effect of viscosity into account, S86 found that the accretion at the inner disk edge responded much slower to the change in the disk surface density,  $\Sigma$ , at large radii. Viscosity stabilizes the disk by producing a “delay” or “relaxation time” to the propagation of perturbations throughout the disk. Therefore, a much higher  $\eta_w$  was needed to generate variability in the disk. In this paper, we study a more generalized model of disk wind coupling to accretion power. We look at the equations governing the evolution of a steady disk in the subsequent sections in order to study the behaviour of these oscillations.

### 2.1.1 Equations for Disk Evolution

The mass loss in the form of wind can be included in the source term  $S$  of the equation of continuity to give:

$$\frac{\partial \Sigma}{\partial t} = \frac{1}{2\pi R} \frac{\partial \dot{M}}{\partial R} + S(R, t) \quad (2.1)$$

$$\dot{M} = 6\pi R^{1/2} \frac{\partial}{\partial R} \left( \nu \Sigma R^{1/2} \right) \quad (2.2)$$

where  $\Sigma$  is the surface density,  $\dot{M}(R, t)$  the mass accretion rate, and  $\nu$  is the kinematic viscosity. The source term

$$S(R, t) = S_{\text{in}}(R) - S_w(R, t) \quad (2.3)$$

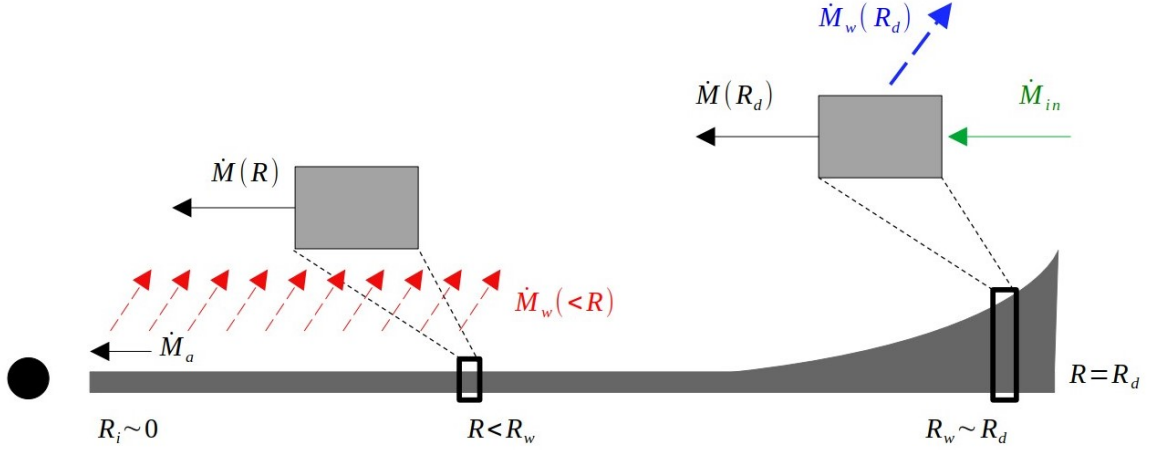


Figure 2.1: A schematic of mass accretion rates at different parts of the accretion disk around a compact object (the accretor, shown as a black circle on the left). Near the outermost disk radius, the disk flares and the net wind mass loss rate and (constant) mass supply rate result in the mass accretion rate  $\dot{M}(R_d)$  at steady state. Defining the wind mass loss rate at some radius  $R$  as a sink term integrated from the inner radius upto that radius, the mass accretion rate  $\dot{M}(R)$  is the resultant of the mass accretion rate at the inner radius of the disk  $\dot{M}_a$  and the net loss in the form of wind  $\dot{M}_w(<R)$ .

includes a steady mass injection rate  $S_{\text{in}}$  and a time-dependent mass loss rate  $S_w$  due to the wind.

Using the following dimensionless variables,

$$R_* \equiv \frac{R}{R_d}, \quad v_* \equiv \frac{v}{v_0}, \quad \dot{M}_* \equiv \frac{\dot{M}}{\dot{M}_{\text{in}}} \quad (2.4)$$

$$\Sigma_* \equiv \Sigma/\Sigma_0, \quad t_* \equiv t/t_0, \quad S_* \equiv \frac{SR_d^2}{\dot{M}_{\text{in}}} \quad (2.5)$$

where  $R_d$  is the disk radius,  $v_0$  is a characteristic viscosity; and the total mass injection rate is defined as

$$\dot{M}_{\text{in}} = 2\pi \int_0^{R_d} S_{\text{in}}(R) R dR \quad (2.6)$$

Here, we have also used the characteristic surface density  $\Sigma_0 \equiv \dot{M}_{\text{in}}/v_0$  and the viscous timescale corresponding to characteristic viscosity as  $t_0 \equiv R_d^2/v_0$ . Finally, using the coordinate transformation  $x = R_*^{1/2}$ , we get

$$\frac{\partial \Sigma_*}{\partial t_*} = \frac{1}{4\pi x^3} \frac{\partial \dot{M}_*}{\partial x} + S_*(x, t) \quad (2.7)$$

$$\dot{M}_* = 3\pi \frac{\partial}{\partial x} (x v_* \Sigma_*) \quad (2.8)$$

We adopt an ad hoc description for viscosity, such as  $v_* \propto R_*^a \Sigma_*^b$ . Two common approximations for



the viscosity law include: (a)  $\nu_* = R_*$ , an  $R$ -dependent viscosity first studied by Lynden-Bell & Pringle (1974), and (b) a general  $\alpha$ -model prescription, where the turbulent disk has an effective viscous stress assumed to be  $\alpha(p_r + p_g)$ , such that

$$\nu = \frac{2\alpha c_s^2}{3\Omega} = \frac{2\alpha\Omega H^2}{3} \quad (2.9)$$

where  $H = c_s/\Omega$  is the disk scaleheight, as defined before.

In a steady disk, the characteristic timescale for the accretion instability to persist is the diffusion timescale,

$$\tau_\nu \equiv \frac{R^2}{\nu^{(s)}} \quad (2.10)$$

where  $\nu^{(s)}$  is the viscosity in the steady (or unperturbed) disk. We can characterize the mass loss in the wind by

$$\dot{M}_w^{(s)}(< R) = 2\pi \int_0^R S_w^{(s)}(R') R' dR' \quad (2.11)$$

which we have considered to be independent of time for a steady disk. Thus, an essential parameter  $C(R)$  can be defined as the ratio of this mass loss rate to the central accretion rate as

$$C_R \equiv \frac{\dot{M}_w^{(s)}(< R)}{\dot{M}_a^{(s)}} \quad (2.12)$$

which at the outermost radius,  $R = R_d$ , can be written as

$$C \equiv \frac{\dot{M}_w^{(s)}}{\dot{M}_a^{(s)}} \quad (2.13)$$

In this work, we alternatively refer to this ratio as the wind efficiency,  $\eta_w$  (as introduced in § 2.1). While discussing or referring to the classic case studied in S86, we use the ‘ $C$ ’ notation for comparison. At any radius interior to the mass injection region, the mass conservation thus, gives

$$\dot{M}^{(s)}(R) = \dot{M}_a^{(s)} + \dot{M}_w^{(s)}(< R) \quad (2.14)$$

since  $S_{\text{in}} = 0$ . This is depicted in the Figure 2.1. Rewriting the above equation in terms of the previously defined parameters, we get

$$\dot{M}_*^{(s)}(R) = \frac{1 + C_R}{1 + C} \quad (2.15)$$

As  $\tau_\nu$  increases with radius, the inner regions of the disk can adjust to changes in  $\dot{M}$  due to mass input and wind loss at large disk radii. This implies that the radial mass flux must be independent of  $R$  in

the inner region. Since  $\dot{M}_a = \dot{M}(R_i)$  (where  $R_i$  is the innermost radius) must remain finite, we can adopt the inner boundary condition as

$$\frac{\partial}{\partial R}(\nu\Sigma) = 0 \quad (2.16)$$

provided  $R_i \sim 0$ . For an inner boundary condition of  $\Sigma = 0$  at some small but non-zero radius, gives the same result. The outer boundary of a disk with a strong wind is usually determined by determining the angular momentum loss in the wind, since the outer edge is where the angular momentum of the disk is lost. We can assume a zero mass flux condition at the outer edge as  $\dot{M}(R_d) = 0$ .

At steady state, the mass conservation relation applied to the disk, gives

$$\dot{M}_{in} = \dot{M}_a^{(s)} + \dot{M}_w^{(s)}, \quad (2.17)$$

where the superscript  $(s)$  denotes the steady state value. The expression for steady state mass accretion rate normalized to the mass input rate  $\dot{M}_{in}$  reads as,

$$\dot{M}_{a*}^{(s)} = \frac{1}{1+C}. \quad (2.18)$$

### 2.1.2 $\delta$ -function Wind at $R_d$

We now consider a more general disk with finite radial extent but a simple  $\delta$ -function wind launched from a ring of infinitesimal width at radius  $R_w$ . The mass loss rate is given by

$$\dot{M}_w(t) = C(\dot{M}_a)\dot{M}_a(t) \quad (2.19)$$

For disk radius  $R > R_w$ , the evolution is on a much longer timescale than the viscous time scales for  $R < R_w$  and hence, cannot participate in oscillations with timescales  $\lesssim \tau_v(R_w)$ . The outer boundary  $R_d$  is located at an infinitesimal distance from  $R_w$  and hence, the net influx of mass, proceeding from  $R_w$  towards smaller radii, is

$$\dot{M}(R_d, t) = \dot{M}_{in} - C(\dot{M}_a)\dot{M}_a(t) \quad (2.20)$$

The steady state solution has  $\dot{M}^{(s)}(R) = \dot{M}_{in}/(1+C)$  and there is a corresponding  $\Sigma^{(s)}(R)$ . If we consider an infinitesimal perturbation  $\delta\Sigma_* = \Sigma_*(R, t) - \Sigma_*^{(s)}(R)$  and  $\delta\dot{M}_* = \dot{M}_*(R, t) - \dot{M}_*^{(s)}(R)$ . The disk evolves such that

$$\frac{\partial}{\partial t_*}\delta\Sigma_* = \frac{1}{4\pi x^3} \frac{\partial}{\partial x}\delta\dot{M}_* \quad (2.21)$$

where,

$$\delta\dot{M}_*(x, t) = 3\pi \frac{\partial}{\partial x} (x v'_* \delta\Sigma_*) \quad (2.22)$$

and  $v'_* \equiv \partial(v_* \Sigma_*)/\partial\Sigma_*$  is the Lightman-Eardley stability parameter, such that the disk is stable against viscous diffusion, if  $v'_* > 0$ . Now, using the viscosity law  $v_* = R_*$  and  $y \equiv x^3 \delta\Sigma_*$ , the equations (2.21) and (2.22), become

$$\frac{\partial y}{\partial t_*} = \frac{3\partial^2 y}{4\partial x^2} \quad (2.23)$$

The corresponding inner and outer boundary conditions are  $y(0, t_*) = 0$  and

$$\frac{\partial y(1, t_*)}{\partial x} = -(1 + k_I)C \frac{\partial y(0, t_*)}{\partial x} \quad (2.24)$$

where  $k_I \equiv d \ln C / d \ln \dot{M}_a^{(s)} = d \ln C / d \ln L^{(s)}$ . We can absorb  $(1 + k_I)$  in  $C$ , for simplicity. Assuming a solution of the form

$$y = e^{i(kx - \omega t_*)} \quad (2.25)$$

which from equation (2.23) implies that  $i\omega = 3k^2/4$ , and hence,  $\omega_R = 3k_R k_I/2$  and  $\omega_I = 3(k_I^2 - k_R^2)/4$ , where subscripts  $R$  and  $I$  denote the real and imaginary parts of the quantities. The outer boundary condition implies that  $\cosh k_I \cos k_R = -C$  and  $\sinh k_I \sin k_R = 0$ . Since  $C > 0$ , we get  $k_R = (2n - 1)\pi$  and hence, for the lowest mode,  $k_R = \pi$ , marginal stability occurs when  $k_I = \pi$ . The corresponding value for  $C$  is

$$C_{\text{crit}} = \cosh \pi \approx 11.6 \quad (2.26)$$

For a large  $C_{\text{crit}}$ , we find that  $k_I \approx \ln 2C$  in the case of instability ( $\omega > 0$ ,  $C > C_{\text{crit}}$ ). For  $\Delta C = C - C_{\text{crit}} < C_{\text{crit}}$ , we have

$$\frac{2\pi\omega_I}{\omega_R} = \frac{2\Delta C}{C_{\text{crit}}} \quad (2.27)$$

The growth timescale  $\omega_I^{-1}$  is comparable with the period of the oscillation,  $P_* = 2\pi/\omega_R$ , when  $\Delta C \approx C_{\text{crit}}$ . Thus, for the lowest most rapidly growing mode ( $k_R = \pi$ ), we get

$$P_* \approx \frac{4}{3\pi} \frac{\ln 2C_{\text{crit}}}{\ln 2C} \approx 0.42 \quad (2.28)$$

i.e. the period is a weak function of  $C$ . Our finite radial extent disk shows that the  $C_{\text{crit}}$  is almost an order of magnitude higher than  $C_{\text{crit}} = 1$ , for the simple time-delay model which ignored viscous damping.

Carrying out similar analysis for a  $\delta$ -function wind, but at  $R_w < R_d$ , we will find that

$$C_{\text{crit}} \approx \frac{\cosh[(2n-1)\pi/x_w]}{\cosh[(2n-1)\pi(1-x_w)/x_w]} \approx e^{(2n-1)\pi} \quad (2.29)$$

For the lowest mode,  $C_{\text{crit}} \approx e^\pi$ , which is about the twice the value for the  $x_w = 1$  case. For  $n = 1$  and  $C = C_{\text{crit}}$  case, the period of oscillation is

$$P_* = \frac{2\pi}{\omega_R} = \frac{4x_w^2}{3\pi} = \frac{4R_w}{3\pi R_d} \quad (2.30)$$

## 2.2 Models

We consider a geometrically thin and optically thick disk with azimuthal symmetry and solve the diffusion equation that describes the disk evolution (Pringle, 1981; Lynden-Bell & Pringle, 1974). We primarily study two wind-launching models for comparison. The two models are described below.

### 2.2.1 Fixed Launching Radius at $R = R_d$

As in S86, we assume a constant rate of mass injection at the outermost disk radius,  $R_d$ , from an external source. The wind mass loss rate might not be a linear function of mass accretion rate. S86 considers such a possibility and they show based on their analytical treatment that for a power-law dependence,  $C \propto \dot{M}_a^{k_l}$ , where  $k_l$  is an arbitrary constant, the  $C_{\text{crit}}$  would be reduced by a factor of  $(1 + k_l)^{-1}$  (an analogous equation is eqn. (4.5) in S86). The case with  $k_l = 0$  corresponds to the case discussed above, where equation (2.18) gives the value of  $C_{\text{crit}}$ .

We can thus, express the mass loss rate in the following way:

$$\dot{M}_{w*} \equiv C' \dot{M}_{a*}^p \quad (2.31)$$

where any remaining constant of proportionality has been absorbed into  $C'$ , and  $p$  is an arbitrary constant exponent. Note that equation (2.31) reduces to equation (2.19) when  $p = 1$ . The requirement for the steady state condition becomes

$$\dot{M}_{a*}^{(s)} + C' (\dot{M}_{a*}^{(s)})^p - 1 = 0, \quad (2.32)$$

but this equation needs to be solved numerically.

### 2.2.2 Variable Launching Radius $R_L$

In the above analyses, a fixed wind launching radius has been assumed. However, in general, this may not be an ideal condition. We examine the effects of relaxing this assumption by allowing the radiation from the inner disk to irradiate the entire disk and causing reduced local escape velocity. We can express luminosity  $L$  in units of the Eddington factor  $\Gamma$ , such that  $L = \Gamma L_{Edd}$ , where  $L_{Edd}$  is the Eddington luminosity. Here we assume that the irradiation luminosity  $L$  of the disk equals to the total accretion luminosity. We express the coupling between the launching radius and  $\dot{M}_a$  using the following expression:

$$R_{L*} = 1 - \Gamma \frac{\dot{M}_{a*}}{\dot{M}_{a*}^{(s)}}, \quad (2.33)$$

where  $R_{L*}$  is the launching radius normalised to  $R_d$ . Our equation (2.33) is similar to equation (22) in Proga & Kallman (2002) that was derived for the launching radius of a Compton-heated wind, corrected for radiation driving. When  $\Gamma = 0$ ,  $R_L = R_d$  and we have the case studied by S86. The only numerical constraint is that  $R_L \geq 0$ .

Using their analytical method for the simplest case ( $\Gamma = 0$ ,  $p = 1$ ), S86 derived an expression for the period of oscillations as

$$P_* \propto \frac{R_L}{R_d} \quad (2.34)$$

We expect that in our variable  $R_L$  model, the disk stability condition and the variability period will be sensitive to  $\Gamma$ .

## 2.3 Numerical Methods

We assume azimuthal symmetry and perform 1D simulations along the radial direction. We have written a Python script to study the effects of self-regulated accretion as discussed in the previous section. The wind launching zone is a delta function, with mass loss taking place from a single radial grid zone.

$$S_{w*} = \frac{C\dot{M}_{a*}}{\pi(R_{j*}'^2 - R_{j-1*}'^2)} \quad (2.35)$$

where  $R_{j*}' = x_j'^2$  and  $x_j' = (x_j + x_{j+1})/2$ . Here  $R_j$  refers to the wind launching radius and  $R_{j*}'$  is the averaged launching radius value used to calculate  $S_w$ . The disk surface density  $\Sigma_*$  is assigned an initial

value of 0. We take  $\dot{M}_{in} = 1$ , since all mass rates are normalised to  $\dot{M}_{in}$  and together with eq. (2.35), calculate the source term  $S_*$ . The diffusion equation (2.7) is then solved using forward difference method while updating  $\Sigma_*$ . The boundary condition is obtained by imposing the condition that mass flux is finite and conserved at the disk edges, i.e.  $\partial(v\Sigma)/\partial R = 0$ .

Our resolution study shows that the calculated value of the accretion rate depends on the width of each radial zone. In particular, the variable  $\Gamma$  model is sensitive to smaller resolution in  $x$ ,  $N_x$  ( $N_x < 200$ ). Hence, for most of our models presented below, we use  $N_x = 200$  (see § 2.4 for more discussion).

To ensure that the value of  $\Sigma$  remains realistic at all times, it is quite common to impose the condition  $\Sigma_* = 0$ , whenever the numerical solution leads to  $\Sigma_* < 0$ . This condition is especially important when we deal with growing oscillations. Instead of allowing the disk to deplete completely, we introduce a floor value of 0.001 for  $\Sigma$ .

The initial condition is to set the disk surface density to be 0 and let matter diffuse from the surrounding source until the accretion disk reaches a steady state. We then perturb it by switching on the wind. In practice, we allow the system to reach  $(1 - \epsilon)\dot{M}_{a*}^{(s)}$ , where  $\epsilon$  is a very small number of the order of  $10^{-3}$ . It takes roughly 3 viscous time scales to reach this near steady state. We use the *fsolve* method in SciPy's (Python 3.6.7) optimization library to find the root of equation (2.32).

## 2.4 Results and Discussions

### 2.4.1 Fixed Launching Radius

First we checked the results from our simulations against the results presented in S86. Our resolution is higher than theirs by a factor of 10. This increased resolution does not considerably affect the key result although it does substantially reduce the amplitude of oscillation. This can be attributed to the fact that we have limited our analysis to a single zone wind regardless of the radial resolution. Namely, we still inject and eject the same amount of matter but now from a radial ring with smaller area. We find that  $C_{crit} \approx 11.3$  as opposed to 11.4 obtained by S86. Fig. 2.2 illustrates our results in a similar manner to the fig. 1 by S86. As expected, we observe damped oscillation for  $C < 11.3$  and growing oscillations for  $C > 11.3$ . We note that we consider only those oscillations to be stable whose amplitudes vary by less than  $10^{-4}$ . This condition is consistently followed throughout our analysis, and is used to classify the oscillations into categories.

In the growing oscillation case, the mass accretion rate grows until it saturates after some time. This saturation of oscillation is caused by the local surface density reaching negligible values or, in other

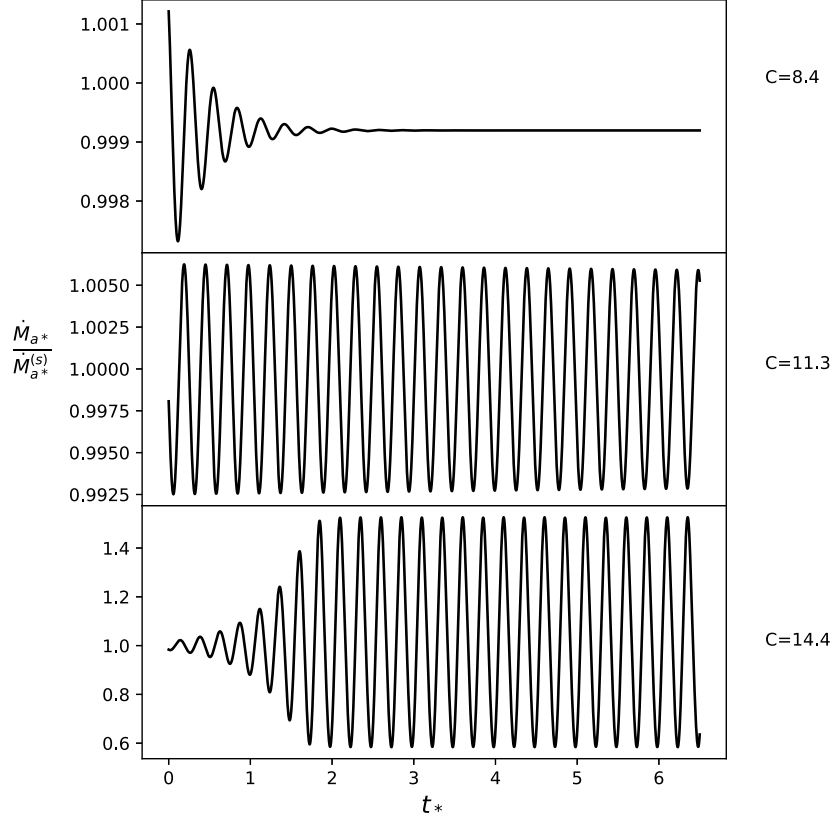


Figure 2.2: Central mass accretion rate (normalized to the steady state mass accretion rate) evolution of the disk for different wind strength parameter  $C$ . The top panel shows decayed oscillations in the disk, the middle panel shows the critical  $C$  case where the oscillation persists with constant amplitude. The bottom panel shows a growing oscillation phase, which saturates after some time due to local disk depletion.

words, complete depletion of matter from that region of the disk. We expect that if S86 continued their calculations to longer times, they would likely find the same behaviour. For  $C = 14.4$  shown above, our simulations showed that during this phase,  $\Sigma_{*,min}$  approaches 0, whereas  $\Sigma_{*,max}$  approaches 2.5 times its steady state value. The outcome of this instability is a small amplitude  $\dot{M}_{a*}$  oscillation but a large modification of the disk solution.

Table 2.1 summarizes the combination of  $p$  and  $C'$  (for  $\Gamma = 0$ ) values used in our simulations. The wind to accretion ratio sets the stability of the disk. The efficiency factor  $\eta_w$  is a function of time and hence, we consider the value of  $\eta_w$  at the beginning of the perturbation. The value of  $\eta_w$  decreases with increasing  $p$  with a slope of about -1 on a log-log plot (Fig. 2.3). This confirms the inverse relationship between  $\eta_{w,crit}$  and  $p$ , that demonstrates that the disk is easily destabilized if the wind is more strongly coupled to accretion (i.e. higher  $p$ ).

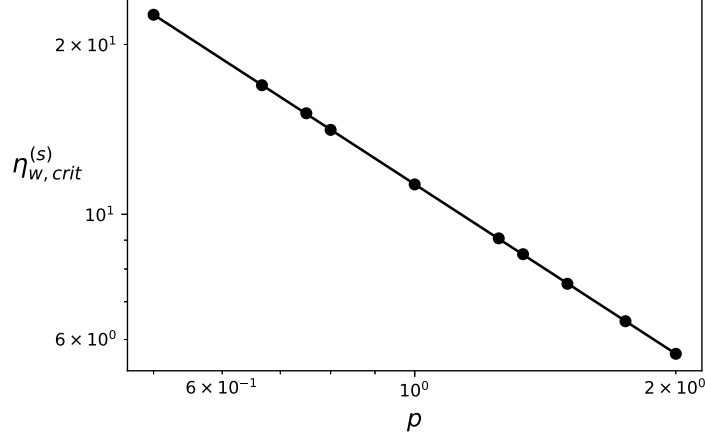


Figure 2.3: The critical wind efficiency  $\eta_{w,crit}$  as a function of the power-law index,  $p$ , in accordance with eq. (2.31).

$p$	$C'_d$	$C'_{crit}$	$C'_g$
0.5	4.5	4.95	5
2/3	6	7.05	7.5
3/4	8	8.6	9
4/5	9	9.5	9.9
1	11	11.3	14.4
5/4	18.5	20	24
4/3	21	22.8	24
3/2	20.5	26	30.5
7/4	37	39	40.5
2	30.5	48.5	50.5

Table 2.1: Summary of all parameters ( $C'$  and  $p$ ) used in simulations for the model described by eqn (2.31). The subscripts d, crit and g denote values of  $C'$  for which the oscillations decay, persist and grow, respectively. The value of  $C'_{crit}$  increases with increasing  $p$ . In Fig. 2.3, we use the corresponding  $C'_{crit}$  to plot the wind efficiency  $\eta_{w,crit}$ , which decreases with increasing  $p$ .

## 2.4.2 Variable Launching Radius

Table 2.2 contains our parameter survey for the variable  $R_L$  model. The  $\Gamma$  factor strongly controls and alters the outcome of disk evolution. In particular, we identified new cases for high  $\Gamma$  ( $\Gamma \geq 0.7$ ). In low  $\Gamma$  cases ( $\Gamma \sim 0.2$ ), we observe some deviation from the classical cases of stable oscillations.

We limit our presentation to 3 cases,  $p = 0.5, 1$  and  $2$ . The case  $p = 1$  corresponds to the special case studied in S86. The other two cases are representative of the lowest and highest  $p$  values considered (see Table 2.1). For  $0.001 \leq \Gamma \leq 0.1$ , the disk behaviour does not deviate much from the classical behaviour depicted in Fig. 2.2. However, for  $\Gamma \geq 0.2$ , we find some new results. We describe these cases in detail below.

- $\Gamma=0.2$  and  $0.3$ : We observe more than one  $C'_{crit}$  value resulting in stable oscillations. For example,



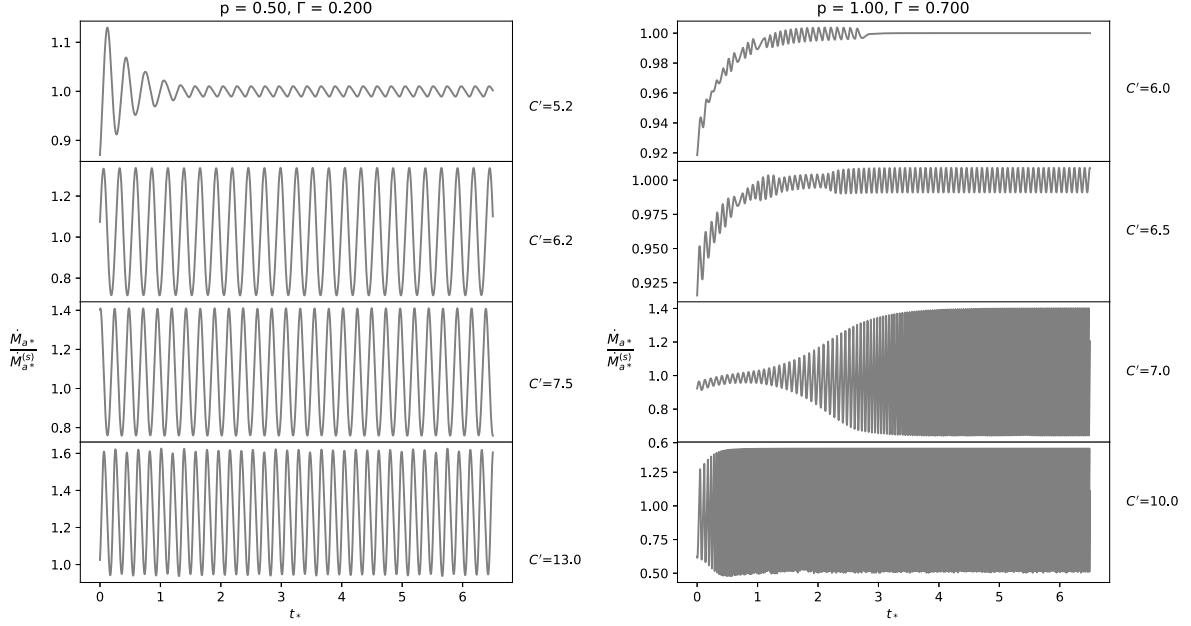


Figure 2.4: Examples of the time evolution of the accretion rate for (a)  $\Gamma = 0.2, p = 0.5$  (left), and (b)  $\Gamma = 0.7, p = 1$  (right), for various  $C'$ . *Left*: The top panel shows an example of an initial decay that is followed by a constant amplitude oscillation. The second, third and fourth panels depict the range of  $C'_{crit}$  that lead to stable oscillations. *Right*: The top three panels indicate a damped high amplitude oscillation superposed on the fundamental mode oscillating around the steady state value of 1. The lowest panel shows growing oscillations that saturate but has a very high frequency of oscillation, which increases with time.

constant amplitude oscillations occur when  $C'_{crit}$  is between 6.2 and 12. The lowermost panel on the left of Fig. 2.4 shows how the sinusoidal nature of the stable oscillations starts to change for  $C' \gtrsim 13$ . We also find that for increasing  $C'$ , the frequency of oscillation starts to increase. For  $\Gamma = 0.3$ , the results are similar to those of  $\Gamma = 0.2$ .

- $\Gamma = 0.4$ : For  $p = 0.5$  and  $p = 1$ , we find a single value of  $C'_{crit}$ . For  $p = 2$ , we see that  $C'_{crit}$  lies between 130 and 300. The range of  $C'_{crit}$  and the critical value of  $C'$  rise considerably.
- $\Gamma = 0.5$ : For all  $p$  values, we obtain single-valued  $C'_{crit}$ . We note that  $C'_{crit}$  for  $\Gamma = 0.5$  is less than that for  $\Gamma = 0.4$ . This result holds true for all three  $p$ -values investigated.
- $\Gamma = 0.7$ : Fig. 2.4 summarizes the distinct cases obtained for  $p = 1$ . We see that up to a certain value of  $C'$ , the accretion rate initially increases and at the same time oscillates with relatively high frequency and small amplitude. In the case of  $C' = 6.5$ , we see that eventually the fundamental oscillation dominates and steadies around 1. As  $C'$  increases, we see a growing oscillation that eventually saturates.
- $\Gamma = 0.9$ : The behaviour is similar to the  $\Gamma = 0.7$  case. For higher  $C'$ , the frequency increases rapidly with time.

The amplitude of oscillations in  $\dot{M}_{a*}$  remain constrained to  $\sim 50\%$  of its steady state value in all our

simulations. This can be mostly attributed to the amount of matter available to be launched as wind and also the constraint on the lowest possible launching radius. In all of the cases studied, the amplitude of oscillation increases for increasing  $\eta_w$ .

We have chosen a spatial resolution of  $N_x = 200$  for the above cases. Our resolution study showed that there are quantitative changes in most cases as well as qualitative changes in some of the extreme cases. For example, for  $p = 1, C' = 6, \Gamma = 0.7$ , the oscillations cease earlier for  $N_x = 400$ , while for  $N_x = 800$ , they persist for a longer number of time steps. In addition, the amplitude of oscillations also decrease with increasing resolution. For higher  $N_x$ , there is a clear tendency towards convergence. This resolution study was conducted for several other cases in our parameter survey. Convergence was evident for most cases with  $\Gamma \leq 0.7$ . For higher  $\Gamma$ , the behaviour was more erratic and unpredictable for different  $N_x$ . We restricted our  $N_x$  to 200 despite this fact, since the nature of oscillations and the feedback on  $\dot{M}_w$  remained unaffected from a qualitative perspective.

In Fig. 2.5, we show the steady state critical  $\eta_w$ - $p$  relation for various  $\Gamma$ . We find that the slope of this relation is nearly constant for  $\Gamma \leq 0.2$ . For higher  $\Gamma$ , the slope changes and more than one  $\eta_{w,crit}$  exists. For such cases we have shaded the region between all the possible straight line fits. For  $\Gamma > 0.5$ , oscillations are distinctly different from that of the classical cases and we cannot group them under simple categories (see above and the right panels of Fig. 2.4). We do not plot these points in Fig. 2.5 or list them in our table of classification of disk oscillations.

To visualize our results for the wind efficiency in a different way, we also plot steady state critical  $\eta_w$  as a function of  $\Gamma$  for different  $p$  values (the upper panel of Fig. 2.5, right). The curves for different  $p$  values generally resemble each other. For  $\Gamma \leq 0.2$ ,  $\eta_{w,crit}$  increases with increasing  $\Gamma$ . For higher  $\Gamma$ ,  $\eta_w$  decreases with increasing  $\Gamma$ , in all three  $p$  cases. To more directly compare the results for various  $p$ , in the bottom panel of Fig. 2.5 (right), we plot  $p\eta_{w,crit}$  vs  $\Gamma$ . For  $\Gamma < 0.1$ , we see that  $p\eta_{w,crit}$  is nearly constant, which is what we concluded from Fig. 2.3.

## 2.5 Conclusion

The study of disk winds in the context of state transition has evoked a lot of interest over the past decades (e.g. Fender et al., 2005; K rding et al., 2006). The wind launching mechanism and location may lead to time variability, the effects of which could be coupled to the signatures of mass accretion by the accretor. We explore this aspect through a self-regulated accretion disk. We found that our model is unlikely to explain state transitions in accretion disk spectra. However, it could be responsible for persistent small

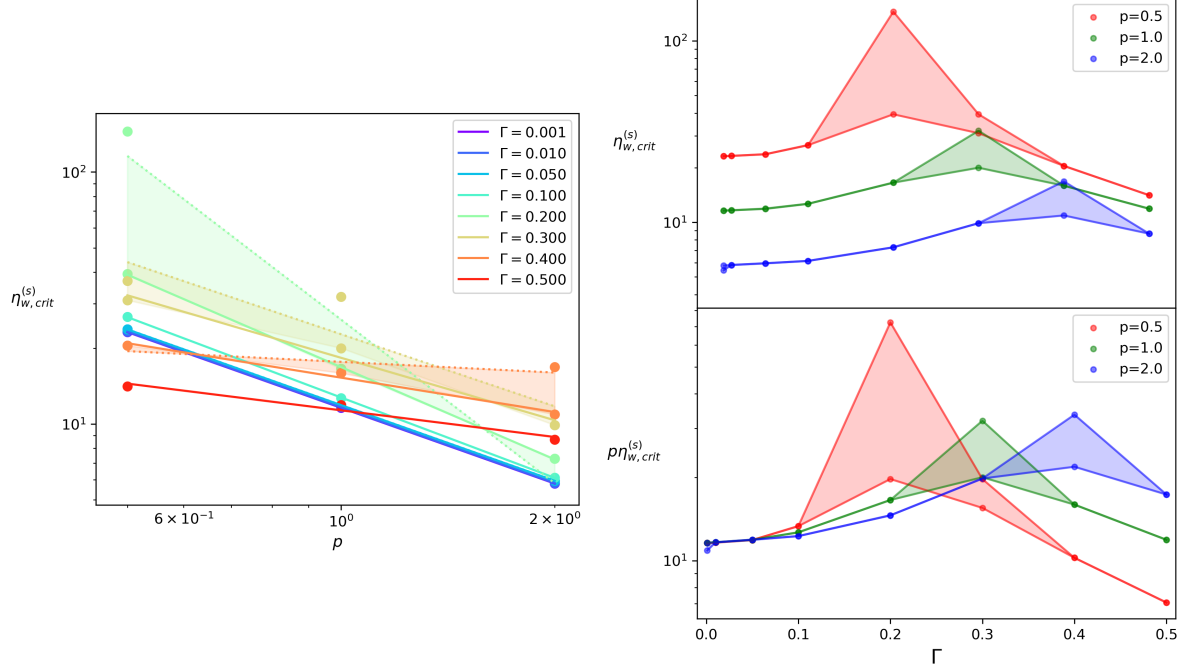


Figure 2.5: *Left:* The steady state critical wind efficiency  $\eta_w$  vs  $p$  for different  $\Gamma$  values. For some  $\Gamma$ , stable oscillations occur not just for a single value of  $\eta_w$ , but for a range of  $\eta_w$  (see Fig. 2.4 for some examples, e.g. second, third and fourth panels there). We shaded the regions for  $\Gamma$ 's where this happens. *Right:* The steady state critical wind efficiency  $\eta_{w,crit}$  vs  $\Gamma$  for different  $p$  values (top panel). In the bottom panel, we plot  $p\eta_{w,crit}$  vs  $\Gamma$  for different  $p$  values. Once again, the shaded region highlights the possible  $\eta_{w,crit}$  values for a particular combination of  $p$  and  $\Gamma$ .

amplitude regular single-mode oscillations in the mass accretion rate. Admittedly, our treatment is very simple. We use one viscosity law in all our analyses,  $v_* = R_* = x^2$ . We did not consider thermodynamic effects. We also did not incorporate magnetic fields in our analysis. Moreover, we assumed a  $\delta$ -function model for the wind, which exaggerates the role of mass removal.

Despite the simplifications, this analysis might be a stepping stone towards developing models that can account for the existence of state transition signatures in accretion disks. Time variability in accretion rates may be explained by physical processes considered here. They are rich in features and may hold the key to understanding the coupling forces operating in an accretion disk. For example, the study of GRS 1915+105 by Neilsen et al. (2011) is a very detailed analysis in that direction. They nicknamed the oscillations in X-ray spectra as the ‘heartbeat’ state and conducted a study of the geometry of the accretion disk using the X-ray continuum and emission lines in the optical spectrum. They demonstrate a strong correlation between mass loss in the form of wind and oscillations in the accretion rate that would explain the long-term effects in the disk.

A study of the same source, GRS 1915+105, by Zoghbi et al. (2016) considered in detail the reflection spectrum during the oscillatory phase of the source. Their calculations indicate winds being

launched from very small disk radius which remains unchanged during this phase. Our variable  $R_L$  model allows the launching of wind from as close as the innermost disk region for high  $\Gamma$  cases. The time evolution of the accretion rate from our simulation does not indicate any distinct spike or sharp flare, which leads us to conclude that the system does not produce outbursts. Higginbottom et al. (2017) used their photoionization modelling of the SEDs to argue that thermally driven winds may hold the key to explaining the state changes in such systems. On the other hand, Neilsen (2013) goes on to demonstrate how heavy outflows not only quench the disk, thus affecting the formation of jets and causing state transition, but also influence the further production of winds. Disk variability and the state changes could also be caused or affected by instabilities of the disk itself. For instance, Janiuk et al. (2002) studies the effect of radiation instabilities leading to limit-cycle behaviour and modulations in accretion rates. As opposed to our model, this radiation-driven instability may result in sharp spikes indicating a high outflow from the system.

There are a number of studies related to fast outflows with high mass loss rates leading to state transitions and subsequent detection of jets in the system (Neilsen & Lee, 2009; King et al., 2013; Gatuzz et al., 2019). A similar situation has been discussed in Casares et al. (2019), where a particular case of V404 Cyg indicates the presence of massive outflows, almost 2 orders of magnitude higher than central mass accretion rate  $\dot{M}_a$ . They speculated that these outflows are produced by radiation-driven winds coupled with classical thermal winds. This work stands out as providing direct observational evidence of powerful outflows leading to a quenching of accretion. The optical  $H_\alpha$  line profile clearly indicates disk contraction following the massive outflow phase, consistent with what we would expect happens when irradiation is reduced. Our analysis of the  $\Sigma$  radial profile showed that  $\Sigma$  approaching 0 is responsible for saturating the oscillations.

Recently, Tomaru et al. (2019) showed that the detection of a blue-shifted line from a black hole binary source H1743-322 strongly suggests a thermal-radiative disk wind. Their work indicates a disappearing wind in the hard state which could be attributed to the shadowing of outer disk region by the inner corona. They also went on to state that the absorption features in other black hole sources such as GRS 1915+105 and GRO J1655-40 are most likely due to thermal-radiative winds as opposed to previously speculated magnetic effects. Another recent paper Dubus et al. (2019) studies the effect of thermal-viscous instability on the light curves and stability diagrams associated with black hole binary systems. Additionally, they consider a fraction of the X-ray irradiation to be scattered by the wind and partially impinge on the outer disk regions. This has a stabilizing effect and can explain the shortened outbursts but cannot explain the rapid decay of outbursts. They studied a particular BHXB, GRO J1655-

40, for which their model was able to reproduce the observed features of the light curve. They speculate that magnetic fields would need to be considered for a more promising explanation for the outbursts.

These studies indicate several possible aspects of our simplistic approach towards the study of wind-accretion coupling. The criteria for instability derived by S86 is often invoked when discussing consequences of observed or model disk winds (e.g., Luketic et al., 2010). The main conclusion of our work is that upon satisfying this criteria, a disk wind might not be responsible for large scale variations in luminosity because instability saturates at a relatively low level in terms of  $\dot{M}_a$ . However, it could result in a harder-to-detect significant reduction of  $\Sigma$  at large radii.

<b>p=0.5</b>					
$\Gamma$	$C'_{sd}$	$C'_d$	$C'_{crit}$	$C'_g$	$C'_{sg}$
0.001	-	3.5 $\rightarrow$ 4.7*	4.71	4.715 $\rightarrow$ 4.75	4.8
0.01	-	4 $\rightarrow$ 4.71	4.72	4.8 $\rightarrow$ 5	-
0.05	-	4.7 $\rightarrow$ 4.75	4.772	4.8 $\rightarrow$ 5	-
0.1	-	5 $\rightarrow$ 5.05	5.067	5.1 $\rightarrow$ 5.2	-
0.2	5.2 $\rightarrow$ 5.5	5.8 $\rightarrow$ 6	6.2 $\rightarrow$ 12	-	-
0.3	-	4 $\rightarrow$ 5.45	5.48 $\rightarrow$ 6.2	6.5 $\rightarrow$ 9	10 $\rightarrow$ 15
0.4	4 $\rightarrow$ 4.417	-	4.418	-	4.419 $\rightarrow$ 5
0.5	3.4 $\rightarrow$ 3.6	-**	3.63	-	3.7 $\rightarrow$ 4
<b>p=1</b>					
$\Gamma$	$C'_{sd}$	$C'_d$	$C'_{crit}$	$C'_g$	$C'_{sg}$
0.001	-	11.4	11.6	-	11.65
0.01	-	11.6	11.65	11.7	-
0.05	-	11.8	11.87 $\rightarrow$ 11.9	11.95	-
0.1	-	12.6	12.65	12.7	-
0.2	-	16.5	16.55	16.6	-
0.3	18	-	20 $\rightarrow$ 32	-	45
0.4	15	-	15.93	-	20 $\rightarrow$ 25
0.5	-	11.8 $\rightarrow$ 11.88	11.89	-	11.9 $\rightarrow$ 11.95
<b>p=2</b>					
$\Gamma$	$C'_{sd}$	$C'_d$	$C'_{crit}$	$C'_g$	$C'_{sg}$
0.001	-	39.4	35 $\rightarrow$ 39.3	39.5 $\rightarrow$ 40	50
0.01	-	11 $\rightarrow$ 39.5	39.7	40	-
0.05	-	39.7 $\rightarrow$ 41	41.3	41.5 $\rightarrow$ 42	-
0.1	-	42 $\rightarrow$ 43.5	43.7	44	-
0.2	-	43 $\rightarrow$ 55	60.35	62 $\rightarrow$ 65	-
0.3	-	60 $\rightarrow$ 100	107.8	110 $\rightarrow$ 120	-
0.4	-	110	130 $\rightarrow$ 300	500	-
0.5	78	80 $\rightarrow$ 83	83.7	85	100

\*The  $\rightarrow$  denotes the range of tested values that fall under a certain category. The limits of the range are not absolute but give a more or less general idea of the behaviour within those  $C'$  values.

\*\* Empty cells denote parameter combination for which we do not find the outcome in question. This does not rule out the possibility of such a case or of any other new cases.  $C'_{crit}$  is the only value that was important for our analysis and the parameter survey was focused on finding the condition for stable (or critical) oscillations.

Table 2.2: Summary of parameter survey.  $C'_d, C'_{crit}, C'_g$  hold the same meaning as described in the Table 2.1. The two new types of outcome,  $C'_{sd}$  and  $C'_{sg}$ , denote oscillations that decay/grow for a few time scales before stabilizing and oscillating with a constant amplitude. In Fig. 2.5, we use the corresponding  $C'_{crit}$  to plot the wind efficiency  $\eta_{w,crit}$ .

## Chapter 3

### Synthetic Absorption Line Profiles of Thermally-Driven Winds in AGNs

In this chapter, the results from Ganguly et al. (2021) are discussed. The outline for this chapter is as follows: We provide a background for the theory of thermally-driven outflows and thermal instability, that can lead to the formation of clumps in steady wind solutions in § 3.1 and § 3.2, respectively. We then discuss the setup of the photoionization calculation code XSTAR in § 3.3, followed by the setup of the simulations in the MHD code ATHENA++ in § 3.4. We finally present and discuss the synthetically generated absorption line profiles of the outflow models in the remainder of the chapter.

#### 3.1 Thermally-Driven Winds

We can consider a steady, spherically symmetric flow of a fully ionized pure hydrogen plasma in a gravitational field. Although this is a highly idealized situation, it gives us useful insight into the dynamics of thermal winds. For a steady one-dimensional wind flow, the mass continuity, momentum and energy equations, read

$$\frac{1}{r^2} \frac{d}{dr} (r^2 \rho v) = 0 \quad (3.1)$$

$$\rho v \frac{dv}{dr} = - \left( \frac{dp}{dr} \right) - \frac{GM}{r^2} \quad (3.2)$$

$$\frac{1}{r^2} \frac{d}{dr} \left[ r^2 \rho v \left( \frac{1}{2} v^2 + h \right) \right] = - \rho v \left( \frac{gM}{r^2} \right) + \frac{1}{r^2} \frac{1}{r^2} \left( r^2 K \frac{dT}{dr} \right) \quad (3.3)$$

respectively, where  $h = e + (p/\rho) = 5kT/m_H$  is the specific enthalpy of the plasma. Integrating the continuity equation, we get

$$4\pi r^2 n m_H v = \dot{M} \equiv m_H \mathcal{F} \quad (3.4)$$

where  $\mathcal{F}$  is the particle flux. Integrating the energy equation gives

$$\dot{M} \left[ \frac{1}{2} v^2 + h - \left( \frac{GM}{r} \right) \right] - 4\pi r^2 K \left( \frac{dT}{dr} \right) = \mathcal{E} \quad (3.5)$$

where  $\mathcal{E}$  is the total energy flux. Here, we have also assumed for a fully ionized hydrogen plasma, the electron heat flux is  $\mathbf{q} = -K\nabla T$ , where the thermal conductivity is given by  $K = K_0 T^{5/2}$  with

$K_0 \approx 8 \times 10^{-7} \text{ ergs cm}^{-1} \text{ s}^{-1} \text{ K}^{-7/2}$ . Using the first-order differential equations (3.3) and (3.5), we can determine the structure of the thermal wind. For the determination of a unique solution, we need to specify proper boundary conditions, behaviour of the solution or choices of free parameters.

### 3.2 Field's Criterion for Thermal Instability

The Field's criterion for thermal instability (Field, 1965) can be applied to all optically thin gases in which thermal balance between heating and cooling leads to an equilibrium relation between density  $\rho$  and temperature  $T$  of the form

$$\mathcal{L}(\rho, T) = 0 \quad (3.6)$$

In equation (3.6),  $\mathcal{L}$  is the net loss of heat per unit mass of the gas (shown in fig. 3.1). The region above the curve corresponds to  $\mathcal{L} > 0$  and cooling exceeds heating if the temperature exceeds the equilibrium temperature, while conversely, below the curve  $\mathcal{L} < 0$ , and heating exceeds cooling there. If we have a static, homogeneous gas in thermal equilibrium at some  $\rho$  and  $T$  and consider a small blob embedded in this medium such that it is perturbed away from the equilibrium curve along  $P \propto \rho T = \text{constant}$ . At the point F (in fig. 3.1), if we displace the blob to lower  $T$  and higher  $\rho$  along  $P = \text{constant}$ , then the blob enters the region where  $\mathcal{L} < 0$ . Thus, the blob must heat up and re-expand back to the point F. Conversely, if the blob is perturbed upward, it will cool down to the point F. Hence, the gas placed near the plateau region F is thermally stable. We can conclude the same for the plateau region H.

If the blob however, existed at G and on displacement towards lower  $T$  and higher  $\rho$ , entered the region  $\mathcal{L} > 0$ , then it would get cooler and cooler while maintaining pressure equilibrium with its surroundings, and make a phase transition to become an H-type gas. Conversely, when displaced to higher  $T$  and lower  $\rho$ , on entering  $\mathcal{L} < 0$ , the gas will keep heating until it reaches F. Hence, a gas artificially placed at thermally unstable phase G, would spontaneously separate into two phases of warm rarefied gas and cold dense gas, in pressure equilibrium with one another. This forms the basis of the two-phase model of the ISM (Goldsmith et al., 1969), and the Field's criterion for thermal instability is given by

$$\left( \frac{\partial \mathcal{L}}{\partial T} \right)_P < 0 \quad (3.7)$$

The growth rate of the instability under such a criterion is given by  $-c_P^{-1}(\partial \mathcal{L} / \partial T)_P$ , which yields an estimate of the cooling time of the medium.



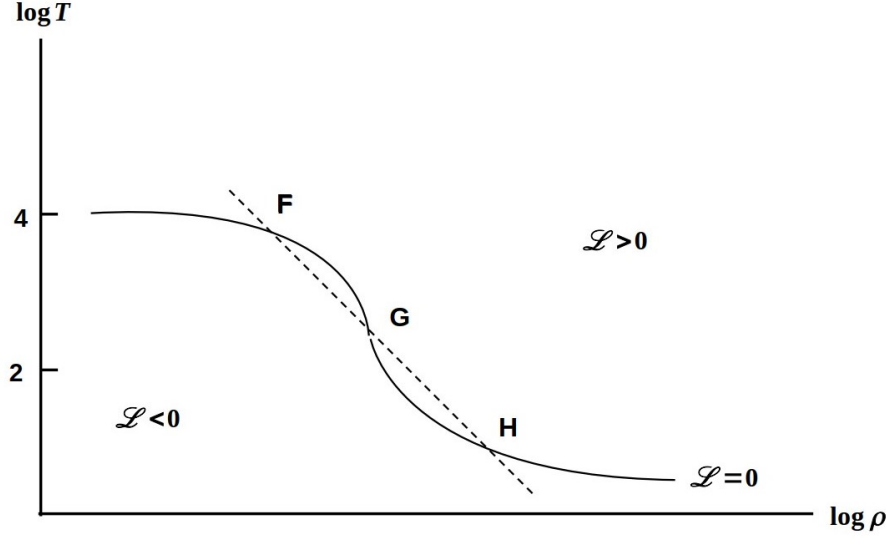


Figure 3.1: Thermal equilibrium curve (solid curve) relevant to the two-phase model of the ISM. The dashed line shows a fiducial isobar  $P \propto \rho T = \text{constant}$ , which shows three possible phases in pressure equilibrium with one another. The phases F and H are thermally stable, while phase G is thermally unstable. *Image credits: Shu (1992).*

### 3.3 Photoionization Code - XSTAR

XSTAR is a command-driven computer program to compute physical conditions and emission spectra of a photoionized gas. Simply put, we can consider a spherical gas shell surrounding a central source of ionizing radiation that absorbs some of this radiation and then re-radiates it in other portions of the spectrum. XSTAR helps calculate the effects on this gas and obtain the re-radiated emission spectra. It also permits consideration of effects due to other sources/sinks of heat such as mechanical compression or expansion, cosmic ray scattering, etc.

Some of the useful outputs produced by XSTAR include the abundance file that contains ion abundance rates and the heating and cooling rates, along with Compton and total heating rates and bremsstrahlung, Compton and total cooling rates (in  $\text{ergs cm}^{-3} \text{s}^{-1}$ ). The log files also contain input parameters such as, log of temperature, radius, fractional distance from illuminated cloud face  $\Delta R/R$ , column density, ionization parameter, electron fraction, proton number density, temperature, fractional heating-cooling rates, continuum optical depth at the Lyman continuum in the transmitted and reflected directions, and the number of iterations required to reach thermal equilibrium.

It is assumed that the spherical shell of gas is irradiated by a point source of continuum radiation at the center, which means that it is implicitly assumed that there is spherical symmetry and that the incident radiation is radially beamed. All physical processes affecting the state of the gas are assumed

to be in steady state. The transfer of radiation is calculated by assuming that diffuse radiation emitted at each radius is directed radially outward or inward. In treating the transfer of photons, a complete redistribution in scattering is assumed, which assumes that the transfer of line photons occurs in a spatial region very close to the point where the photons are emitted. After escaping from the local regions, the line photons are assumed to be subjected to absorption by continuum processes which are treated using the same 2-stream transfer equation as for the continuum. We now present a brief description of the photoionization modelling of a typical plasma (as described in Kallman et al., 2010) and then proceed to the methods applied to carry out photoionization calculations of our hydrodynamic outflow simulations (along the line of work presented in Dyda et al., 2017).

### 3.3.1 Photoionized Plasma Modelling

The gas is typically assumed to be in a steady balance between ionization and recombination and between heating and cooling. If the gas is optically thin, the ionization parameter can be defined in terms of the ratio of the incident ionizing flux to the gas density or pressure. Several expressions of this parameter exists, such as the one presented in Tarter et al. (1969) with  $\xi = 4\pi F/n$ , where  $F$  is the incident energy flux integrated between 1 and 1000 Ry, and  $n$  is the gas number density. For an isobaric gas, it is preferable to use the parameter  $\Xi = \xi/T$  or  $\Xi = \xi/(kTc)$ , as presented in Krolik et al. (1981). The modelling of the plasma is incomplete without radiation transfer calculations which depends on the geometry of the gas and the source of illuminating radiation. The calculation of transfer of ionizing continuum into the photoionized gas and its subsequent transfer out of the gas as a cooling or reprocessed radiation can be quite complex. Recent sophisticated methods such as accelerated lambda iteration method in the Titan code (Chevallier et al., 2006; Róžańska et al., 2006) and Monte Carlo methods (Sim et al., 2008, 2010) to treat transfer in AGN BAL and WA flows produce accurate results, although they are limited to very specialized cases.

The next important step in photoionization modelling of the plasma is to incorporate a comprehensive atomic data. This includes consistent treatment of various ionization/excitation processes, both radiative and collisional, and their inverses, including inner shell processes, for all of the ions of the most abundant elements. A significant amount of work has been done to calculate and measure atomic energy levels, cross sections and transition probabilities for the purposes of astrophysical X-ray photoionization modeling.

## Thermal Instability

The physical origin of thermal instability in the gas due to the properties of the cooling function which allows for two stable and one unstable solutions to exist in pressure equilibrium (discussed in § 3.2), lies in the fact that the net cooling function has a strong temperature dependence in some regions and a weak temperature dependence in others. The existence of thermal instability depends on the validity of the assumption of thermal and ionization equilibrium. Thermal equilibrium requires that the timescale for heating and cooling, the thermal timescale, be less than other relevant timescales, such as gas flow timescales. The net cooling rate per nucleus in a photoionized gas can be written as

$$L_{\text{net}} = \Lambda - H \quad (3.8)$$

where the heating rate  $H = H_X + H_C$  includes the photoelectric and Compton heating rates, respectively, as

$$H_C \simeq n \xi \sigma_C \frac{\langle \varepsilon \rangle - 4kT}{m_e c^2} \quad (3.9)$$

where  $T$  is the electron kinetic temperature,  $\langle \varepsilon \rangle$  is the mean photon energy,  $\sigma_C$  is the Compton cross section and  $n$  is the gas number density. For example, the photoelectric heating rate and the net cooling rate are given due to Blondin (1994) as:

$$H_X \simeq 1.5 \times 10^{-21} n_{\text{cm}^3}^2 \xi^{1/4} T_K^{1/2} \left( 1 - \frac{T}{T_X} \right) \text{ erg s}^{-1} \quad (3.10)$$

$$\Lambda \simeq 3.3 \times 10^{-27} T_K^{1/2} + 1.7 \times 10^{-18} \xi^{-1} T_K^{1/2} e^{-\frac{1.3 \times 10^5 \text{K}}{T_K}} \text{ erg cm}^3 \text{ s}^{-1} \quad (3.11)$$

The first term in  $\Lambda$  is due to bremsstrahlung and dominates in the temperature range  $T_X < T < T_C$ , and at constant pressure,  $n\Lambda \propto T^{-1/2}$ , in this range where the gas is thermally unstable according to Field's criteria:  $dL_{\text{net}}/dT < 0$ .

### 3.3.2 Photoionization Calculation Setup

The setup of our photoionization calculations is similar to that presented in Dyda et al. (2017). Here, we discuss some of their important assumptions applicable to our work, which will be later discussed in detail in § 3.5.1. As in Dyda et al. (2017) and later in D20, we have assumed a particular AGN SED flux that is incident on a box containing known species of gas. Using the known SED, XSTAR can calculate the heating/cooling rates as discussed above, as a function of temperature and ionization

parameter. The mean photon energy corresponding to an X-ray temperature is defined as  $\langle h\nu \rangle = kT_X$ . The heating/cooling in the gas is assumed to be due to Compton, X-ray, bremsstrahlung and line processes. We thus, allow the composition of the gas, atomic transitions and SED of the source to be model-dependent parameters.

### 3.4 Models

Using the magnetohydrodynamics code ATHENA++ (Stone et al., 2020), D20 solved the equations of non-adiabatic gas dynamics with a radiation force due to electron scattering for the unobscured AGN SED of NGC 5548 (see Mehdipour et al., 2015). The line force in these warm/hot winds can exceed gravity but it is much weaker than the gas pressure force (Dannen et al., 2019), and has therefore been ignored in D20 for simplicity. They explored a parameter space comprised of the three dimensionless parameters governing thermal wind solutions: (1) Eddington fraction,  $\Gamma$  ( $=L/L_{\text{Edd}}$  for a system with luminosity  $L$ ), which sets the radiation force per unit volume due to electron scattering as  $F_{\text{rad}} = GM_{\text{BH}}\rho\Gamma/r^2$  ( $M_{\text{BH}}$  is the black hole mass and  $\rho$  the gas density at radius  $r$ ), (2) the pressure ionization parameter at the base of the wind,  $r_0$ ,

$$\Xi_0 = \left. \frac{p_{\text{rad}}}{p} \right|_{r=r_0} = \frac{\xi_0}{4\pi ck_B T_0}, \quad (3.12)$$

where  $p_{\text{rad}} = F_X/c = f_X\Gamma L_{\text{Edd}}/(4\pi r^2 c)$  is the radiation pressure,  $f_X \equiv L_X/L$  is the ionizing portion of the SED ( $f_X = 0.36$  for the NGC 5548 SED used by D20), and  $\xi_0 = L_X/(n_0 r_0^2)$  is the density ionization parameter (with  $n_0 = \rho_0/\bar{m}$ ,  $\bar{m}$  being the mean molecular mass), and (3) the hydrodynamic escape parameter evaluated at  $r_0$ ,  $\text{HEP}_0$ . This parameter is defined as the ratio of effective gravitational potential and thermal energy at  $r_0$ ,

$$\text{HEP}_0 \equiv \frac{GM_{\text{BH}}(1-\Gamma)}{r_0 c_{s,0}^2}, \quad (3.13)$$

where  $c_{s,0} = \sqrt{\gamma k T_0/\bar{m}}$  is the adiabatic sound speed of the gas with the temperature,  $T = T_0$ , and  $\gamma$  is adiabatic index assumed to be 5/3.

To specify the lower boundary conditions of the hydrodynamical simulations (i.e.,  $T_0$ ,  $r_0$ , and  $\rho_0$ ), D20 took the following five steps: (i) selected which SED to use along with its associated ‘S-curve’ and  $f_X$ , (ii) chose values of  $M_{\text{BH}}$ ,  $\Gamma$ , and  $\xi_0$ , (iii) computed  $T_0$  for the value of  $\xi_0$  and assuming that the gas is in thermal equilibrium, i.e.,  $T_0 = T_{\text{gas}} = T_{\text{eq}}(\xi_0)$ , (iv) used  $T_0$  to compute  $c_{s,0}$  and then used

Model	HEP <sub>0</sub>	$r_0$ [10 <sup>18</sup> cm]	$\rho_0$ [10 <sup>-18</sup> g cm <sup>-3</sup> ]	$v$ [km s <sup>-1</sup> ]	$\dot{M}$ [10 <sup>24</sup> g s <sup>-1</sup> ]	$r_{\text{out}}$ [10 <sup>18</sup> cm]	$N_H$ [10 <sup>23</sup> cm <sup>-2</sup> ]
A21	14.7	0.91	3.28	659.3	1.1	9.14	1.22
B	11.9	1.13	2.15	346.0	3.4	11.28	1.47
C	9.1	1.48	1.25	248.0	6.1	14.76	1.35

Table 3.1: Model parameters and some gross properties of steady wind models A21, B and C. These models share the following basic parameters:  $\Gamma = 0.3$ ,  $\Xi_0 = 3.12$  ( $\xi_0 = 5.0$  erg cm s<sup>-1</sup>) and  $M_{\text{BH}} = 10^6 M_\odot$ . D20 found that models B and C are unsteady. However, Waters et al. (2021) refined the numerical methods and found that these two models can eventually settle down to an unstable yet steady state. Once these solutions are perturbed they become clumpy in agreement with D20’s findings. The second, third, and fourth columns list the hydrodynamic escape parameter HEP<sub>0</sub>, the inner radius  $r_0$ , and the density  $\rho_0$  at  $r_0$ , respectively. The next three columns list the following properties of the solutions: the flow velocity  $v$  and mass loss rate  $\dot{M}$  at the outer most grid point,  $r_{\text{out}}$ , at a late time when the flow has become steady. The last column shows the hydrogen column density  $N_H$  for the outflow.

eq. 3.13 to obtain the value of  $r_0$ , and finally ( $v$ ) computed  $\rho_0$  using the expression for  $\xi_0$ . Keeping the parameters  $M_{\text{BH}}$ ,  $\Gamma$  and  $\xi_0$  fixed, D20 altered only the value of the HEP<sub>0</sub> between the models, which required changing  $r_0$  and  $\rho_0$ . Note that once  $\xi_0$  is fixed,  $\Xi_0$  is fixed as well. In Table 3.1, we summarize the parameters of three simulations and the gross properties of the corresponding outflow solutions.

An extensive exploration of the parameter space led D20 to arrive at a new category of ‘clumpy’ thermal wind models occurring at sufficiently large radius (small HEP<sub>0</sub>), namely, solutions that are unstable to TI. As further shown by Waters et al. (2021), these solutions also reach a steady state and only occur beyond a characteristic ‘unbound’ radius given by

$$R_u = \frac{2\gamma - 1}{\gamma\gamma + 1} \frac{T_C}{T_{c,\text{max}}} R_{\text{IC}} (1 - \Gamma) \approx 140 R_{\text{IC}} (1 - \Gamma), \quad (3.14)$$

where the second expression is evaluated for  $\gamma = 5/3$  and for the thermal equilibrium or ‘S-curve’ corresponding to Mehdipour et al. 2015’s SED. The ratio  $T_C/T_{c,\text{max}} = 4.68 \times 10^2$ , where  $T_C$  is the Compton temperature ( $\sim 10^8$  K),  $T_{c,\text{max}} = T(\Xi_{c,\text{max}})$  ( $\Xi_{c,\text{max}}$  is the critical  $\Xi$  for which the gas enters the lower TI zone), and the Compton radius is  $R_{\text{IC}} = (10^{18}/T_C)(M/M_\odot)$  cm.

In Fig. 3.2, we show this S-curve (solid black line) along with the Balbus contour (black dashed line) that is necessary to analyze TI in a dynamical flow. Specifically, while regions of negative slope on the S-curve are thermally unstable, the Balbus contour maps out the thermally unstable parameter space both on and off the S-curve, as explained in the caption. These two  $T$ - $\xi$  relations are computed from our grid of photoionization models first presented in Dyda et al. (2017). In their calculations, Dyda et al. (2017) used version 2.35 of XSTAR (Kallman & Bautista, 2001) and assumed a constant density

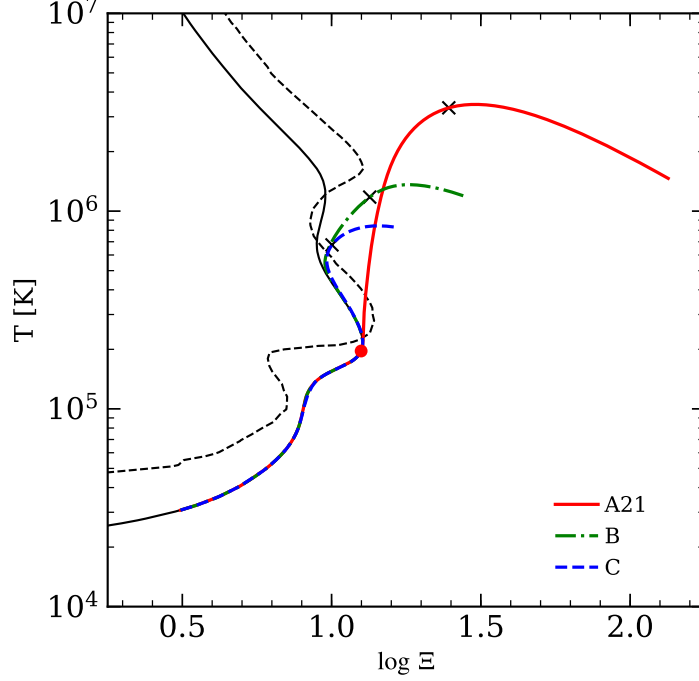


Figure 3.2: Phase diagram ( $T - \Xi$ ): the solid black line represents the thermal equilibrium curve (S-curve) while the black dashed line represents the Balbus contour. All points to the left of the latter are thermally unstable whereas those to the right are thermally stable according to Balbus' criterion for TI (Balbus, 1986). There are two unstable regions encountered while tracing the S-curve starting from low temperatures; we refer to them as the lower and upper TI zones. The figure also shows our three steady wind solutions (solid red, dot-dashed green, and dashed blue line for model A21, B, and C, respectively). We marked the sonic points for each solution with an 'x'. Notice that upon reaching  $\Xi_{c,\max}$  (marked by red dot on the S-curve), Model A21 exhibits runaway heating and quickly exits the lower TI zone. Models B and C instead follow the S-curve within this zone. The decrease in temperature beyond the sonic points in all three cases is due to efficient adiabatic cooling being balanced by radiative heating.

of  $n_{\text{XSTAR}} = 10^8 \text{ cm}^{-3}$  over the parameter space with  $\log \xi$  in the range  $-2 - 8$ , and  $T$  in the range  $5 \times 10^3 - 5 \times 10^8 \text{ K}$ . We note that, unless otherwise stated, we use cgs units throughout the paper, except for the velocity and distance ( $r - r_0$ ), which are in  $\text{km s}^{-1}$  and the inner radius of the computational domain  $r_0$ , respectively.

In this figure, we also present examples of steady state solutions (see the legend for color coding of the curves). The wind solutions chosen are similar to those presented in D20: model A21 is an example of a thermally stable solution<sup>1</sup>, whereas models B and C are examples of thermally unstable solutions. Although all three models reach a time-independent state, they have different properties that signal their stable or unstable character. Namely, after they enter the lower TI zone, the stable solution undergoes rapid heating and leaves the TI zone, evolving under nearly isobaric conditions (moves vertically up on the phase diagram), whereas the unstable solutions continue to follow the S-curve even within the lower

<sup>1</sup>Model A21 is for  $\text{HEP}_0 = 21$  whereas model A in D20 is for  $\text{HEP}_0 = 19$ . As found by Waters et al. (2021)'s improved numerical methods, the transition between stable and unsteady solutions occurs at somewhat higher  $\text{HEP}_0$ .

TI zone (where the slope of the S-curve is negative) over a relatively wide range of  $T$  before they too leave the zone.

In Fig. 3.3 (left), we show radial profiles of the main wind properties of our three steady state solutions. Specifically, we plot the number density  $n$ , temperature  $T$ , flow velocity  $v$ , ionization parameter  $\xi$  and the pressure ionization parameter  $\Xi$ . As discussed above and in D20, model A21 has quite different properties than models B and C. The main reason for this is that model A21 undergoes strong runaway heating (as seen by comparing the temperature profiles), and consequently its velocity/density is higher/lower than that of the other two. In model A21,  $\xi$  is also higher than in models B and C. Therefore we can expect that the models will produce spectral lines with different profiles. In general, we also see that  $\xi$  increases outward, for all the models. One of our goals is to check how this ionization stratification could be traced in the profiles of absorption lines.

### 3.4.1 Clumpy Models

Our steady state model A21 is formally stable to TI despite it passing through the lower TI zone in Fig. 3.2. As discussed by Waters et al. (2021), this happens whenever there is a sharp jump in the entropy profile, which in these solutions will be accompanied by a change in sign of the Bernoulli function. Models B and C, meanwhile, have smooth entropy profiles and the Bernoulli function does not change signs when gas encounters the TI zone. These solutions reach a steady state only when there are no more entropy modes being generated at the base of the flow. Starting from D20's initial conditions, such entropy modes are only produced for a transient period of time.

To examine line profiles for clumpy outflow solutions, we reintroduce entropy modes into models B and C to trigger TI. Specifically, isobaric perturbations, i.e. density perturbations applied at constant pressure (and velocity), are added to the wind base by changing the density boundary condition from  $\rho_{bc} = \rho_0$  to

$$\rho_{bc}(t) = \rho_0 \left[ 1 + \sum_{m=1}^{m=5} A_m \sin\left(\frac{2\pi t}{T_m}\right) \right], \quad (3.15)$$

where  $A_m = A_0/N_{\text{modes}}$  and  $T_m = mT_0$  are the amplitude and period of the driving modes; we set  $A_0 = 0.01$  and  $T_0 = t_{\text{dyn}}/20$  (where  $t_{\text{dyn}} = |r/v|$  is the dynamical timescale). We chose this form of density perturbation, comprising five driving modes ( $N_{\text{modes}} = 5$ ), as it adequately captures the overall complexity of a clumpy wind solution in a controlled way. We will refer to the perturbed versions of Models B and C as Models B-c and C-c.

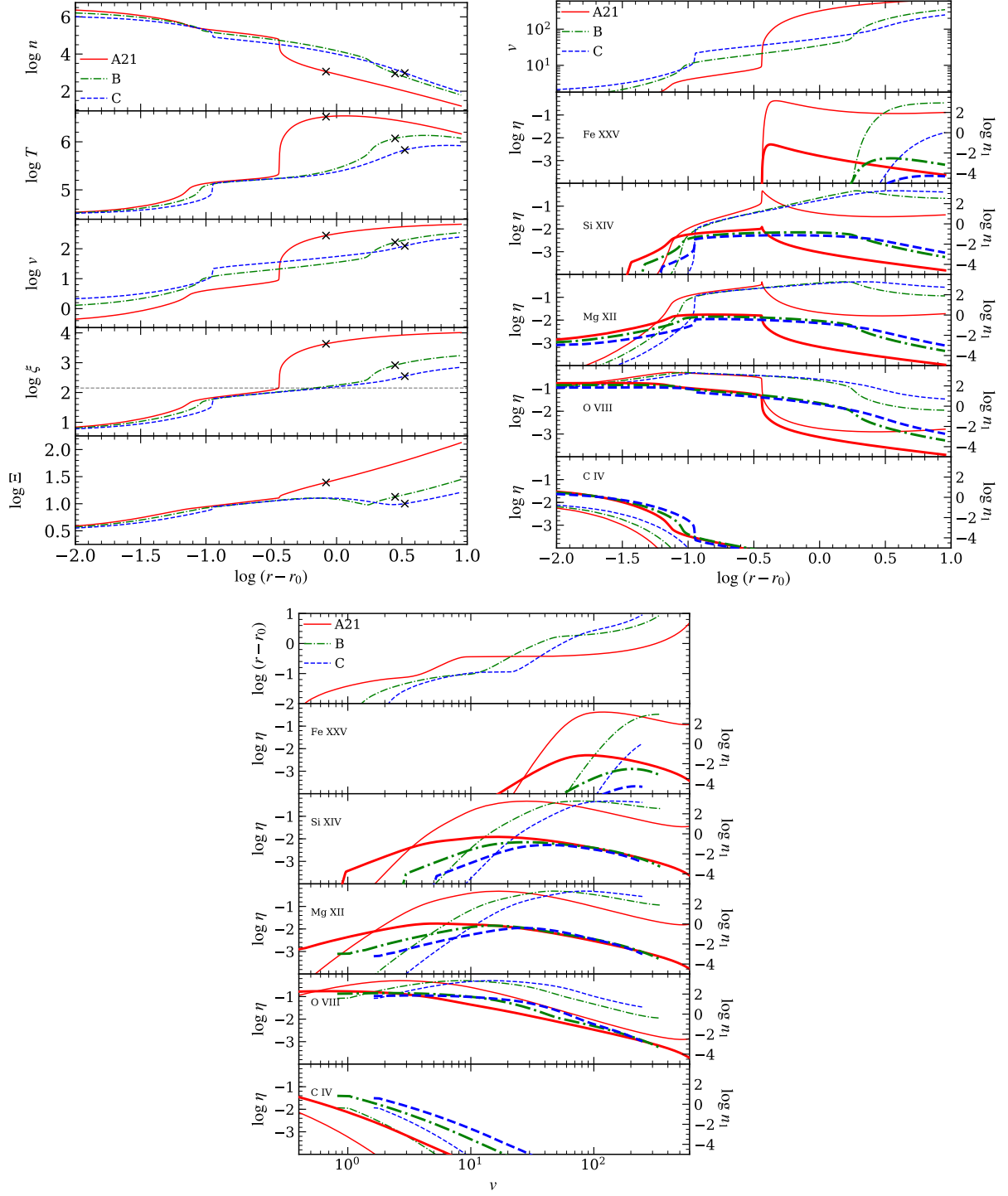


Figure 3.3: *Left*: Radial profiles of logarithm of number density  $n$  ( $\text{cm}^{-3}$ ), temperature  $T$  (K), flow velocity  $v$  ( $\text{km s}^{-1}$ ), ionization parameter  $\xi$  ( $\text{erg cm s}^{-1}$ ) and the dimensionless pressure ionization parameter  $\Xi$ , for the three steady wind models shown in Fig. 3.2. Sonic points are again marked by ‘x’*s*. The horizontal line in the fourth panel marks  $\log(\xi_{\text{c,max}}) = 2.15$ , the entry into the lower TI zone. *Right*: Fractional ionic abundance  $\eta$  (shown on left y-axis, with thinner lines) and the ion ground state level population  $n_1 = n\eta A$  (shown on right y-axis, with thicker lines) vs  $\log(r - r_0)$ , for the same five ions whose line profiles are compared in Fig. 3.6. The topmost panel shows radial velocity profiles (in  $\text{km s}^{-1}$ ) to aid in assessing blueshifts. The legend in this panel applies to both the left and right y-axes. *Bottom*: The same quantities as in the top right subfigure, but plotted against the flow velocity  $v$  (in  $\text{km s}^{-1}$ ) rather than distance. The topmost panel shows the radial distribution of  $v$ .



### 3.5 Ionization Structure and Absorption Diagnostics

As an aid to understanding our line profile calculations, we examine two other wind properties that enter these calculations, namely the fractional ion abundance,  $\eta$ , and the level population of the ion's ground state,  $n_1 = nA\eta$  (where  $A$  is the elemental abundance relative to hydrogen). These quantities provide important information about what to expect and/or how to explain the line profile shapes and the presence of the lines themselves. We extract  $\eta$  and  $n_1$  as a part of post-processing from our grid of photoionization calculations from XSTAR. These quantities are related to the line center absorption coefficient contained in XSTAR output,

$$\begin{aligned} (\kappa_{v_0}\rho)_{\text{XSTAR}} &= \frac{\pi e^2}{m_e c} n_1 f_{12} \phi(v_0), \\ &= \frac{1}{\sqrt{\pi}} \left[ \frac{\pi e^2}{m_e c} \frac{n_{\text{XSTAR}} A \eta}{v_0 (v_{\text{th}}/c)} f_{12} \right], \end{aligned} \quad (3.16)$$

where  $\kappa_{v_0}$  is the line center opacity,  $\rho = \mu m_p n$  is the gas density (mean molecular mass  $\mu = 0.6$  for this work,  $m_p$  is the proton mass),  $f_{12}$  is the oscillator strength of the lower level of the line,  $\phi(v)$  is the profile function to be defined later, and  $v_{\text{th}}(r) = \sqrt{2k_B T(r)/m_i}$  is the mean thermal velocity of an ion with mass  $m_i$ .

To illustrate the details of the ionization structure, in Figs. 3.3 (right) and 3.3 (bottom), we plot  $n_1$  for five ions in order of decreasing IE: Fe XXV, Si XIV, Mg XII, O VIII and C IV (plotted on the right y-axis using thicker lines in the second to sixth panels). We also plot  $\eta$  along the left y-axis (shown by thinner lines). These two figures are complementary to each other since Fig. 3.3 (right) shows  $n_1$  and  $\eta$  as functions of radius while Fig. 3.3 (bottom) shows these quantities as functions of velocity. This mapping to the velocity space is done solely for the purpose of aiding in our analysis and interpretation of line profile results. To this end, the top panels of Fig. 3.3 (right) and Fig. 3.3 (bottom) show respectively the velocity as a function of distance and the distance as a function of velocity.

The ionization stratification is on full display in these figures, e.g., we see that C IV is only abundant at the wind base whereas Fe XXV only at very large radii. Meanwhile, Si XIV and Mg XII are present at intermediate locations and show up roughly where the C IV abundance drops off. Comparing with Fig. 3.2 or Fig. 3.3 (left), we see that C IV disappears at  $r > r(\xi_{\text{c,max}})$ . This is not merely a property of the models but rather the underlying cause explaining why  $\xi_{\text{c,max}}$  identifies a bend in the S-curve: C IV and other mildly ionized elements provide efficient cooling via line emission, and as these ions rapidly deplete as  $\xi$  increases, the photoionization equilibrium temperature must sharply increase as well in

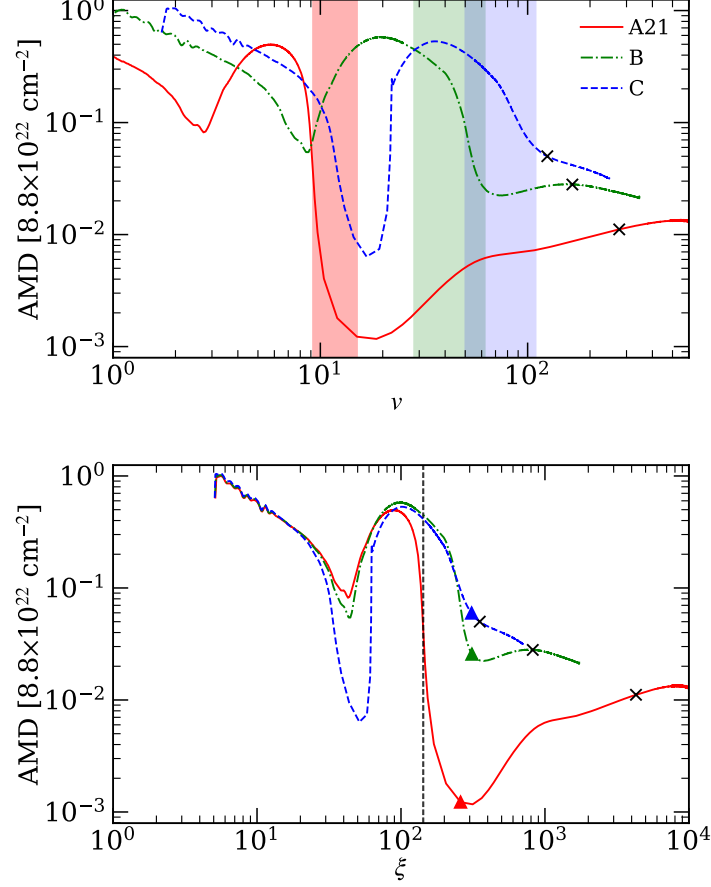


Figure 3.4: Comparison of the AMD for our three steady state wind solutions. The top panel shows the AMD (eq. 3.17) in units of its maximum value for model A21 ( $=8.8 \times 10^{22} \text{ cm}^{-2}$ ) versus  $\xi$ . The vertical black dotted line marks the base of the lower TI zone,  $\xi = \xi_{c,max}$ , while the three triangles mark the points where each model leaves this TI zone. In the bottom panel, these AMDs are mapped onto the flow velocity,  $v$  (in  $\text{km s}^{-1}$ ; the range with  $v < 1 \text{ km s}^{-1}$  is not shown). Sonic points are marked with ‘x’ symbols and the color shadings denote the parameter space of gas occupying the lower TI zone.

order to compensate for this lack of efficient cooling. As we will describe below, this enhanced heating and subsequent gas acceleration results in a drop in the amount of matter (measured by the column density).

Our last diagnostic that can help to develop a feel for the absorption properties of our wind solution is the absorption measure distribution (AMD). It is defined as

$$\text{AMD} = \frac{dN_H}{d(\log \xi)} = n\lambda_\xi, \quad (3.17)$$

where  $N_H$  is the hydrogen column density and  $\lambda_\xi = (d \log \xi / dr)^{-1}$  is the characteristic length scale for variations in  $\xi$ . The AMD has proven to be both an important observable (Holczer et al., 2007; Behar, 2009) and a useful tool for quantifying the absorption properties of hydrodynamical models. We note that for a steady state,  $v \propto \xi$  ( $v \propto 1/nr^2$ , as is  $\xi$ ). Therefore,  $\lambda_\xi = \lambda_v \equiv (d \log v / dr)^{-1}$ .

In Fig. 3.4, we show the AMDs for our three steady models. There are two prominent dips in the AMD: one at the entrance to the TI zone, which is marked by the vertical line in the top panel, and another at even smaller  $\xi$ , corresponding to gas on the cold phase branch of the S-curve. The bottom panel in Fig. 3.4 shows this latter dip occurs for low velocity gas. As pointed out by Dyda et al. (2017), a dip in the AMD can be caused by enhanced heating even in regions that are thermally stable. Referring to Fig. 3.2, notice that the cold branch of the S-curve becomes nearly vertical (for  $\log \Xi \approx 0.9$  and  $T$  just above  $10^5$  K), or equivalently, the S-curve and the Balbus contours approach each other. In this physical regime, the velocity is relatively low but the acceleration is relatively high (e.g., see Fig. 3.3 (left) for the steep gradient in the radial profiles of  $T$ ,  $n$  and  $v$ ). This rapid acceleration leads to the minima in the AMD at  $v \approx 2, 10$ , and  $20 \text{ km s}^{-1}$  in models A21, B, and C, respectively.

A quantitative understanding of the reason for a decrease in the AMD is found by referring to the right hand side of eq. 3.17 and recalling that  $\lambda_\xi = \lambda_v$  (see above). Also note that an enhanced acceleration results in shortening the characteristic length scale  $\lambda_v$ . The region of the enhanced acceleration is relatively small. Therefore,  $\lambda_v$  increases as the slope of the S-curve flattens again, and the AMD recovers to the level from before the drop. Importantly, our analysis above (mentioned while describing top right and bottom subfigures in Figs. 3.3) reveals that such a change in the slope of the S-curve can be driven by a reduction in line cooling: all wind solutions reach this region of enhanced acceleration where the abundance of C IV undergoes a sharp decrease (at  $\log(r - r_0) \approx -1$  in the right bottom panel of Fig. 3.3). In other words, the gas experiences enhanced heating as a result of it losing important coolants.

Farther downstream, the gas becomes even more ionized and, as we already mentioned, it enters the lower TI zone at  $\xi_{c,\max}$ . The corresponding changes in the thermal and dynamical properties of the wind solutions produce a change in the AMD. Namely, the AMD drops by one or even two orders of magnitude (see the shaded color areas in the bottom panel of Fig. 3.4). This is best exemplified by the results for model A21 where the heating is so enhanced that it leads to runaway heating. The drops in the AMD for models B and C are not as large simply because the heating is weaker. Upon exiting the TI zone, the AMD in model C continues to decrease unlike in models A21 and B where we see a mild increase.

Our analysis demonstrates how the flow properties closely depend on the gas dynamics and thermodynamics even if the flow is time independent. The methodology used by D20 to couple photoionization and hydrodynamical calculations provides us with a substantial amount of information. Not only can we extract the opacities necessary to compute absorption line profiles, but we can also examine intermediate quantities to explain the physics behind the properties of the profiles and the relations between different

ionization states.

### 3.5.1 Photoionization Calculations

The photoionization calculations from XSTAR provide us with the quantity in brackets in equation (3.16) above, for  $n = n_{\text{XSTAR}} = 10^8 \text{ cm}^{-3}$ . Due to  $(\kappa_{\nu_0}\rho)_{\text{XSTAR}}$  being insensitive to  $n_{\text{XSTAR}}$  in low density regimes, we can calculate the opacities corresponding to our hydrodynamic density profiles as follows,

$$\kappa_{\nu_0}\rho = (\kappa_{\nu_0}\rho)_{\text{XSTAR}} \times \frac{n}{n_{\text{XSTAR}}}. \quad (3.18)$$

In practice, we generate lookup tables of  $(\kappa_{\nu_0}\rho)_{\text{XSTAR}}$  parameterized by  $\xi$  and  $T$ , using bilinear interpolation to access values for the local hydrodynamic values of  $(\xi, T)$  in our simulations (see Waters et al., 2017).

Our current analysis is an improvement over Waters et al. (2017) on two major fronts: (i) their heating/cooling source term was calculated using analytical fits to earlier photoionization calculations by Blondin (1994), while their opacities were extracted from XSTAR using a similar 10 keV Bremsstrahlung SED. For this work, we extract abundances, opacities, and heating/cooling rates from XSTAR for a realistic AGN SED; (ii) we examine over two dozen lines as opposed to the study of only the O VIII Ly $\alpha$  doublet (O VIII 19) in Waters et al. (2017), which was determined to be the strongest line in their local cloud simulations. In Table 3.3, we list the basic properties of the lines and the corresponding ions selected for analysis.

The frequency-dependent line optical depth is calculated (using the trapezoid rule) as

$$\tau_{\nu} = \int_{r_{\text{in}}}^{r_{\text{out}}} \kappa_{\nu}(r)\rho(r) dr, \quad (3.19)$$

where  $r_{\text{in}}$  and  $r_{\text{out}}$  are the inner and outer radius of the computational domain and

$$\kappa_{\nu}(r) = \kappa_{\nu_0}(r)\phi(\nu)/\phi(\nu_D) \quad (3.20)$$

is the frequency distribution of opacity corresponding to a particular ion. Here  $\phi(\nu)$  is the profile function, taken to be a Gaussian distribution with a thermal line width  $\Delta\nu_0 = \nu_0\nu_{\text{th}}/c$ :

$$\phi(\nu) = \frac{1}{\sqrt{\pi}} \frac{1}{\Delta\nu_0} \exp\left(\frac{-(\nu - \nu_D)^2}{\Delta\nu_0^2}\right). \quad (3.21)$$

Ions	A21	B	C	Ions	A21	B	C
Fe XXVI	$2.42 \times 10^{16}$	$4.71 \times 10^{15}$	$5.20 \times 10^{13}$	Ne VIII	$1.59 \times 10^{18}$	$1.61 \times 10^{18}$	$1.53 \times 10^{18}$
Fe XXV	$1.67 \times 10^{16}$	$1.35 \times 10^{16}$	$3.86 \times 10^{14}$	O VI	$5.93 \times 10^{18}$	$6.05 \times 10^{18}$	$6.20 \times 10^{18}$
Ar XVIII	$2.17 \times 10^{15}$	$5.61 \times 10^{15}$	$3.38 \times 10^{15}$	N V	$2.16 \times 10^{17}$	$2.21 \times 10^{17}$	$2.27 \times 10^{17}$
S XVI	$8.82 \times 10^{15}$	$4.28 \times 10^{16}$	$3.77 \times 10^{16}$	C IV	$8.86 \times 10^{16}$	$9.06 \times 10^{16}$	$9.35 \times 10^{16}$
Si XIV	$6.64 \times 10^{16}$	$2.88 \times 10^{17}$	$2.75 \times 10^{17}$	He II	$1.44 \times 10^{19}$	$1.48 \times 10^{19}$	$1.50 \times 10^{19}$
Mg XII	$2.82 \times 10^{17}$	$6.68 \times 10^{17}$	$6.04 \times 10^{17}$	S IV	$2.70 \times 10^{13}$	$2.77 \times 10^{13}$	$2.86 \times 10^{13}$
Ne X	$2.20 \times 10^{18}$	$3.56 \times 10^{18}$	$2.99 \times 10^{18}$	Si IV	$3.89 \times 10^{12}$	$4.00 \times 10^{12}$	$4.13 \times 10^{12}$
O VIII	$2.01 \times 10^{19}$	$2.34 \times 10^{19}$	$2.01 \times 10^{19}$	Si III	$1.96 \times 10^{11}$	$2.02 \times 10^{11}$	$2.09 \times 10^{11}$
O VII	$3.20 \times 10^{19}$	$3.26 \times 10^{19}$	$3.21 \times 10^{19}$	C II	$1.56 \times 10^{13}$	$1.60 \times 10^{13}$	$1.65 \times 10^{13}$
N VII	$3.43 \times 10^{18}$	$3.67 \times 10^{18}$	$3.37 \times 10^{18}$	Mg II	$1.25 \times 10^7$	$1.29 \times 10^7$	$1.34 \times 10^7$
C VI	$1.28 \times 10^{19}$	$1.33 \times 10^{19}$	$1.29 \times 10^{19}$				

Table 3.2: Ionic column densities ( $\text{cm}^{-2}$ ) in steady models. The ionic column density for each ion in our survey,  $N_{\text{ion}} = \int n_1 dr$ , where  $n_1$  is the level population for the ground state, for the three steady models A21, B and C.

This function peaks at frequency  $\nu_D(r) = \nu_0[1 + v(r)/c]$ , corresponding to the line center Doppler-shifted to the local wind velocity.

The solution of the radiative transfer equation in 1D, for zero emission, can be expressed as the intensity,

$$I_\nu = I_0 e^{-\tau_\nu(r)}, \quad (3.22)$$

where  $r$  is the radial distance from the central source (an X-ray corona near the black hole). We use equations (3.19) - (3.22) to calculate the synthetic absorption line profiles,  $I_\nu$ , for a chosen ion and model run, taking  $I_0 = 1$ .

### 3.6 Results

As one would expect based on the values of the AMD, our models are associated with significant ionic column densities for ions spanning a large range of ionization energy (IE). In Table 3.2, we list the results of our calculations of ionic column density for the steady models. We also plot these ionic column densities and their values corrected for the element abundance, i.e.,  $N_{\text{ion}}/A$ , i.e. the hydrogen column density in the region where the given ion is present, in Fig. 3.5 (see the top and bottom panel respectively). These results show that there can be significant absorption in lines due to ions of the abundant elements, especially if they are mildly to highly ionized (e.g., He II, C VI, O VII, and O VIII). On the other hand, ions with IE less than that of He II are expected to produce weak absorption.

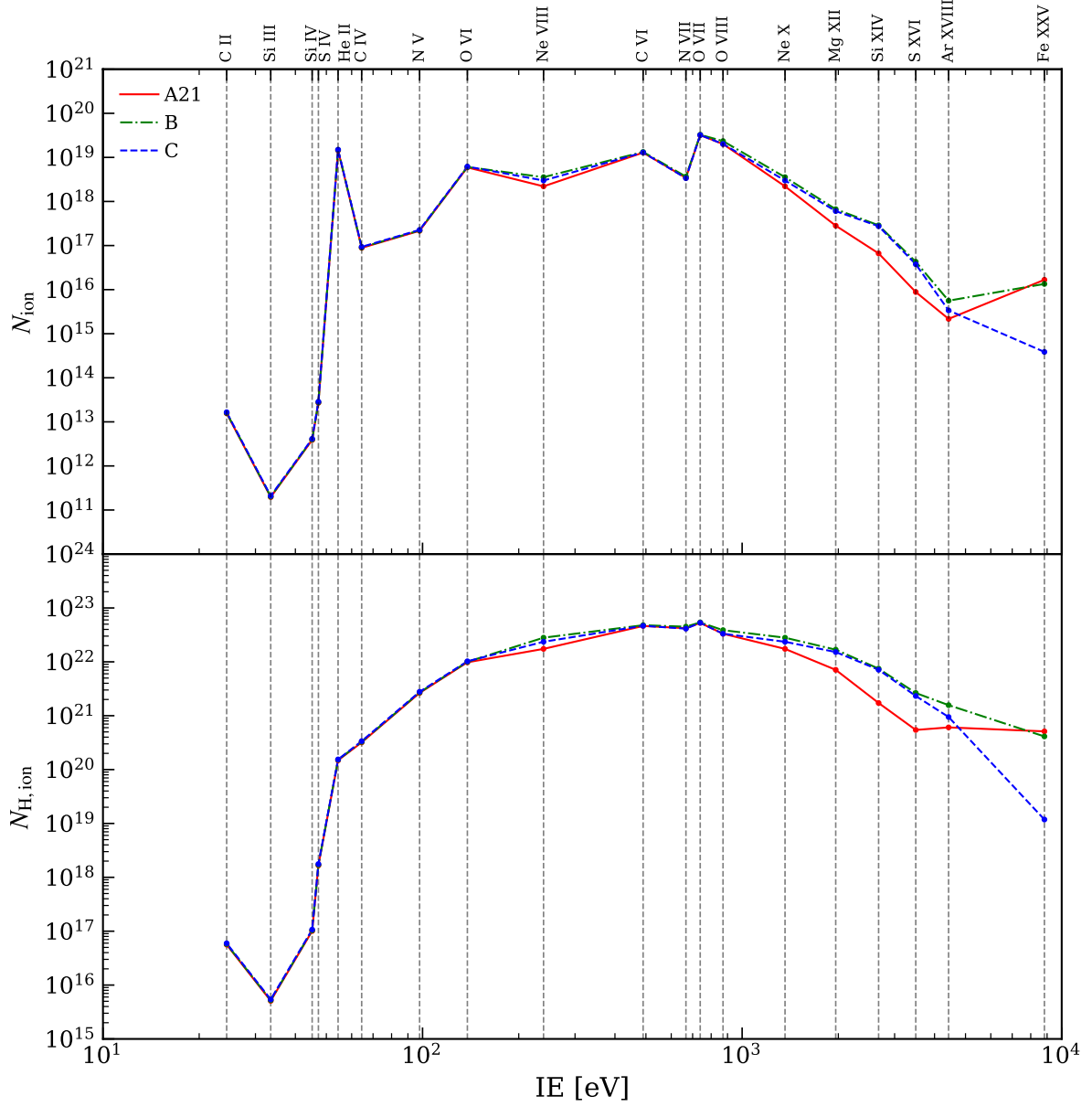


Figure 3.5: Column densities as functions of ionization energy. *Top panel:* the column density of a given ion (the ionic column density,  $N_{\text{ion}}$ ) as a function of IE of that ion (see also Table 3.2). *Bottom panel:* as above but with  $N_{\text{ion}}$  corrected for the element abundance ( $N_{\text{ion}}/A$ ), so it is the hydrogen column density in the region where a given ion is present.

In §3.6.1, we first analyze line profiles computed for steady state solutions. Then in §3.6.2, we analyze those of unsteady versions of our thermally unstable models (B and C).

### 3.6.1 Steady State Wind Solutions

In Fig. 3.6, we highlight the absorption profiles for the same ions that we used to illustrate the ionization stratification in section 3.4 (i.e., Fe XXV, Si XIV, Mg XII, O VIII, and C IV).<sup>2</sup> In Fig. 3.7, we show profiles for our full selection of lines for various ions, including those shown in Fig. 3.6. Note that in both the figures, for the doublet lines, we plot the total profile by adding the profiles due to the red and blue components. In Fig. 3.7, however, we also show the individual profiles due to these components using red and blue dashed lines, respectively. To aid connection between the wind solution and the line profiles, in the bottom panels of these figures, we plot  $\xi$  as a function of  $v$ .

Line profiles in our sample belong to one of four major categories: 1) Gaussian (typical for weak lines, e.g., the S IV line), 2) boxy (lines with a strong broad core, e.g., the C IV line, 3) boxy with an extend blue wing (e.g., Mg XII), and 4) weak extended (e.g., Fe XXV). Below we will focus on the last three categories.

The troughs of the C IV, O VIII 19 and Mg XII show black saturation. The profile of the red component of the UV C IV line is relatively simple. It has a boxy shape and its width is determined by the line saturation. The line has a relatively sharp transition from the very optically thick core to the line wings. However, the profile is not exactly symmetric because even though the line forming region is near the wind base, it still has non-zero bulk velocity (see fig. 3.3, left). Therefore, the blue wing of the line is broader than the red wing due to a Doppler blueshift. The C IV profile is similar for all three wind models because the wind solutions are also similar at the base. The main difference is the line width: it increases from model A21 through B to C and this order is consistent with the order of the velocity at which  $\xi = \xi_{c,max}$  (compare the bottom panel in Fig. 3.6 with the panel immediately above). These subtle differences are in contrast with the other profiles shown in this figure, with different models producing quite different line profiles; these are all X-ray lines with significant opacity above the wind base.

The profiles of the O VIII 19, Mg XII and Si XIV 5 lines are narrower, less blueshifted, and even weaker for model A21 than for models B and C, and this might seem contradictory to the fact that the wind in model A21 is the fastest. However, the lines probe the conditions where the population of their lower levels are the largest, and as we showed in the previous section, the  $n_1$  distribution of

---

<sup>2</sup>The number after the ion name denotes the wavelength (in Å) absorbed by the ion to undergo a particular transition and is only shown for the few lines in our full list given in Table 3.3 that are from the same ion (e.g., Si XIV 5 and Si XIV 6).

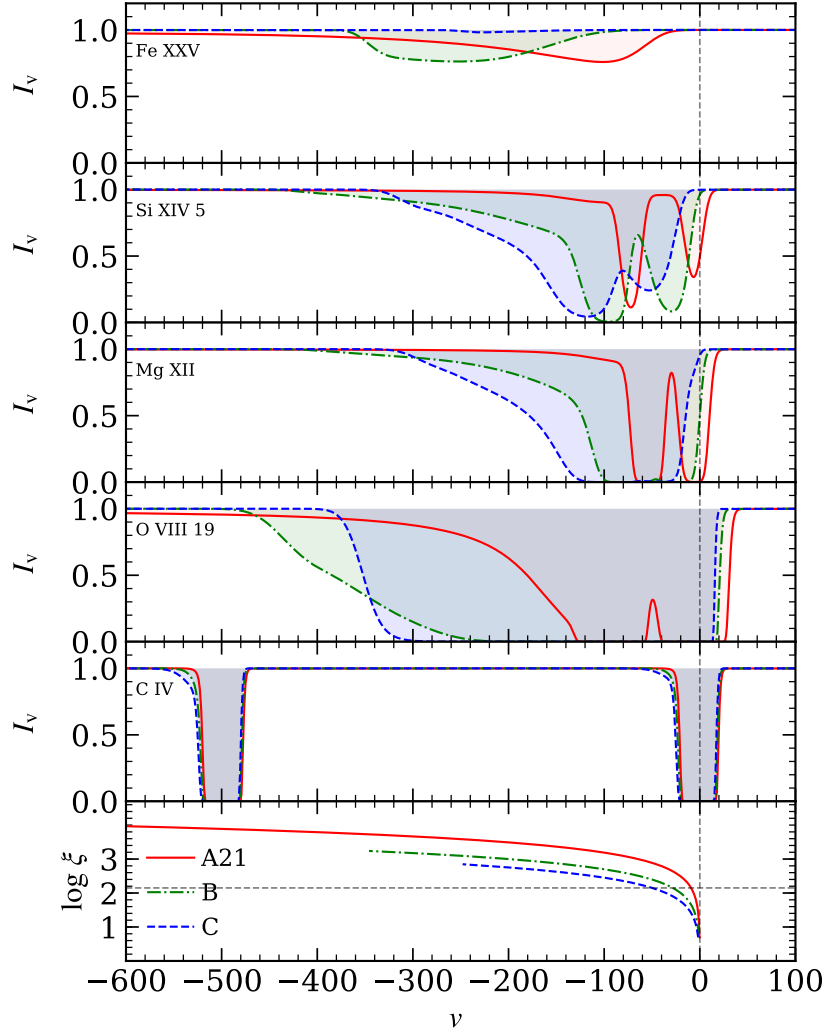


Figure 3.6: Absorption profiles due to lines from five ions (as labeled) together with a plot of  $\xi$  vs.  $\nu$  (bottom panel). Red solid, green dot-dashed, and blue dashed lines denote model A21, B and C, respectively. Absorption troughs are shaded to highlight their depth and shape. Except for Fe XXV, all lines shown here are doublets (see Table 3.3 for details). The C IV doublet components (second from the bottom panel) are separated in all three models whereas the Si XIV 5, Mg XII, and O VIII 19 doublet components are blended. The vertical grey dashed line marks  $\nu = 0$  in all panels. In the lowermost panel, the horizontal dashed line marks  $\log(\xi_{c,\max}) = 2.15$  in order to judge the blueshift at which the flow enters the lower TI zone.



their corresponding ions peaks within a relatively narrow velocity range that does not include the fast part of the wind. That is, ionization stratification may cause the signature for any individual line to be diminished and not reflect on the entire wind solution. In addition, the strong runaway heating in model A21 leads to a drop in the overall flow density that in turn reduces wind absorption, as can be seen in the AMD. Therefore, the absorption in these three lines at large velocities in model A21 is weaker than in the other two models.

The Fe XXV line stands out among the other lines in Fig. 3.6: its blueshifted trough does not extend to zero velocity. This feature is simply caused by lack of the Fe XXV ion at small velocities (see top right and bottom subfigures of Fig. 3.3 for the distributions of the ion abundance).

A quick inspection of Fig. 3.7, where our full sample of line profiles are plotted in order of decreasing IE, reveals that the velocity of the red-edge of the lines increases overall with IE: it is negative for the low energy ions and can be positive for the high energy ions. In addition, the extent of the blue wing of strong lines mostly decreases with decreasing IE. These trends are more clearly evident in Fig. 3.8 that will be discussed below. The notable exception to the second trend is the He II line which is relatively wide. This is due to the fact that the line's strong saturation is related to a relatively very high helium abundance leading to its ground level population being significant over a wide range of radii.

Fig. 3.7 shows that a 'detachment' of the line forming region from the wind base is not unique to the Fe XXV line. This is seen to a lesser degree in the profiles of the Si XIV 5 and 6 lines for model C (and lesser still for model B). Referring yet again to Fig. 3.3 (bottom) to check if there is obvious explanation for this, we see that although models B and C have smaller terminal velocities than model A21, they are actually faster where the Si XIV ion is most abundant.

We also note that absorption in the Mg II line is absent in our models while the C II, Si III, Si IV, S IV lines are weak and symmetric. These low ionization lines form at the wind base and the maximum absorption (of the red component) is at or near zero velocity.

To quantify the extent of the blue wing, we measured the velocity at which  $I_v = 0.99$  for each line. We refer to this as the blue-edge velocity,  $v_B$ , and we plot  $v_B$  as a function of IE in Fig. 3.8. When the line is a blended doublet, we correct  $v_B$  for the doublet split, while for unblended lines we measure  $v_B$  of the red component.

Fig. 3.8 shows that, in general, for low IE lines, the extent of the blue wing is close to  $v_{c,max}$ , the velocity at which  $\xi$  approaches  $\xi_{c,max}$ , while  $v_B$  is close to the maximum wind velocity for high IE lines. As mentioned above, the He II line is an exception because it is a very strongly saturated line. We note that in model A21, not all high IE lines extend to the maximum wind velocity (see e.g., Ne X and Mg

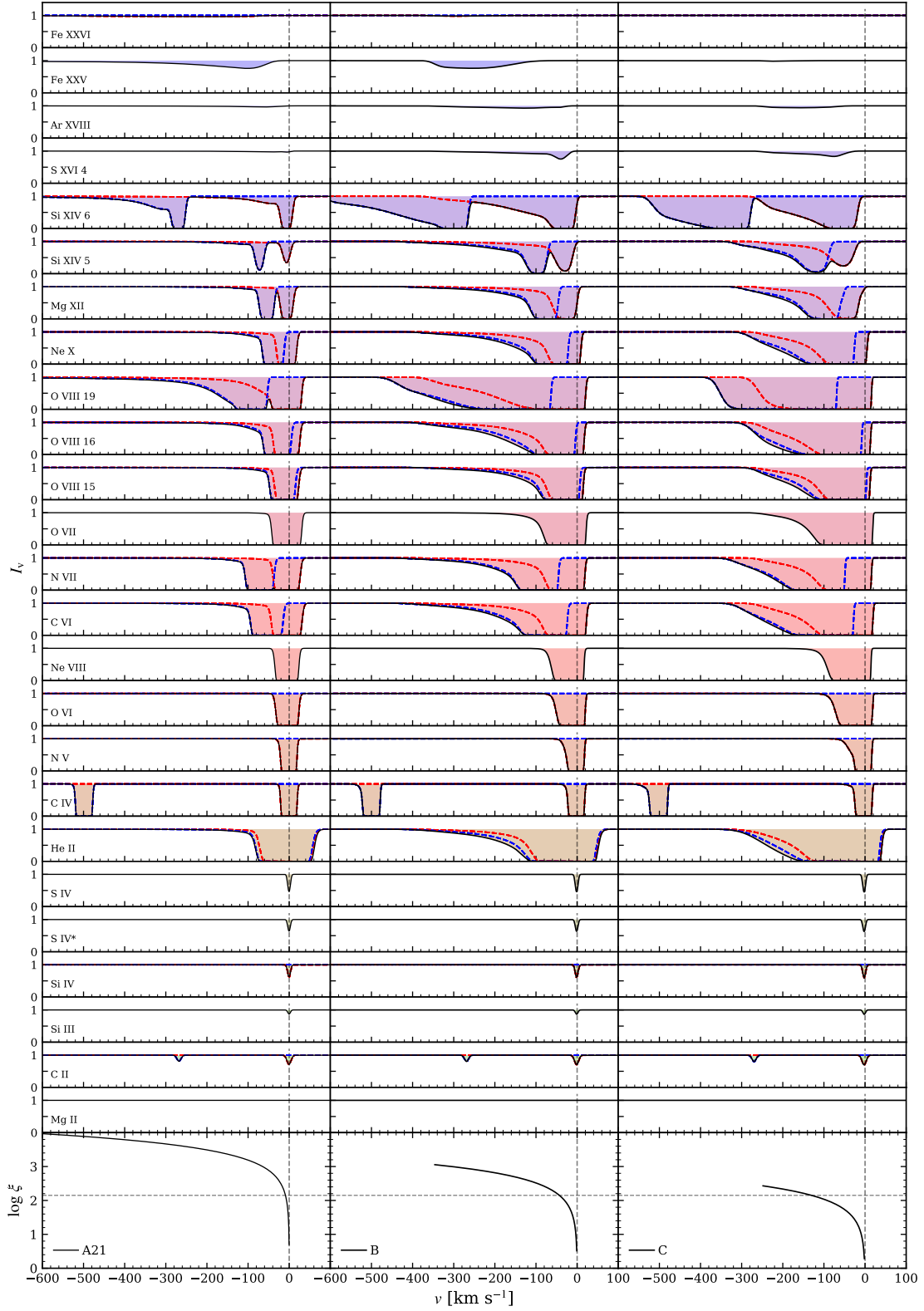


Figure 3.7: Absorption profiles for models A21, B and C (left, middle, and right columns of panels, respectively). See the ion labels at left and Table 3.3 for the line identification. The profiles are shown using solid black lines. For doublet lines, we plot a composite spectrum by adding the red and blue components while accounting for their wavelength separation in velocity space. The individual components have been additionally plotted with red and blue dashed lines. In the bottom panel, we plot the ionization parameter against the radial flow velocity, for reference. The dashed horizontal line indicates the value of  $\xi_{c,max}$ , whereas the black vertical line marks zero velocity. For FITS files of all our line profile calculations, see: <http://www.physics.unlv.edu/astro/clumpywindsims-lps.html>.

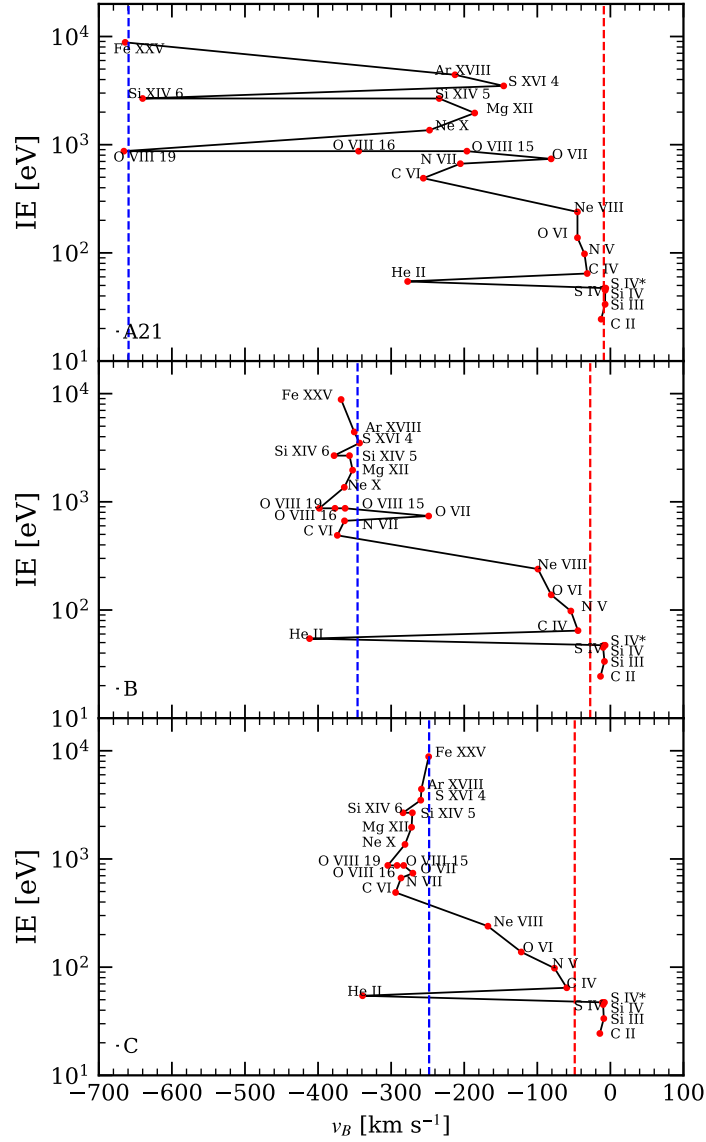


Figure 3.8: The position of the the blue-edge of the absorption trough,  $v_B$  as a function of IE. We formally define  $v_B$  as the velocity where  $I_v = 0.99$ . When the line is a blended doublet we correct  $v_B$  for the doublet split. Here we show results for the steady models. The blue and red dashed lines indicate the maximum flow velocity and the velocity where ionization parameter  $\log \xi = \log \xi_{c,max} = 2.15$ , respectively.

XII) because the opacity of this line is relatively small at large radii for this wind solution.

The three lines of the same ion, i.e. those of O VIII, offer a good illustration of how the opacity affects the line extent. The lines of this ion have very strong and broad cores and extended blue wings. In model A21,  $v_B$  increases with the oscillator strength, which is strongest for O VIII 19 and weakest for O VIII 15. The line absorption extends all the way to the wind maximum velocity only for the O VIII 19 line (see also Fig. 3.7).

Overall, the comparison of the three models shows that  $v_B$  of high IE lines could be a good proxy for the maximum flow velocity for models B and C but for model A21, this is true only for certain high IE lines.

### 3.6.2 Clumpy Wind Solutions

In Fig. 3.9, we over-plot line profiles for Model B-c (in magenta) on those for steady Model B shown previously in Fig. 3.6. Only one new category of line profile needs to be added to our list given in §3.6.1: boxy with an extended *non-monotonic* blue wing. It is clear from this figure that non-monotonic features can be due to either stronger or weaker absorption at different velocities and are present in all lines except those from ions with peak abundance at  $\xi < \xi_{c,\max}$  like C IV. In other words, clumps do not affect the ‘boxy’ profiles characterizing ions formed at the wind base, as clumps are produced further downstream.

Of the remaining profiles, that of Mg XII is perhaps the most intuitive: the clumps in Model B-c can be considered over-densities superimposed on the ‘background’ wind profiles shown in Fig. 3.3 (left). Hence, a deeper absorption trough should occur at the velocity where the clump resides. More distant clumps will thus have both higher velocity and lower density, so this explains the general trend that absorption troughs get less deep at higher velocities in the wing. The width of each trough is essentially  $\max(\Delta v_c, v_{\text{th}})$ , where  $v_{\text{th}}$  is the ion thermal velocity and  $\Delta v_c$  is the range of line of sight velocities internal to the clump. As will be shown below, model C-c results in smooth line profiles because the intercloud spacing is very small. Hence, we can state that a very clumpy wind can appear completely smooth with monotonic wings if it satisfies the condition that the velocity separation of the clumps is smaller than the thermal widths. Note that similar considerations have been used to place constraints on the number of clouds in broad line regions (Arav et al., 1997).

To clearly illustrate the contribution of clumps to line profiles, Fig. 3.9 breaks down different density regions of the outflow in the case of the Mg XII line profile (again for model B-c). The saturated part of the absorption trough is formed at the wind base, although some of the slowest clumps do contribute.

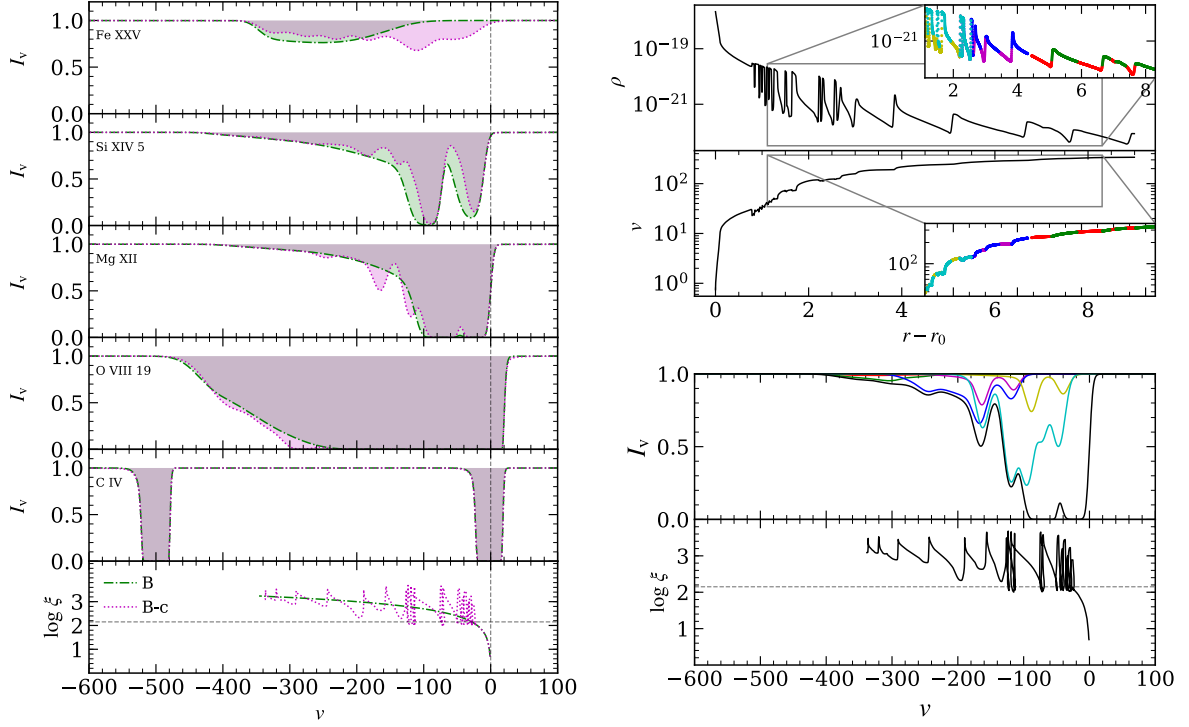


Figure 3.9: *Left*: Line profile comparison for the steady model B (dot-dashed green shaded profile) and the unsteady/clumpy model B-c (dotted magenta shaded profile, refer to eq. 3.15). The lower panel shows  $\log \xi$  vs  $\nu$  for these two cases, for comparison, where horizontal gray dashed line marks  $\log(\xi_{c,\max}) = 2.15$ , while vertical dashed lines mark  $\nu = 0$  in all panels. *Right*: Contributions of different parts of a clumpy outflow (model B-c) to the overall line profile for Mg XII. The colors green, blue and cyan highlight the higher-than-average density regions corresponding to clumps, while the red, magenta and yellow highlight intercloud regions.

This is shown by the cyan colored regions, where absorption due to several high velocity clumps blend together to form part of the line core as well as discernible absorption troughs in the blue wing of the profile. Regions marked in green and blue are responsible for the higher velocity features that together add up to form the extended blue wing of the line. The absorption within the warm, under-dense regions between the clumps is seen to be mostly negligible (see the red, magenta and yellow colors).

In Fig. 3.10, we illustrate how the Mg XII line profile changes due to the evolution of the clumps in model B-c. We plot the profile at three times,  $t_i$  (as explained in figure caption;  $\Delta t = (t_i - t_0) = \{0, 0.54, 1.09\}$  kyr). For reference, we also plot the time-averaged line profile (shown in black). The dips become increasingly blueshifted with time and also less deep as the clumps move outward with a higher velocity and become less dense. In the middle panel, we show the absolute difference between each of the three profiles and the time-averaged profile. This reveals that the largest differences occur at velocities where

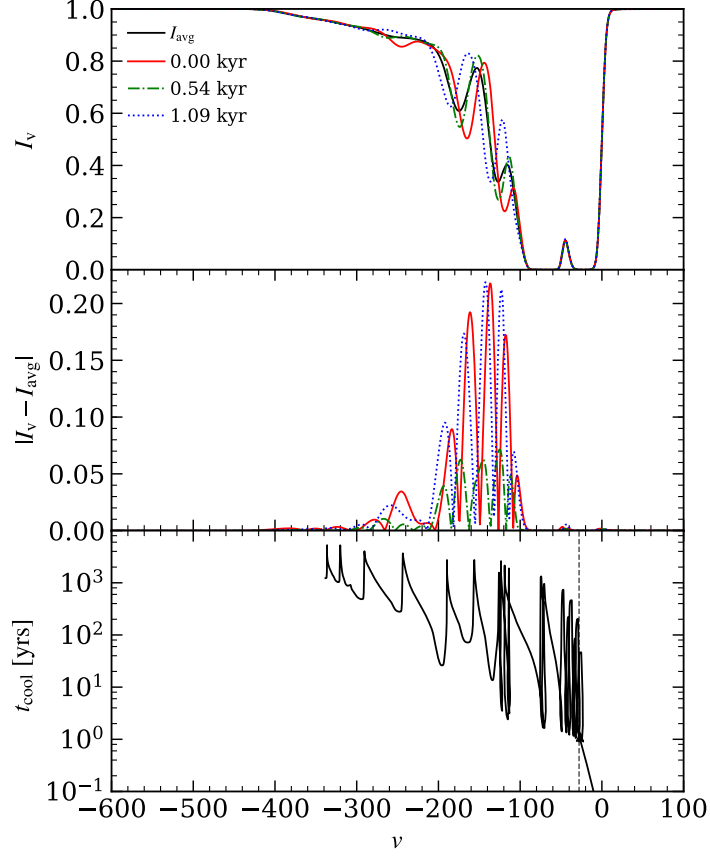


Figure 3.10: Variability of the Mg XII line profile for model B-c. Line profiles at three different states  $t_i$  of the simulation runs are plotted along with the time-averaged line profile. The legend shows the time  $\Delta t = (t_i - t_0)$  (in kyr), the red line denoting the state  $t_0$ . The middle panel shows the difference between the snapshots from the average profile. The bottom panel shows the cooling time,  $t_{\text{cool}}$ ; a vertical line marks the velocity for which  $\log \xi_{c,\text{max}} = 2.15$ , showing that cooling times exceed 1 year in the clumps. Any time-dependence must therefore occur on longer timescales. An animation of the time evolution of line profiles for B-c and C-c, can be found here: <http://www.physics.unlv.edu/astro/clumpywindsims-lps.html>.

the line just starts to de-saturate. The bottom panel shows the cooling time,

$$t_{\text{cool}} = 6.6 \frac{T_5}{n_4 C_{23}} \text{ yrs} \quad (3.23)$$

where  $T_5 = T/10^5$  K,  $n_4 = n/10^4 \text{ cm}^{-3}$  and  $C_{23} = C/10^{23}$  is the cooling rate in units of  $\text{erg cm}^3 \text{ s}^{-1}$ . The vertical dashed line marks the velocity at which  $\log \xi > \log \xi_{c,\text{max}} = 2.15$ . Above this velocity, the cooling time is of the order of years, which indicates that the flow cannot respond to minor flux variability on timescales less than  $\sim 1$  year. Note from §3.4.1 that we chose the time period of perturbations to be a small fraction of the dynamical time scale, but still large enough to ensure that the gas can respond.

In Fig. 3.11, we again show a plot of IE versus  $v_B$ , this time showing models B-c and C-c over-plotted with models B and C for comparison. The clumpy cases have a slightly higher overall flow velocity ( $v$ )

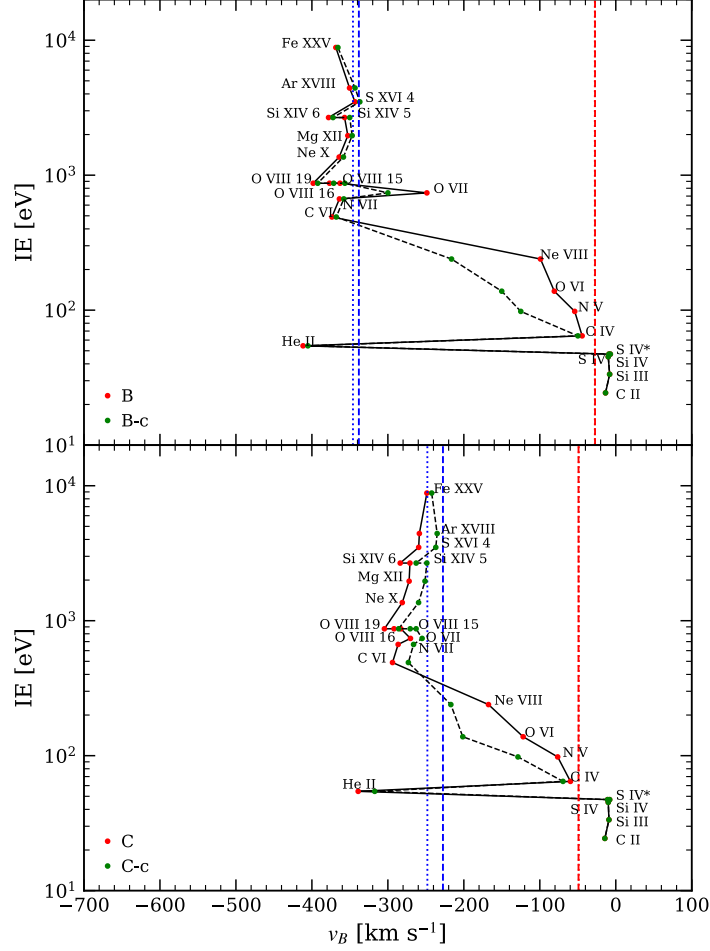


Figure 3.11: Ionization energy vs velocity of the blue-edge of line profiles (defined as where  $I = 0.99$ ) for steady models (black solid line with red dots) compared to their clumpy versions (black dashed line with green dots). The dotted (dashed) blue and red vertical lines indicate the maximum flow velocity and the velocity where  $\xi = \xi_{c,max}$ , respectively, for the clumpy (steady) models.

(compare the blue vertical lines; dashed lines are for steady solutions and dotted lines for their clumpy counterparts). While higher IE ions show slightly lower  $v_B$  for clumpy cases, intermediate ions show a very prominent increase in  $v_B$  of their absorption troughs due to the presence of the clumps. This is because these ions (namely, N V, O VI, and Ne VIII) are direct probes of the temperature within the clumps and therefore deepen the absorption at the blue edge. The low IE ions, meanwhile, show no change in their  $v_B$  values between steady and clumpy models. Again, these ions form at the base of the flow have negligible opacity within the clumps.

In Figs. 3.12 and 3.13, we compare steady and clumpy models for our entire collection of line profiles. As we mentioned above, model C-c is so clumpy that the blue wings of the line profiles remain essentially monotonic. Rather than produce distinguishable absorption troughs, small intercloud spacings simply result in an increase in the depth of line profiles for most ions. There are, however, a few

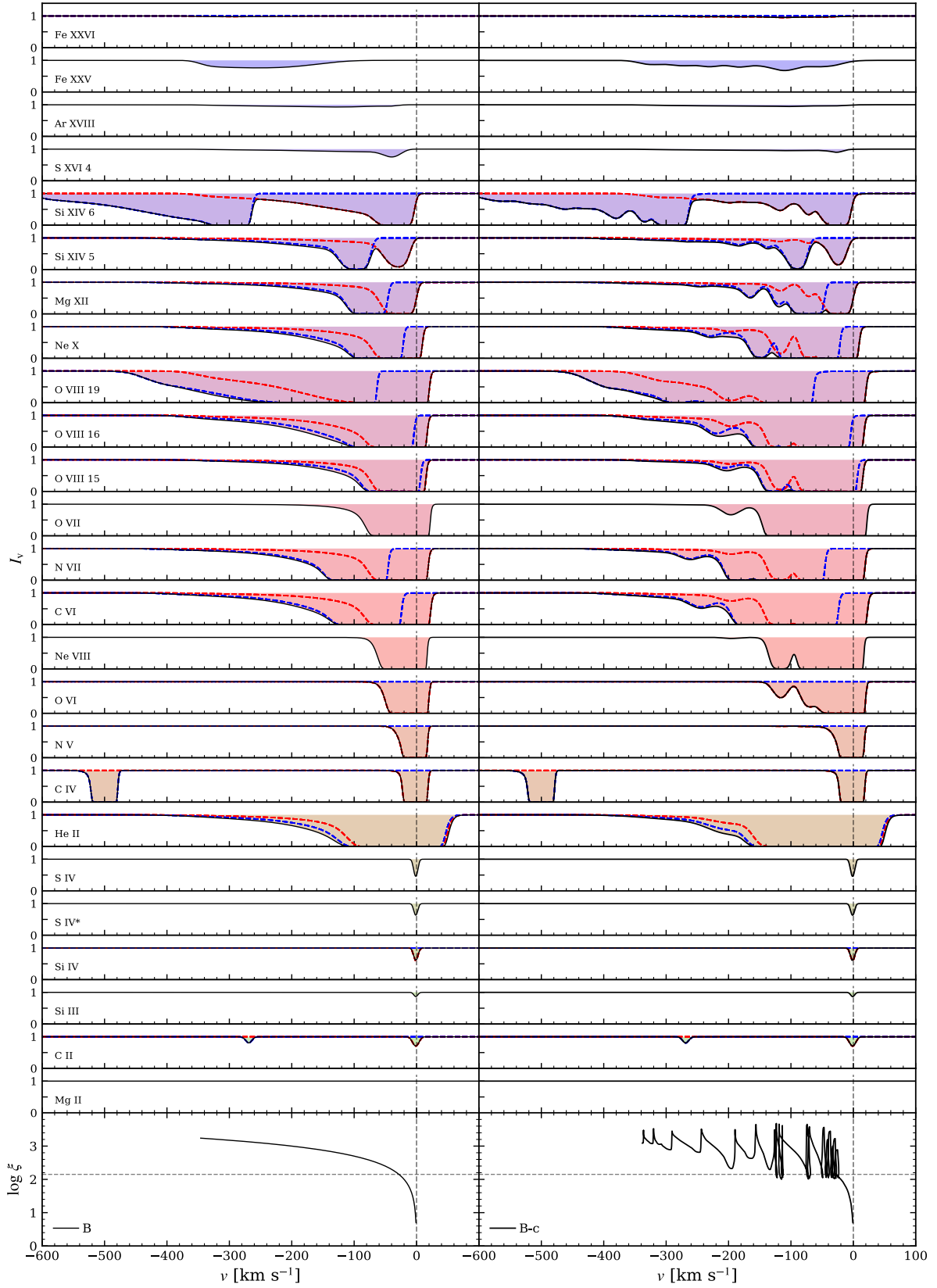


Figure 3.12: Same as 3.7, but for steady model B compared to clumpy model B-c.



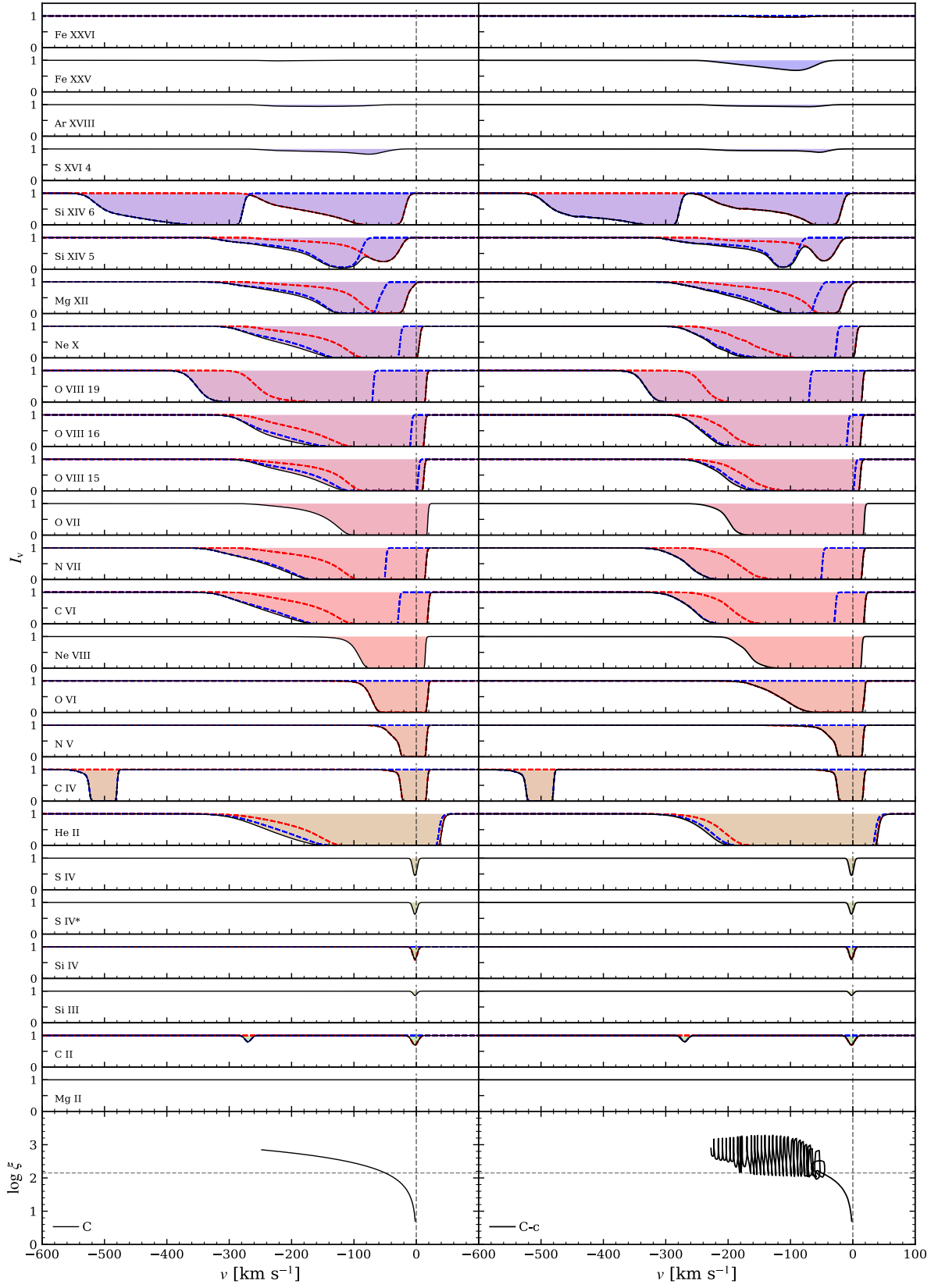


Figure 3.13: Same as 3.12, but for steady model C compared to clumpy model C-c.

cases of less deep absorption (e.g., Mg XII, O VIII, and Si XIV), and this occurs also in model B-c as seen most clearly for Si XIV 5 in Fig. 3.9. To explain this, note that locally, the individual clumps are isobaric, meaning the clumps are also associated with under-densities corresponding to higher temperature intercloud regions. For the ions noted, these regions have less opacity compared to smooth solutions where the temperature is intermediate between cloud and intercloud gas temperatures. Thus, the column density of ions with peak abundance in intermediate temperature gas can be less in the presence of clumps, and this accounts for the reduced absorption. Conversely, the higher column of hot gas in the presence of clumps explains the increased absorption in Fe XXV, which only forms in high temperature gas.

We conclude here that it is non-trivial to determine the wind structure based on line profiles. Despite the presence of clumps in outflows, line profiles can be smooth and monotonic under certain conditions. We also note that different velocity components are not necessarily distinctive outflows (e.g., flows launched from different geometries with different escape velocities), but are instead potentially just different parts of the same flow.

### 3.7 Conclusion

The conditions for generating outflows that are heated and driven by AGN radiation place these outflows at parsec scales from the central engine, where the gas is mildly bound. Such outflows can be responsible for WAs in AGNs. In this paper, we present results from our calculations of synthetic absorption line profiles that are based on smooth/clumpy models of thermally driven outflows from AGNs. Although our calculations are based on 1D radial outflow models, we find that each model produces diverse profiles and some profiles are quite complex, especially for clumpy models. We classify our line profiles into four major categories: 1) Gaussian (typical for weak lines, e.g., the S IV line), 2) boxy (lines with a strong broad core, e.g., the C IV line), 3) boxy with an extend blue wing (e.g., Mg XII), and 4) weak extended (e.g., Fe XXV). In Figs. 3.7, 3.12, and 3.13, we show examples of how line widths and shapes vary depending on the ionization energy of the absorbing ion. To explore the effects of outflow clumpiness, we present the breakdown of a line profile due to Mg XII as an example (see Fig. 3.9). This figure shows that clumps can produce deeper absorption troughs in the blue wing compared to a smooth flow, whereas the cold slow gas at the base of the outflow dominates the line center.

One of the key outflow properties is the terminal velocity. Therefore, we check whether there are any relations between the maximum outflow velocity in our models and the predicted line properties. We

Lines	$\lambda_0$ [Å]	$\Delta v$ [km s <sup>-1</sup> ]	IE [eV]	Lines	$\lambda_0$ [Å]	$\Delta v$ [km s <sup>-1</sup> ]	IE [eV]
Fe XXVI	1.77802 1.78344	911.0	9277.69	C VI	33.7342 33.7396	48.0	489.99
Fe XXV	1.8505	–	8828.0	Ne VIII	780.324	–	239.10
Ar XVIII	3.7311	–	4426.23	O VI	1031.91 1037.61	1648.0	138.12
S XVI 4	3.9908	–	3494.19	N V	1238.82 1242.80	961.0	97.89
Si XIV 6	6.18042 6.18583	262.6	2673.18	C IV	1548.2 1550.77	497.0	64.49
Si XIV 5	5.21681 5.21795	65.6	2673.18	He II	303.780 303.786	5.9	54.42
Mg XII	7.10577 7.10691	48.1	1962.66	S IV	1073.51	–	47.22
Ne X	10.2385 10.2396	32.2	1362.20	S IV*	1062.66	–	47.22
O VIII 19	18.9671 18.9725	85.4	871.41	Si IV	1393.76 1402.77	1927.0	45.14
O VIII 16	16.0055 16.0067	22.5	871.41	Si III	1206.5	–	33.49
O VIII 15	15.1760 15.1765	9.9	871.41	C II	1334.52 1335.71	268.0	24.38
O VII	21.602	–	739.29	Mg II	2798.75	–	15.04
N VII	24.7792 24.7846	65.7	667.046				

Table 3.3: Ions used for computing line profiles (in decreasing order of IE). We denote different transitions for the same ion with a number, which corresponds to the wavelength of the transition, as in Si XIV 5 and Si XIV 6. The 2<sup>nd</sup>, 3<sup>rd</sup>, and 4<sup>th</sup> column denote the rest frame wavelength  $\lambda_0$ , the velocity shift (in km s<sup>-1</sup>) of the doublet components  $\Delta v = c(\lambda_b - \lambda_r)/\lambda_r$  (where subscripts  $r$  and  $b$  denote red and blue components) and the ionization energy of the ion, IE.

found that the highly ionized ion species (such as Fe XXV) with ionization energies above 100 eV trace the fastest part of the outflows. Fig. 3.8 shows that line profiles due to these very highly ionized species could be strongly blueshifted. Most blueshifts from these ions are comparable to the outflow terminal velocity in our thermally unstable solutions, both steady state and clumpy versions. In our thermally stable model A21, however, the blue line wing is very extended and weak so that the blue end is difficult to determine. If one then uses the width of the strong, often saturated core of the line, the wind velocity can be underestimated by an order of magnitude.

Our outflow models produce line profiles that are unlike those expected for a spherical flow. For example, winds from OB stars can be well approximated as 1D spherical outflows and their absorption profiles show maximum absorption near the highest velocities (e.g., Lamers & Cassinelli, 1999). Our profiles show maximum absorption near zero velocity which is more characteristic of bipolar disk winds in cataclysmic variables (see e.g. Drew, 1987). We realize that in both winds from OB stars and in winds from cataclysmic variables, line emission is important. Nevertheless, this simple comparison illustrates that even smooth spherical winds can produce surprising line profiles that at least superficially show similarities to profiles produced by axisymmetric disk wind calculations, a good example being the diverse line profiles shown by Giustini & Proga (2012). However, in disk winds the diversity is typically due to the line profile dependence on the inclination angle. Here we report on the importance of the wind ionization structure (see also the ionization stratification effects on line profiles in Waters et al., 2021, which is our companion paper on clumpy thermally driven disk winds).

We note the line profiles of our clumpy solutions are characterized by significantly non-monotonic blue wings *only* if the separation in velocity space between individual clumps is greater than the thermal width of the gas within and between the clumps. This is the difference between our models B-c and C-c (compare Figs. 3.12 and 3.13); the non-monotonic wings in model B-c are due to clumps producing blueshifted absorption troughs at velocities outside of the line core. Additionally, the small clump spacing in a highly clumped model like C-c, results in smaller columns of intercloud gas, which are at temperatures where the opacity of certain lines (S XVI and Si XIV) reach peak values. A close comparison of the left and right panels in Figs. 3.13 revealed that these lines are actually weaker in model C-c compared to smooth model C.

Future X-ray observatories equipped with micro-calorimeters, such as the X-ray Imaging and Spectroscopy Mission (XRISM Science Team, 2020, launch expected in 2022) and the Advanced Telescope for High ENergy Astrophysics (Athena; Nandra et al., 2013, launch expected in the 2030s) mission should permit distinguishing different shapes of absorption line profiles and should also allow charac-

terizing clump-like features in the X-ray spectra of nearby AGN such as NGC 5548, if present. Spectra from these observatories will provide a uniform energy resolution down to a few eV over a wide energy range, including in the Fe K band, allowing velocity features of only a few  $\text{km s}^{-1}$  to be resolved. Despite the great wealth of current observational data, these future spectral resolutions are needed for the precise comparison of our models for WAs due to the relatively small velocities involved (e.g., see Laha et al., 2021, for a recent review).

Our main conclusion is that thermally driven wind solutions constitute viable models for WAs. Therefore, we plan to further develop these models, as well as to increase the fidelity of our line profile calculations. We finish the paper by mentioning just a few of the future developments we have planned.

To better treat line saturation, we plan to implement Lorentzian profiles instead of Gaussian profiles. In addition, it is of course important to consider the contribution of emission to absorption line profile calculations. Indeed, Lucy (1983) showed that non-monotonic velocity profiles in O star winds give rise to saturated P Cygni profiles with flat bottoms. For our future work, we expect that exploration of emission line profiles could result in significant emission lines near  $v = 0$ , which could extend to larger velocities and make absorption appear weaker. Studies of X-ray binaries where AGN-like warm absorbers are sometimes observed show that the line emission could be indeed important (i.e., Miller et al., 2002, 2004).

On the hydrodynamical modeling side, we compared conduction and cooling timescales and found that thermal conduction may be important, especially in regions between clumps that have high temperature contrasts (the importance of including thermal conduction in local cloud simulations has already been demonstrated; e.g. Proga & Waters, 2015). Therefore, we plan to assess the effects of thermal conduction on line profiles in our future calculations. Finally, the time variability due to clump evolution on observable timescales is insignificant, as shown in Fig. 3.10. This may be indicative of the limitations of our assumption of pure photoionization models in thermal equilibrium. We therefore plan to assess if non-equilibrium effects can be important.

## Chapter 4

### Conclusion

Detection of outflows from accretion disks in X-ray binaries and Active Galactic Nuclei have been used to study the self-regulating accretion feedback processes and the launching mechanisms of disk winds. X-ray binaries demonstrate state transitions and quasi-periodic oscillations. The theory of time evolution of accretion disks destabilized by outflows or winds have been used to explain such state changes. Several efforts have been made to explain the observed transitions and, with more sophisticated observational tools, more varieties of state transitions have been detected. The classic Compton-heated thermal wind launched from accretion disks could destabilize disk accretion leading to sinusoidal oscillations. Although upon comparison with observations, such sinusoidal or well-behaved periodic oscillations are hardly ever detected (Shields et al., 1986). In our work Ganguly & Proga (2020), we allowed the fixed wind launching criteria to be relaxed in the wind-driven relaxation cycle. We found that the closer the launching radius was to the innermost disk edge, the more easily the disk was destabilized for a much smaller critical value of the parameter coupling the wind to the central irradiating luminosity. The change in mass accretion rate or luminosity may not be sufficient to explain state transitions, while the large variations in surface density at the outer radii may have significant detectable effects.

We have also developed a pipeline to generate synthetic absorption line profiles for any outflow models from numerical simulations in Ganguly et al. (2021). Line emissions and absorptions provide a vital tool for determining outflow properties. The bulk motion imprints as Doppler shifts, while the local thermal velocity broadens the observed line profiles. With sufficiently sensitive and high-resolution future missions, we may be able to compare our theories of such outflows against observations of line profiles by comparing with our synthetic profiles generated in post-processing. The parameter space explored by us consist of the so-called warm absorbers detected in outflows of AGNs. Our results showed that secondary absorption features can be detected in a clumpy outflow solution as opposed to a smooth one, depending on the properties of the clumps. Yet, not all outflows with the presence of clumps end up displaying these distinguishing features. Depending on how closely spaced the clumps are and/or the velocity entrained within a clump compared to the local thermal velocity of the neighbouring inter-cloud medium, even clumpy solutions may produce smooth blue wings in the absorption troughs. Our exploration of a range of absorption lines due to ions with energies in the range of eV-keV showed a clear ionization stratification in the outflows as well. Overall we can conclude that the thermally-driven

clumpy wind models presented in this work can be considered as viable warm absorber models, and direct comparison with future *X*-ray missions can test this with certainty. Including emission lines in our module, incorporating results from higher dimensional hydrodynamic simulations and considering Lorentzian profiles would be some of the more immediate steps to further generalize and make robust the analyses of the results from our ‘line profile generator’.

## References

- Abbott, D. C. 1980, *ApJ*, 242, 1183
- Abramowicz, M. A., Czerny, B., Lasota, J. P., & Szuszkiewicz, E. 1988, *ApJ*, 332, 646
- Abramowicz, M. A., & Lasota, J. P. 1995, *Comments on Astrophysics*, 18, 141
- Allen, J. L., Schulz, N. S., Homan, J., et al. 2018, *ApJ*, 861, 26
- Antonucci, R. 1993, *ARAA*, 31, 473
- Arav, N., Barlow, T. A., Laor, A., & Blandford, R. D. 1997, *MNRAS*, 288, 1015
- Arnaud, K. A. 1996, in *Astronomical Society of the Pacific Conference Series*, Vol. 101, *Astronomical Data Analysis Software and Systems V*, ed. G. H. Jacoby & J. Barnes, 17
- Balbus, S. A. 1986, *ApJL*, 303, L79
- Balbus, S. A., & Hawley, J. F. 1991, *ApJ*, 376, 214
- . 1998, *Reviews of Modern Physics*, 70, 1
- Balbus, S. A., Hawley, J. F., & Stone, J. M. 1996, *ApJ*, 467, 76
- Beckmann, V., & Shrader, C. 2012, in *Proceedings of “An INTEGRAL view of the high-energy sky (the first 10 years)” - 9th INTEGRAL Workshop and celebration of the 10th anniversary of the launch (INTEGRAL 2012). 15-19 October 2012. Bibliotheque Nationale de France*, 69
- Begelman, M. C., McKee, C. F., & Shields, G. A. 1983, *ApJ*, 271, 70
- Behar, E. 2009, *The Astrophysical Journal*, 703, 1346
- Belcher, J. W. 1971, *ApJ*, 168, 509
- Belloni, T. 2005, in *American Institute of Physics Conference Series*, Vol. 797, *Interacting Binaries: Accretion, Evolution, and Outcomes*, ed. L. Burderi, L. A. Antonelli, F. D’Antona, T. di Salvo, G. L. Israel, L. Piersanti, A. Tornambè, & O. Straniero, 197–204
- Blondin, J. M. 1994, *ApJ*, 435, 756
- Casares, J., Muñoz-Darias, T., Mata Sánchez, D., et al. 2019, *MNRAS*, 488, 1356



- Castor, J. I., Abbott, D. C., & Klein, R. I. 1975, *ApJ*, 195, 157
- Chevallier, L., Collin, S., Dumont, A. M., et al. 2006, *A&A*, 449, 493
- Cox, D. P., & Smith, B. W. 1974, *ApJL*, 189, L105
- Dannen, R. C., Proga, D., Kallman, T. R., & Waters, T. 2019, *ApJ*, 882, 99
- Dannen, R. C., Proga, D., Waters, T., & Dyda, S. 2020, *ApJL*, 893, L34
- Das, V., Crenshaw, D. M., Hutchings, J. B., et al. 2005, *Astron. J.*, 130, 945
- Díaz Trigo, M., & Boirin, L. 2013, *Acta Polytechnica*, 53, 659
- Díaz Trigo, M., Migliari, S., Miller-Jones, J. C. A., & Guainazzi, M. 2014, *A&A*, 571, A76
- Drew, J. E. 1987, *MNRAS*, 224, 595
- Dubus, G., Done, C., Tetarenko, B. E., & Hameury, J.-M. 2019, *A&A*, 632, A40
- Dyda, S., Dannen, R., Waters, T., & Proga, D. 2017, *MNRAS*, 467, 4161
- Elvis, M., Wilkes, B. J., McDowell, J. C., et al. 1994, *ApJS*, 95, 1
- Fender, R., Belloni, T., & Gallo, E. 2005, *Astrophysics and Space Science*, 300, 1
- Ferland, G. J., Chatzikos, M., Guzmán, F., et al. 2017, *Revista Mexicana de Astronomía y Astrofísica*, 53, 385
- Field, G. B. 1965, *ApJ*, 142, 531
- Frank, J., King, A., & Raine, D. J. 2002, *Accretion Power in Astrophysics: Third Edition*
- Fromang, S., & Lesur, G. 2019, in *EAS Publications Series*, Vol. 82, *EAS Publications Series*, 391–413
- Fromang, S., & Papaloizou, J. 2007, *A&A*, 476, 1113
- Fukumura, K., Kazanas, D., Shrader, C., & Tombesi, F. 2020, in *American Astronomical Society Meeting Abstracts*, Vol. 236, *American Astronomical Society Meeting Abstracts #236*, 208.01
- Ganguly, S., & Proga, D. 2020, *ApJ*, 890, 54
- Ganguly, S., Proga, D., Waters, T., et al. 2021, *ApJ*, 914, 114
- Gatuzz, E., Díaz Trigo, M., Miller-Jones, J. C. A., & Migliari, S. 2019, *MNRAS*, 482, 2597

- Ghisellini, G., Haardt, F., & Matt, G. 2004, A&A, 413, 535
- Gierliński, M., Zdziarski, A. A., Poutanen, J., et al. 1999, MNRAS, 309, 496
- Giustini, M., & Proga, D. 2012, ApJ, 758, 70
- Goldsmith, D. W., Habing, H. J., & Field, G. B. 1969, ApJ, 158, 173
- Higginbottom, N., Proga, D., Knigge, C., & Long, K. S. 2017, ApJ, 836, 42
- Holczer, T., Behar, E., & Kaspi, S. 2007, The Astrophysical Journal, 663, 799
- Janiuk, A., Czerny, B., & Siemiginowska, A. 2002, ApJ, 576, 908
- Kaastra, J. S., Mewe, R., & Nieuwenhuijzen, H. 1996, in UV and X-ray Spectroscopy of Astrophysical and Laboratory Plasmas, 411–414
- Kallman, T., & Bautista, M. 2001, ApJS, 133, 221
- Kallman, T. R., & McCray, R. 1982, ApJS, 50, 263
- Kaplan, S. A. S. A. 1970, The interstellar medium (Cambridge, Mass.: Harvard University Press)
- Kaspi, S., Brandt, W. N., George, I. M., et al. 2002, ApJ, 574, 643
- King, A. L., Miller, J. M., Raymond, J., et al. 2013, ApJ, 762, 103
- King, A. R., Pringle, J. E., & Livio, M. 2007, Monthly Notices of the Royal Astronomical Society, 376, 1740
- Knigge, C., Scaringi, S., Goad, M. R., & Cottis, C. E. 2008, MNRAS, 386, 1426
- Kolman, M., Halpern, J. P., Shrader, C. R., & Filippenko, A. V. 1991, ApJ, 373, 57
- Körding, E. G., Jester, S., & Fender, R. 2006, MNRAS, 372, 1366
- Kriss, G. A. 1988, ApJ, 324, 809
- Krolik, J. H. 1999, Active galactic nuclei : from the central black hole to the galactic environment
- Krolik, J. H., McKee, C. F., & Tarter, C. B. 1981, ApJ, 249, 422
- Kubsch, M., Illenseer, T. F., & Duschl, W. J. 2016, A&A, 588, A22
- Kuhn, O., Bechtold, J., Cutri, R., Elvis, M., & Rieke, M. 1995, ApJ, 438, 643

- Laha, S., Guainazzi, M., Chakravorty, S., Dewangan, G. C., & Kembhavi, A. K. 2016, MNRAS, 457, 3896
- Laha, S., Reynolds, C. S., Reeves, J., et al. 2021, Nature Astronomy, 5, 13
- Lamers, H. J. G. L. M., & Cassinelli, J. P. 1999, Introduction to Stellar Winds
- Lamers, H. J. G. L. M., & Morton, D. C. 1976, ApJS, 32, 715
- Laor, A., & Brandt, W. N. 2002, ApJ, 569, 641
- Lawrence, A., Elvis, M., Wilkes, B. J., McHardy, I., & Brandt, N. 1997, MNRAS, 285, 879
- Lucy, L. B. 1983, ApJ, 274, 372
- Lucy, L. B., & Solomon, P. M. 1970, ApJ, 159, 879
- Luketic, S., Proga, D., Kallman, T. R., Raymond, J. C., & Miller, J. M. 2010, ApJ, 719, 515
- Lynden-Bell, D. 1969, Nature, 223, 690
- Lynden-Bell, D., & Pringle, J. E. 1974, MNRAS, 168, 603
- Martin, R. G., Nixon, C. J., Pringle, J. E., & Livio, M. 2019, New Ast., 70, 7
- McKee, C. F., & Ostriker, J. P. 1977, ApJ, 218, 148
- Mehdipour, M., Kaastra, J. S., & Kallman, T. 2016, A&A, 596, A65
- Mehdipour, M., Kaastra, J. S., Kriss, G. A., et al. 2015, A&A, 575, A22
- Mendoza, C., Bautista, M. A., Deprince, J., et al. 2021, Atoms, 9, 12
- Miller, J. M., Raymond, J., Fabian, A., et al. 2006, Nature, 441, 953
- Miller, J. M., Fabian, A. C., Wijnands, R., et al. 2002, ApJ, 578, 348
- Miller, J. M., Raymond, J., Fabian, A. C., et al. 2004, ApJ, 601, 450
- Montesinos, M. 2012
- Nandra, K., Barret, D., Barcons, X., et al. 2013
- Narayan, R., & Yi, I. 1994, ApJL, 428, L13

- Neilsen, J. 2013, *Advances in Space Research*, 52, 732
- Neilsen, J., & Lee, J. C. 2009, *Nature*, 458, 481
- Neilsen, J., Remillard, R. A., & Lee, J. C. 2011, *ApJ*, 737, 69
- Netzer, H. 2008, *NewAstRev*, 52, 257
- . 2015, *ARAA*, 53, 365
- Nixon, C. 2015, *MNRAS*, 450, 2459
- Novikov, I. D., & Thorne, K. S. 1973, in *Black Holes (Les Astres Occlus)*, 343–450
- Nowak, M. A. 1995, *Pub. of the Ast. Soc. of the Pac.*, 107, 1207
- Ogilvie, G. I. 2016
- Paczyński, B., & Wiita, P. J. 1980, *A&A*, 500, 203
- Parker, E. N. 1965, *SSR*, 4, 666
- Pringle, J. E. 1981, *ARAA*, 19, 137
- Proga, D., & Kallman, T. R. 2002, *ApJ*, 565, 455
- Proga, D., & Waters, T. 2015, *ApJ*, 804, 137
- Różańska, A., Goosmann, R., Dumont, A. M., & Czerny, B. 2006, *A&A*, 452, 1
- Ryan, B. R., Gammie, C. F., Fromang, S., & Kestener, P. 2017, *ApJ*, 840, 6
- Sako, M., Kahn, S. M., Behar, E., et al. 2001, *A&A*, 365, L168
- Salpeter, E. E. 1964, *ApJ*, 140, 796
- Shakura, N. I., & Sunyaev, R. A. 1973, *A&A*, 500, 33
- Shields, G. A., McKee, C. F., Lin, D. N. C., & Begelman, M. C. 1986, *ApJ*, 306, 90
- Shklovskii, I. S. 1968, *Soviet Astronomy*, 11, 749
- Shu, F. H. 1992, *Physics of Astrophysics*, Vol. II
- Sim, S. A., Long, K. S., Miller, L., & Turner, T. J. 2008, *MNRAS*, 388, 611

- Sim, S. A., Miller, L., Long, K. S., Turner, T. J., & Reeves, J. N. 2010, MNRAS, 404, 1369
- Stone, J. M., Tomida, K., White, C. J., & Felker, K. G. 2020
- Tarter, C. B., Tucker, W. H., & Salpeter, E. E. 1969, ApJ, 156, 943
- Tetarenko, B. E., Lasota, J. P., Heinke, C. O., Dubus, G., & Sivakoff, G. R. 2018, Nature, 554, 69
- Tomaru, R., Done, C., Ohsuga, K., Nomura, M., & Takahashi, T. 2019, MNRAS, 490, 3098
- Tripp, T. M., Bechtold, J., & Green, R. F. 1994, ApJ, 433, 533
- Waters, T., Proga, D., & Dannen, R. 2021
- Waters, T., Proga, D., Dannen, R., & Kallman, T. R. 2017, MNRAS, 467, 3160
- Weber, E. J., & Davis, Leverett, J. 1967, ApJ, 148, 217
- Wilkes, B. 2004, in Astronomical Society of the Pacific Conference Series, Vol. 311, AGN Physics with the Sloan Digital Sky Survey, ed. G. T. Richards & P. B. Hall, 37
- Woods, D. T., Klein, R. I., Castor, J. I., McKee, C. F., & Bell, J. B. 1996, ApJ, 461, 767
- XRISM Science Team. 2020
- Zel'dovich, Y. B. 1964, Soviet Physics Doklady, 9, 195
- Zoghbi, A., Miller, J. M., King, A. L., et al. 2016, ApJ, 833, 165

## Curriculum Vitae

**Name:** Shalini Ganguly  
**Email address:** gangulyshalini1@gmail.com / ganguly@unlv.nevada.edu  
**Languages known:** Bengali (mother tongue), English (fluent) & Hindi (fluent)  
**Nationality:** Indian

### Education

---

- Doctor of Philosophy (Ph.D.) in Astronomy (2017-) at *University of Nevada Las Vegas (UNLV), USA*.
- Master of Science (M.Sc.) in Physics (2015-2017) at *Indian Institute of Technology Hyderabad (IITH), India*.
- Bachelor of Science (B.Sc.) in Physics at *Lady Brabourne College, Kolkata*, affiliated to *Calcutta University, India*.

### Research Interests

---

- Investigating formation and dynamics of accretion disks in binary star systems, state transitions in low mass X-ray binaries (LMXBs) and high energy processes in transonic outflows from X-ray binaries.
- Studying active galactic nuclei (AGN) feedback and outflows using numerical simulations, investigating observational consequences of such outflows via synthetically generated line profiles.
- Studying other high energy processes in the above systems, namely, jet production and its observational consequences, cloud formation and dynamics, winds and self-regulating feedbacks.

### Publication List

---

- **S. Ganguly, et al.,** *On Synthetic Absorption Line Profiles of Thermally Driven Winds from Active Galactic Nuclei*, ApJ 914 114 (2021).
- **S. Ganguly, D.Proga,** *On the wind-driven relaxation cycle in accretion disks*, The Astrophysical Journal, Volume 890, Issue 1, id.54, 8 pp. (2020).
- **S. Ganguly, S. Desai,** *Statistical significance of spectral lag transition in GRB 160625B*, Astroparticle Physics, Volume 94, p. 17-21. (2017).

### Research Experience

---

#### Doctoral Research

(2017-)

*Department of Physics and Astronomy, University of Nevada Las Vegas*

- Studying thermal instability-generated clumps in AGN outflows via synthetic absorption line profiles. Used the hydrodynamics code ATHENA++ to reproduce the clumpy outflow solutions of *Dannan et al. 2020*. Wrote a pipeline in python to interface with photoionization calculations from the code XSTAR to calculate synthetic absorption line profiles for 1D radial outflows.
- Modelling Compton-heated disk winds in black hole binary or AGN systems. Wrote a python code to simulate the self-regulating accretion-wind feedback system for several coupling parameters.

### Graduate Research

(2015-2017)

*Department of Physics. IIT, Hyderabad*

- Master's thesis titled "*Triplet Fermion in the light of neutrino mass and dark matter*", under the supervision of *Dr. Narendra Sahu*.
- Studied the validity of gamma ray burst (GRB) time lag data to justify the loop quantum gravity proposition of Lorentz invariance violation (LIV).
- Summer project titled "*Semi-numerical model of reionization*", under the supervision of *Dr. Tirthankar Roychowdhury* at *National Center for Radio Astrophysics (NCRA)*, Pune, India. Wrote a FORTRAN99 code to locate centers of ionization bubbles during the epoch of reionization from a 3D grid of data generated by IGM evolution code CITE.

### Poster Presentations

---

- Poster presentation titled "*On Synthetic Absorption Line Profiles of Thermally Driven Winds from AGN*" at the *Relativistic Astrophysics, Theory and Observational Perspectives* virtual symposium on 16-19 March, 2021, organized by *CTP PAS, Warsaw, Poland*.
- *1 minute lightning talk* titled "*On Synthetic Absorption Line Profiles of Thermally Driven Winds from AGN*" at the *Polarized Radiation near Supermassive Black Holes* virtual conference on May 10-13, 2021, organized by *Princeton Center for Theoretical Science, Princeton University, NJ, USA*.

### Contributed Talks

---

- Online Seminar 'Neem' at *Inter-University Center for Astronomy and Astrophysics (IUCAA)*, Pune, India titled "*On Synthetic Absorption Line Profiles of Thermally Driven Winds from AGN*" on September 30, 2021.

### Conferences and Workshops

---

- *Black Hole Accretion Disk Winds* meeting organized by *Durham University, London* from September 6-9, 2021 (hybrid meeting).

- *European Astronomical Society (EAS) Annual meeting* from June 28-July 2, 2021 (virtual conference).
- *AtomDB Workshop and Advanced Spectroscopy School* from August 3-5, 2020, organized by *Harvard-Smithsonian Center for Astrophysics* (virtual meeting).
- *Advancing Theoretical Astrophysics (ATA)* workshop from July 15-26 2019, at Anton Pannakoek Institute for Astronomy, University of Amsterdam, Netherlands.
- *Winter School in Astronomy/Workshop on Stellar Clusters* (Feb 2017) organized by *Western University, Canada* (IAU), *YPCST* and *B.M.Birla Science Center*, Hyderabad, India.
- *Introductory course in Astronomy* (2013-14) at the *M.P.Birla Planetarium*, Kolkata, India, including lectures by *Dr. Debiprosad Duari* (Director, M.P. Birla Planetarium, Kolkata), on a range of topics in astronomy from solar system to cosmology and general relativity.
- UGC sponsored national seminar (2013) on *Recent Advances in the Frontiers of Physics*, organized by Dept. of Physics, Bidhannagar College, Saltlake, Kolkata, in collaboration with Indian Association for the Cultivation of Science, Jadavpur, Kolkata.

### Teaching Experience

---

**Courses Taught:** General Physics Lab I & II

Physics for Scientists and Engineers Lab I, II & III.

**Department:** Department of Physics and Astronomy

**Topics:** Newtonian mechanics, heat, electricity and magnetism, optics and modern physics.

**Responsibilities:** Preparing comprehensive study guides and weekly solutions to post-lab assignments and recording instructional videos for pre-lab guidance.

### Positions

---

- Teaching assistant Aug-Dec 2017, 2018, 2019, 2020; Jan-May 2018, 2019, 2020, 2021.
- Research assistant June-Aug 2018, 2019, 2020, 2021

### Mentoring experience

---

- Participated in Graduate Professional Student Association (GPSA)/Consolidated Students of UNLV (CSUN) Mentorship Co-op program for the term Spring 2022; assigned to mentor Mr. Rashad Hall, Department of Mathematics, UNLV.

### Other Academic Achievements

---

- Secured All India Rank of 102 in *CSIR-UGC NET* (National Eligibility Test) and qualified for the *Joint Research Fellowship (JRF)*.



- Secured All India Rank of 286 in *Joint Admission for M.Sc.* exam among  $\sim 9000$  students appearing for the exam.

**Technical Skills** 

---

**Computer Languages**                      C/C++, Python, FORTRAN

**Specific Scientific Softwares**            ATHENA++, Numpy, Scipy